A Measurement of the Angular Power Spectrum of the Cosmic Microwave Background with a Long Duration Balloon-borne Receiver

Thesis by

Brendan P. Crill

In Partial Fulfillment of the Requirements

for the Degree of

Doctor of Philosophy

California Institute of Technology

Pasadena, California

2001

(Submitted November 9, 2000)

Abstract

This thesis describes BOOMERANG; a balloon-borne telescope and receiver designed to map the Cosmic Microwave Background (CMB) at a resolution of $10'$ from the Long Duration Balloon (LDB) platform. The millimeter-wave receiver employs new technology in bolometers, readout electronics, cold re-imaging optics, millimeter-wave filters, and cryogenics to obtain high sensitivity to CMB anisotropy. Sixteen detectors observe in 4 spectral bands centered at 90, 150, 240 and 400 GHz. The wide frequency coverage, the long flight duration, the optical design and the observing strategy all provide strong rejection of systematic effects. We report the in-flight performance of the instrument during a short test flight from Palestine, Texas, that mapped 230 square degrees and during a 10.5 day stratospheric balloon flight launched from McMurdo Station, Antarctica, that mapped $\sim$ 2000 square degrees of the sky. The Antarctic data yielded a measurement of the angular power spectrum of the CMB between $50 < \ell < 600$ which shows a peak at $\ell_{peak} = 197 \pm 6$ (1σ error). A maximum likelihood estimation of cosmological parameters within the cold dark matter (CDM) paradigm of structure formation indicates that the universe is flat with a precision of $\sim 6\%$ and that the density of baryons in the universe may be slightly higher than previously thought. The combination of observations of large scale structure (LSS) and the BOOMERANG power spectrum implies the presence of both dark matter and dark energy, or the existence of Einstein's cosmological constant.

Acknowledgments

> ...let me ask you how the scholar who cultivates science to pass his life agreeably differs from the drunkard who also seeks in life no more than immediate enjoyment and finds it in wine? It is true that the scholar makes a better choice of the source of his pleasures, since they are more intense and more durable, but that is all. Both of them, the drunkard and the scholar have the same egotistical aim, personal enjoyment.
>
> ... if you are really thinking of helping humanity, if that is what you aspire to in your studies, you will find yourself facing a formidable objection, for, in so far as you have any sense of justice, you will immediately observe that in present-day society, science is only a kind of luxury that makes life more agreeable to a few, and remains absolutely inaccessible to almost the whole of humanity.
>
> Peter Kropotkin, *To the Young* (1885)

BOOMERANG is an enormous project which has required huge amounts of labor from quite a few people since it began in 1993. The author lists on each of the BOOMERANG publications, no matter how long, can never properly credit all of the people who have contributed to this project over the years. My thanks goes out to all of these people, without whom this thesis would not exist.

As of June 2000, here is the list in alphabetical order of everyone who has worked on BOOMERANG: Peter Ade, Kashif Alvi, Joffa Applegate, Elisabetta Aquilini, Ricardo Artusa, Andy Beard, Jeff Beeman, Ravinder Bhatia, Jamie Bock, Dick Bond, Julian Borrill, Andrea Boscaleri, Kurt Campbell, John Cartwright, Sarah Church, Kim Coble, Matthieu Contensou, Paolo deBernardis, Giancarlo de Gasperis, Marco dePetris, Grazia deTroia, Hector DelCastillo, Mark Devlin, Phil Farese, Ken Ganga, Massimo Gervasi, Massimiliano Giacometti, Vic Haynes, Cara Henson, Eric Hivon, Dave Horseley, Viktor Hristov, Armando Iacoangli, Andrew Jaffe, Andrew Lange, Adrian Lee, Jon Leong, Sam Li, Tao Long, Lorenzo Martinis, Silvia Masi, Peter Mason, Christophe Maquestiaux, Phil Mauskopf, John McAnulty, Jason McElroy, Alessandro Melchiorri, Francesco Melchiorri, Laura Miglio,

Tom Montroy, Barth Netterfield, Dan Osgood, Chris Paine, Ricardo Paniagua, Enzo Pascale, Byron Philhour, Francesco Piacentini, Francesco Pongetti, Simon Prunet, Andrea Raccanelli, Mike Radford, Paul Richards, Gianni Romeo, John Ruhl, Marcus Runyan, Francesco Scarramuzzi, Kacie Shelton, George Smoot, Eric Torbet, Ivy Turkington, Valerio Venturi, Nicola Vittorio, Betsy Villalpando, Johnny Wu, and Lunming Yuen.

Thanks to Stephen Peterzen, Danny Ball, the launch crew at NSBF and the NSF support team at McMurdo Station.

Additional thanks to Ravinder Bhatia, Samantha Edgington, Bill Jones, Eric Hivon, Andrew Lange, Geoff Blake, and Brian Keating for very helpful comments on this thesis.

Contents

Chapter 1 Introduction

The 2.7 K Cosmic Microwave Background (CMB), discovered in 1964 [55], is one of the most powerful observational pillars supporting the current picture of cosmology. The spectrum of the CMB (measured by COBE/FIRAS to be the best fit to a blackbody spectrum ever observed in nature [41]) strongly indicates that the universe evolved from a hot, dense state. The radiation originates from the time when the matter in the universe transitioned from an opaque plasma to transparent gas (the time of recombination), at a redshift of ~ 1000, about 300,000 years after the Big Bang.

Mapping the background radiation provides a snapshot of the universe in its infancy. The tiny (a part in 10^5 of the background) fluctuations seen in the temperature correspond to fluctuations in matter density at the time of recombination. A measurement of the angular power spectrum of the fluctuations of the CMB can test inflationary models of structure formation. Furthermore, within the context of the class of cold dark matter models, constraints can be placed on cosmological parameters.

The standard inflationary, cold dark matter class of models predicts structure formation as follows. The seeds of structure are provided by random quantum fluctuations stretched to cosmological size during the period of rapid inflationary expansion. The amplitude of these "primordial" fluctuations is generally expected to be nearly scale invariant. Due to the small amplitude of the fluctuations, they evolve linearly in the plasma. Gravitational collapse is resisted by photon pressure and the perturbations oscillate acoustically. Recombination occurs relatively rapidly, so the phase of the oscillations is frozen into the CMB at the time of last scattering.

Because of the oscillation, the amplitude of fluctuations at particular scales will be enhanced relative to the primordial scale-invariant amplitude. This effect appears as a series of "acoustic peaks" in the angular power spectrum. The first peak in order of decreasing angular scale corresponds to the sound horizon at the surface of last scattering; in other words, the distance that sound could travel between the Big Bang and last scattering.

Measuring the angular scale of the first (largest angular scale) acoustic peak relates this physical length scale to an angular scale. This makes a measurement of the curvature and

geometry of the universe. For example, a flat universe is expected to have an acoustic peak at a multipole of $\sim \ell = 200$, or $\sim 1^\circ$ scales.

There are degeneracies in this relation; two different sets of parameters can give nearly identical angular power spectra. For example, a large fractional density of baryons in the early universe can decrease the sound speed of the plasma, making the sound horizon smaller. This effect mimics a change in curvature. By further constraining the shape of the angular power spectrum, these degeneracies can be largely overcome. For example, the ratio of power in the first and second peaks constrains the baryon density of the universe. Another means of overcoming degeneracies is by including data from other branches of cosmology which constrain parameters in orthogonal ways; for example, measurements of light element abundances, maps of large scale structure, measurements of Hubble's constant, and Supernovae (SN1A) measurements of the expansion of the universe to high redshift.

Because of the tiny amplitude of the anisotropy in the CMB, it has taken decades of technological development of receivers, telescopes, and observation strategies for precision mapping to be successful. The past decade has seen a rapid series of advances in measurement of the angular power spectrum and the cosmology that it implies. Temperature anisotropy was first discovered on large scales ($>7^\circ$) by the DMR instrument aboard the COBE satellite in 1990. Moreover, at large scales it was found that the spectrum is scale-invariant, lending further support to the idea of inflation.

Subsequently, a host of ground-based and balloon-borne experiments detected anisotropy at a variety of angular scales (see Figure 1.1 for a summary). Starting with the Saskatoon experiment [50], the field began to move from the realm of making a detection to making spectroscopic measurements of power over a range of angular scales. Ground-based experiments have been limited by atmospheric noise, prompting moves to dry and high altitude sites, such as the Atacama desert in Chile [48] and the South Pole [16] with interferometers that have successfully defeated atmospheric noise [64]. Balloon-based measurements have been limited by detector technology and integration time. Flights above North America are normally 5-6 hours long and allow only a small region of the sky to be measured.

In 1999 results were released first by the TOCO experiment [48] and then from the 1997 test flight of BOOMERANG [44] [47] which measured the angular scale of the first acoustic peak. In April 2000, BOOMERANG published results from the Antarctic flight of 1998-

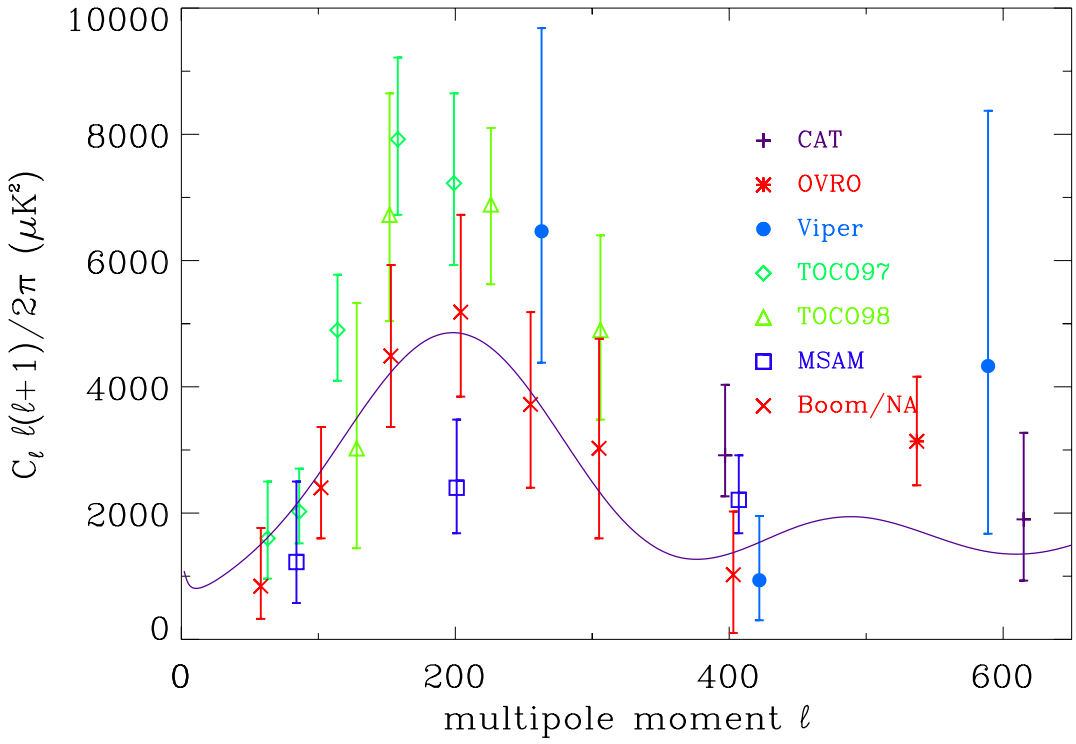

Figure 1.1:
Measurements of the angular power spectrum of the Cosmic Microwave Background in the vicinity of the first peak published between 1995 and November 1999. The solid curve shows the best fit model from the test flight of BOOMERANG (see Chapter 5 of this thesis).

1999, which exploited advances in receiver and detector technology and the long integration time available from the Long Duration Balloon (LDB) platform to make a highly precise measurement of the angular scale of the first acoustic peak [4]. A parabolic fit to the data finds that the peak is located at a multipole of $\ell = 203 \pm 6$ (1 σ error). Standard cosmological analysis implies that the density parameter $\Omega = 1.01 \pm 0.06$. The universe is flat to 6%.

Combined with other cosmological data, an even more interesting picture emerges. For the total density of the universe to be so close to the critical density, a huge fraction of it must be made up of dark matter. Furthermore, results from SN1A measurements of the expansion of the universe indicate that Einstein's cosmological constant Λ is non-zero, and if the universe is flat, in fact $\sim 70\%$ of the energy density of the universe resides in this cosmological constant [56]. This thesis describes the BOOMERANG experiment and the

cosmological measurement in detail.

1.1 Overview of BOOMERANG

BOOMERANG incorporates four unique design features which allow a precise measurement of the angular power spectrum of the CMB.

First, BOOMERANG is a quasi total-power radiometer. The temperature of one part of the sky is measured relative to its surroundings by slowly scanning (scan period 1 minute) the entire telescope in azimuth. The output from each detector is AC coupled to an amplifier at low frequency (f = 0.016 Hz). The stable, virtually transparent atmosphere at balloon float altitude and the intrinsic stability of the bolometric detectors and readout amplifier chain make it possible to map large areas of the sky with high sensitivity.

Second, BOOMERANG is designed to take advantage of the long integration time possible from a balloon borne platform flown over the Antarctic. During the austral summer, the polar vortex winds provide a stable orbit for balloons at the top of the stratosphere at an altitude of roughly 38 km. This observation platform launched 1200 km from the pole provides flight durations of 7 to 20 days, thus allowing measurements to be repeated many times in order to check for systematic effects. The relatively small fraction (<10%) of the sky that is accessible from a balloon platform during the austral summer fortuitously includes the part of the sky that is lowest in foreground contamination.

Third, the BOOMERANG receiver has a high instantaneous sensitivity, due to its optimized low-background bolometers and high-bandwidth feeds operating at cryogenic temperatures. The channels at 90 GHz and 150 GHz are positioned in frequency to optimally avoid galactic foreground contamination. In addition, combining these channels with those at 240 GHz and 400 GHz allows powerful detection and removal of foreground signals.

Finally, the BOOMERANG receiver uses re-imaging optics which provide good image quality over a large focal plane. The receiver simultaneously measures 16 bolometer channels in 8 pixels with beams separated by up to 4° on the sky. The wide format of the focal plane and large number of detectors allowed by the re-imaging optics provides the ability to search for and remove sources of correlated noise, since observations of a specific region of the sky by different detectors are well-separated in time.

This thesis describes the mathematical methods behind the measurements (Chapter

2), the design and testing of the BOOMERANG instrument (Chapters 3 and 4) and its performance during its 10.5 day flight above Antarctica during 1998-1999 (Chapter 6). Chapter 5 contains a short section on the performance of the instrument during the test flight of 1997. The calibration of the instrument with observations of the CMB dipole is described in Chapter 7. A description of the cosmological analysis and implications is included in Chapter 8. Finally, the prospects for further research with the BOOMERANG data are discussed in Chapter 9. The thesis emphasizes my contributions to the BOOMERANG experiment, which required a large international collaboration to develop, field, and produce results. My contributions were the development and testing of the receiver, the dipole calibration, and development of map-making techniques.

Chapter 2 Theory

The theory of how fluctuations in the Cosmic Microwave Background are produced and how they depend on various cosmological parameters has been well developed [61] [29]. This thesis focuses on the measurement of these cosmological parameters as an instrumental and an analytical challenge.

Extracting cosmological information from observations of the CMB involves three steps. The first step is the construction of the maximum likelihood map from the time stream data. Second, a power spectrum is computed from the map. Third, the power spectrum is compared to theoretical power spectra from various model universes to determine the most likely cosmological parameters.

2.1 Map Making

Following [68], the bolometer time stream data are modeled as follows:

$$d_t = P_{tp}\Delta_p + n_t \tag{2.1}$$

where d is the time stream data array, P is the pointing array which maps the data onto the sky, Δ is the temperature of the sky, n is the detector noise, t is the time index and p is the pixel index. Because BOOMERANG is a quasi total-power experiment, the pointing array P contains only one non-zero element per row; at any given time, only one pixel is being observed.

An estimator for the minimum variance map can be found by minimizing the quantity $\chi^2 = (d - P\Delta)^\dagger N^{-1} (d - P\Delta)$, where N^{-1} is the inverse time-time correlation matrix which is defined as $\langle nn^\dagger \rangle^{-1}$:

$$\tilde{\Delta} = \left(P^\dagger N^{-1} P\right)^{-1} P^\dagger N^{-1} d \tag{2.2}$$

In the white noise case, where the noise correlation matrix is the identity matrix, the above equation reduces to:

$$\tilde{\Delta} = \left(P^\dagger P\right)^{-1} P^\dagger d \tag{2.3}$$

The term $P^\dagger d$ is a pixel array containing the sum of all measurements of a pixel and $\left(P^\dagger P\right)$ is the number of hits per pixel. This version of the equation is equivalent to a naive binning of the data in pixels. In the case of non-white noise, the map is still made by binning the data in pixels, except with a "whitening" filter, N^{-1} applied to the data.

The practical challenges involved in solving equation 2.2 are as follows. First, the matrix to be inverted is huge ($n_{pix} \times n_{pix}$, typically 100,000 $\times$ 100,000 for BOOMERANG) and involves considerable computational resources. Second, the noise correlation matrix must be estimated from the timestream data d_t itself because n_t is not a separately measurable quantity. Third, there are gaps in the data (due to cosmic ray hits or other glitches) which complicate estimation of the noise and filtering of the data.

An iterative scheme was developed [58] to address these problems. For each iteration, a noise time stream estimate is made by subtracting the signal estimate from the data time stream. Next, a noise correlation matrix and a correction to the previous map is constructed:

$$n^{(j)} = d - P\tilde{\Delta}^{(j)} \tag{2.4}$$

$$N^{(j)-1} = \langle n^{(j)} n^{(j)\dagger} \rangle^{-1} \tag{2.5}$$

$$\tilde{\Delta}^{(j+1)} - \tilde{\Delta}^{(j)} = \left(P^\dagger W P\right)^{-1} P N^{(j)-1} n^{(j)} \tag{2.6}$$

The initial map used is the unfiltered binned map:

$$\tilde{\Delta}^{(0)} = \left(P^\dagger P\right)^{-1} P^\dagger d \tag{2.7}$$

For computational speed, the filter W is taken to be the number of observations per pixel.

Gaps in the data are of particular concern when any filter is applied to the data because each unflagged sample is affected by the value of nearby flagged data. To deal with this issue, at each step in the iteration scheme, a new constrained realization of the measured noise is used to fill in the gaps. The flagged data are not used in the subsequent binning of the map.

A pixel-pixel noise correlation matrix is necessary for calculating the power spectrum from the map. This can be obtained from the noise time stream that is estimated with this iterative process:

$$N_{pp'} = \left(P^{\dagger} N_{tt'}^{-1} P\right)^{-1} \tag{2.8}$$

A map and a noise correlation matrix obtained in this way can be used in the subsequent power spectrum analysis.

2.2 Angular Power Spectrum

The temperature on the sky at each pixel p can be expanded in spherical harmonics:

$$\Delta_p = \sum_{\ell m} a_{\ell m} B_\ell Y_{\ell m}(\theta_p, \varphi_p) \tag{2.9}$$

where $Y_{\ell m}$ are the spherical harmonics and B_ℓ is the "window function" of the beam, or the pattern of the experimental beam in ℓ space. The correlation between signals is therefore:

$$S_{pp'} = \sum_{\ell m} \sum_{\ell' m'} \langle a_{\ell m} a_{\ell' m'} \rangle B_\ell B_{\ell'} Y_{\ell m}(\theta_p, \varphi_p) Y_{\ell' m'}(\theta_{p'}, \varphi_{p'}) \tag{2.10}$$

The fluctuations are assumed to be isotropic, meaning that $\langle a_{\ell m} a_{\ell' m'} \rangle = C_\ell \delta\ell\ell' \delta m m'$, so the signal correlations reduce to:

$$S_{pp'} = \sum_{\ell} \frac{2\ell + 1}{4\pi} C_\ell P_\ell(\chi_{pp'}) B_\ell^2 \tag{2.11}$$

where P_ℓ are the Legendre polynomials and $\chi_{pp'}$ is the angle between pixels p and p'. The coefficients C_ℓ completely characterize the temperature field on the sky and provide a model-independent way to compare measurements with models.

Because of incomplete sky coverage, C_ℓ cannot be determined independently for each ℓ. Therefore, the power spectrum is computed for ℓ-space bins. The sky coverage also determines the smallest ℓ (the largest angular scale) at which power can be measured.

The angular resolution of the experiment which makes the observations determines the maximum ℓ for which a power spectrum can be computed. The beam shape of the experiment determines the window function B_ℓ. The spherical harmonic transform of the beam

shape generally determines the cut-off in sensitivity due to the beam size. For example, a Gaussian beam profile with FWHM θ_C (in radians) yields a window function:

$$B_\ell^2 \approx \exp\left(\frac{-\ell(\ell+1)}{(\sqrt{8\ln 2}\theta_C^{-1})^2}\right) \tag{2.12}$$

The value of ℓ at which the sensitivity falls to half the maximum sensitivity is therefore:

$$\ell_c \approx \frac{\sqrt{8}}{\theta_C} \tag{2.13}$$

For example, the BOOMERANG experiment had an angular resolution of $10'$, therefore the half-power value of ℓ is ≈ 972.

The MADCAP software package [10] computes the power spectrum C_ℓ by using a Newton-Raphson method to determine the maximum likelihood power spectrum. A Gaussian probability distribution for the map given a particular power spectrum $\mathcal{C}$ is assumed:

$$P(m|\mathcal{C}) = (2\pi)^{-N_p/2}\exp\left(-\frac{1}{2}(m^T M^{-1} m + Tr[\ln M])\right) \tag{2.14}$$

where N_p is the number of pixels, m is the experimental map, and M is the matrix of average pixel-pixel correlations expected for the theoretical power spectrum $\mathcal{C}$. This leads to the following expression for the log likelihood which must be maximized to determine the best-fit power spectrum:

$$\mathcal{L}(C) = -\frac{1}{2}(m^T M^{-1} m + Tr[\ln M]) \tag{2.15}$$

If this function were quadratic, the correction δC_0 to an initial guess C_0 that would yield the peak likelihood would be:

$$\delta C_0 = -\left(\left[\frac{\partial^2 \mathcal{L}}{\partial C^2}\right]^{-1}\frac{\partial \mathcal{L}}{\partial C}\right)_{C=C_0} \tag{2.16}$$

$\mathcal{L}(C)$ is not a perfect quadratic function, so this correction is not strictly correct. Therefore, the correction to C_ℓ is iterated until δC_n is smaller than a desired precision.

2.3 Cosmological Parameters

In the context of cold dark matter (CDM) models, it is possible to use the measured C_ℓ to accurately determine cosmological parameters such as the baryon content of the universe (Ω_b), the total energy density of the universe (Ω), and the spectral shape of the primordial density fluctuations (n_s) [7].

Here, a maximum likelihood method is used to measure cosmological parameters. A database of model power spectra are created assuming a particular range of parameters. These are compared to the experimental measurements by evaluating a likelihood function for each model power spectrum which estimates the probability of this power spectrum given the measured power spectrum.

Given a set of parameters x with a prior probability distribution $P(x|prior)$ and a likelihood function of the parameters given the experiment $\mathcal{L}(x)$, the Bayes theorem gives the total probability distribution of the parameters:

$$P(x) \propto \mathcal{L}(x)P(x|prior) \tag{2.17}$$

If errors in the cosmological parameters $\delta x = x - x_0$ about the mean x_0 are small, then L can be quadratically expanded about the maximum:

$$L \approx L_m \exp\left(-\frac{1}{2}\sum_{ij} F_{ij}\delta x_i \delta x_j\right) \tag{2.18}$$

where F_{ij} is the Fisher information matrix, which is given by the derivatives of the CMB power spectrum with respect to the parameters x:

$$F_{ij} = \sum_\ell \frac{1}{(\Delta C_\ell)^2}\frac{\partial C_\ell}{\partial x_i}\frac{\partial C_\ell}{\partial x_j} \tag{2.19}$$

Offset-lognormal approximations to the Fisher information matrix [9] are used to compute the likelihood $L(x) = P(C_B|x)$ for each combination of parameters in the database.

Some parameters are not of interest and can be marginalized. Marginalized parameters can include cosmological parameters which are not of interest, or experimental parameters such as calibration uncertainty or beam measurement uncertainty. The marginalized likelihood distribution is given by multiplying L by the probability distribution of included

priors and integrating over the marginalized parameters x_m :

$$\mathcal{L} = P(x|C_B) = \int P_{prior}(x)L(x)dx_m \tag{2.20}$$

A global search for maxima of $\mathcal{L}$ is performed for the entire database. The average and $\pm 1\sigma$ points are determined by finding the location in the database at which the integral of $\mathcal{L}$ reaches 50%, 16% and 84% respectively of the value of the integral over the entire database.

Chapter 3 Instrument Design

This chapter describes the design of the BOOMERANG experiment. The experiment has the following requirements: a high sensitivity to Cosmic Microwave Background fluctuations and the rejection of spurious signals from the atmosphere, the ambient environment, and astrophysical sources.

In addition, all systems in the BOOMERANG payload must operate at balloon altitudes, which include very low ambient pressure and extreme temperature swings (varying from -50° C in the shade to +50° C in the Sun). The control systems in the payload must be autonomous for the 7-14 days of a long duration balloon flight.

The characterization of the instrument is described in Chapter 4.

3.1 Telescope and Gondola

The telescope is designed to smoothly scan in azimuth at fixed elevation, and has an attitude control system similar to those described in [11], [12], and [13]. The azimuth pointing of the telescope is controlled by two torque motors (Inland QT6205d); the first torques a large flywheel, the other torques against the steel cables connecting the payload to the balloon. The two motors provide enough torque to move the gondola in azimuth and to correct for random rotation of the balloon. The elevation of the telescope can be controlled by tipping the inner frame with a DC gear motor. An overview of the gondola frame is shown in Figure 3.1. The control hardware consists of two redundant 386 CPU's. A watchdog circuit switches control of the pointing from one CPU in a few milliseconds in case of a reboot.

Pointing information is provided by a differential GPS array, a two-axis Sun sensor, an encoder on the elevation axis, and three orthogonal axis laser rate gyroscopes. The azimuth gyroscope provides velocity feedback for controlling the scan of the telescope. The absolute pointing data from the Sun sensor is used to reset the drift in the gyroscopes and to provide data for post-flight attitude reconstruction.

This set of pointing sensors provides no good measure of absolute roll angle about the Sun vector, so we rely on the gyroscopes to measure absolute roll. Future upgrades

of BOOMERANG will include a star tracking camera with the proper filter to operate in daytime.

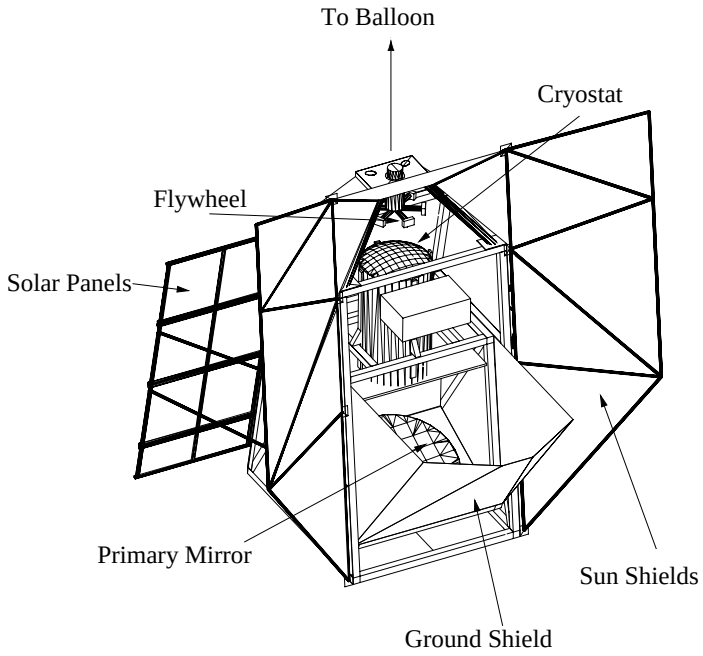

Figure 3.1:
An overview of the BOOMERANG gondola.

3.2 Thermal Design

The extreme conditions of the balloon-borne observation platform require some care in the thermal design of the payload. Electronics must not be allowed to get too hot or too cold to function. More importantly, the cryostat must not reach a temperature at which O-rings freeze, which could lead to a leak. The cryostat O-rings are made from Buna-N rubber, which freeze at temperatures below $\sim$ -50° C.

The outside of the gondola is covered with $1''$ thick open-cell styrofoam panels (Dow extruded polystyrene "blue foam") with 50 μm mylar bonded to 25 μm thick aluminum foil. With the mylar side facing outwards, the combination of layers provides high reflectivity in the optical band and high emissivity in the infrared band, thus protecting the payload from excessive solar heating.

A thermal model which included heat transfer by conduction and radiation was con-

structed for the payload. Two cases were considered for the input power– "cold" and "hot." The cold case assumed that the payload is over water and receives 1044 W/m^2 radiation from the Sun and a 9% albedo for the surface of the Earth for 177 W/m^2 of power. The hot case assumed that the payload is above fresh snow and receives 1397 W/m^2 radiation from the Sun and 213 W/m^2 from the Earth with an albedo of 95%. Table 3.2 shows the predicted range of temperatures for a few of the key experimental components. All electronics were expected to maintain reasonable temperatures during the flight, as was the cryostat.

Item	Predicted Temperature °C
Attitude Control System	-8° to 12°
Data Storage System	17° to 27°
Data Acquisition System	-7° to 6°
Cryostat	-29° to 27°
Bolometer Readout Electronics	-31° to 2°
Solar Array	55° to 92°

Table 3.1:
Predicted equilibrium temperatures for electronic components of the payload.

3.3 Cryogenics

The cryogenic system for BOOMERANG keeps the detectors at an operating temperature of 0.28 K for the entire two weeks of an LDB balloon flight. It has 60 liters of volume at 2 K to contain the photometers, re-imaging optics, baffles, and cold preamplifiers. The system is composed of a self-contained sorption-pumped ^{3}He refrigerator [37] and a helium/nitrogen main cryostat [38]. The ^{3}He fridge contains 40 liters STP of ^{3}He and runs at 0.280 K with a load of 27 μW. The main cryostat holds 65 liters of liquid nitrogen and 60 liters of liquid helium. The tanks, toroidal in shape, are suspended by means of Kevlar cords. Radiation from the 300 K ambient environment to the 77 K tank is shielded by a blanket of superinsulation aluminized mylar (30 layers). The 77 K tank contains copper braid to maintain cryogenic thermal contact in the event of the nitrogen freezing. Radiation from the 77 K tank to the helium tank is shielded by an intermediate temperature shield cooled to < 20 K by the ^{4}He vapor from the helium tank.

Due to the complex geometry of the vent lines, the pumpdown of the helium bath is

plagued with thermo-acoustic oscillations, making it necessary to pump the bath down in a controlled manner over the course of 12 hours. Therefore, BOOMERANG is launched with the helium bath already at low pressure. External plumbing with electrically actuated valves is used to pressurize the nitrogen bath during the flight and to maintain the low pressure of the helium bath during ascent. At float altitude the helium valve is opened for the remainder of the flight.

3.4 Optics

The BOOMERANG telescope consists of an ambient temperature (-20° C in the shade at float altitude) off-axis paraboloidal primary mirror which feeds a pair of cold re-imaging mirrors inside the cryostat. The primary mirror is 1.3 m in diameter and has a 45° off-axis angle for a projected size of 1.3 × 1.2 m. The mirror can be tipped in elevation by +10° and −12° to cover elevation angles from 33° to 55°. Radiation from the sky is reflected by the primary mirror and passes into the cryostat through a thin (50 μm) polypropylene window near the prime focus. The window is divided in two circles side by side, each 6.6 cm in diameter. Filters to reject high frequency radiation and to reduce the thermal load on the 2 K and 0.3 K stages of the cryostat are mounted on the 77 K and 2 K shields in front of the cold mirrors. These are capacitive multilayer metal mesh low pass filters [72] with cutoffs at 540 GHz and 480 GHz respectively. Neutral density filters with transmission of 1.5% used to reduce the loading on the detectors for ground testing are mounted on a mechanism which can move the filters in and out of the beam near the prime focus. See Figure 3.2 for an overview of the optics.

The off-axis ellipsoidal secondary and tertiary mirrors are surrounded by black baffles and re-image the prime focus onto a detector focal plane with diffraction-limited performance at 1 mm over a 2° × 5° field of view.

The re-imaging optics form an image of the primary mirror at the 10 cm diameter tertiary mirror. The size of the tertiary mirror limits the illumination of the primary mirror to the central 50% in area to reduce sidelobe response.

The secondary and tertiary mirrors are ellipsoidal reflectors with effective focal lengths of 20 cm and 33 cm. The mirror surface shapes have been optimized with Code V software [42]. The prime focus is fed at f/2, so the detector focal plane is fed at f/3.3. The tertiary

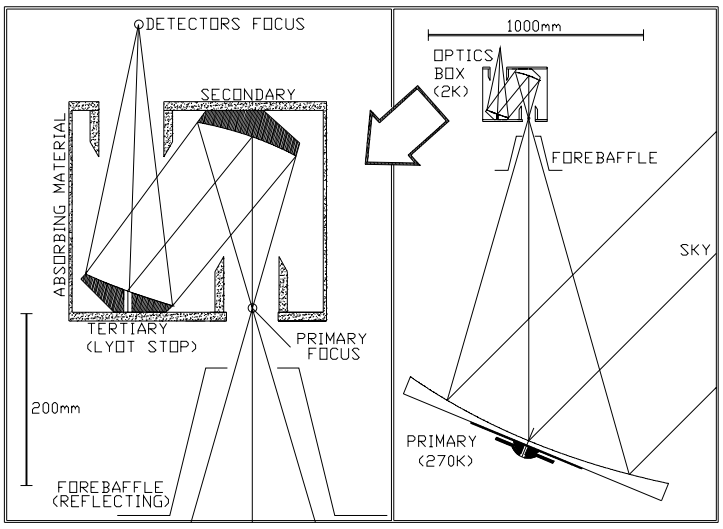

Figure 3.2:
An overview of the BOOMERANG optics.

mirror is 10 cm in diameter, corresponding to an 85 cm diameter aperture on the 1.2 m diameter primary.

The BOOMERANG focal plane contains a combination of four single-frequency channels fed by smooth-walled conical horns and four multicolor photometers fed by parabolic concentrators (Winston horns). Although the image quality from the optics is diffraction limited at 150 GHz over a $2^\circ \times 5^\circ$ field, all of the feed optics are placed inside two circles 2° in diameter, separated center to center by 3.5°. The focal plane area outside these circles is vignetted by blocking filters at the entrance to the optics box and on the 77 K shield and is unusable. Due to the curvature of the focal plane, the horns are placed at the positions of the beam centroids determined from geometric ray tracing. All of the feeds are oriented towards the center of the tertiary mirror.

A schematic of the relative positions and sizes of the beams on the sky is shown in Figure 3.3. The focal plane layout was chosen so as to repeat observations of the same part of the sky on many different time scales. The telescope scans in azimuth, and at 1°/s at 45° elevation, channels on opposite sides of the focal plane will observe the same sky ~ 2 s apart. The rotation of the sky above Antarctica allows each row of detectors to observe the same patch of sky ~ 30 minutes apart.

All physical joints in the focal plane were sealed with vacuum grease blacked by a small

admixture of carbon lampblack to assist in the rejection of stray high-frequency light.

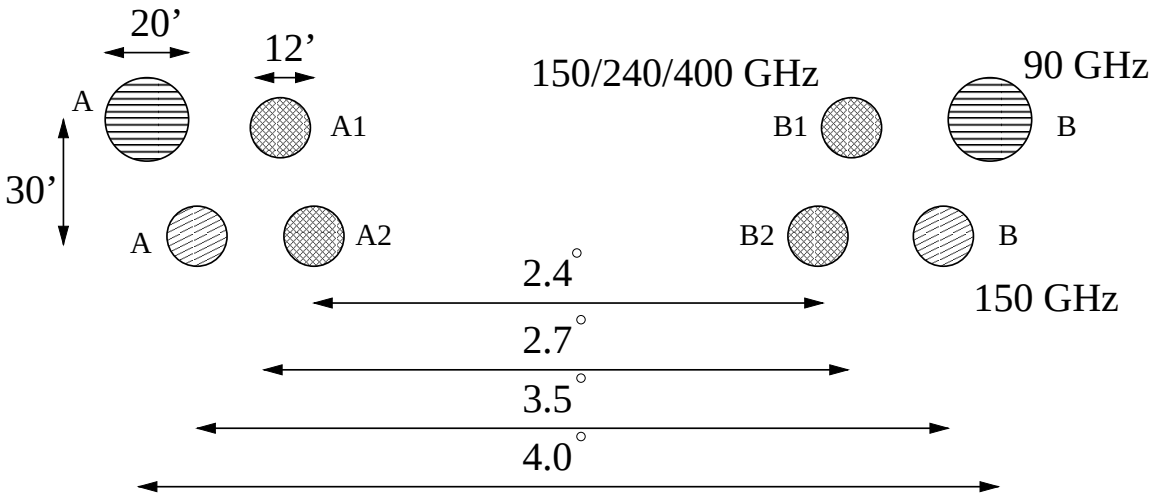

Figure 3.3:
The BOOMERANG focal plane projected onto the sky. The labels “A,” “B,” “A1,” “A2,” “B1,” and “B2” are designations for each of the channels.

3.5 Bandpass Selection

The BOOMERANG bands were chosen to provide a wide enough frequency coverage that CMB fluctuations can be unambiguously measured and foreground sources of signal can be separated from contaminants. See Figure 3.4 for a comparison of the four bandpasses selected with the spectra of the foreground contaminants: synchrotron radiation [65], free-free emission [46], and thermal emission from dust [21]. Despite the small atmospheric optical depth at balloon float altitude, strong atmospheric absorption lines were avoided. Bands centered at 90 GHz, 150 GHz, and 240 GHz were selected to measure primarily CMB anisotropy, and a fourth band at 400 GHz was chosen to monitor thermal dust emission, which was expected to be the most important contaminant.

3.6 Single Mode Feed

The focal plane contains four single frequency channels; two at 90 GHz and two at 150 GHz (see Figure 3.3). The feeds follow the Planck HFI prototype design [15]. The dual-polarization feed structures are designed to provide compactness, reduced thermal load on the 0.3 K stage, high efficiency, and excellent control of frequency and spatial response.

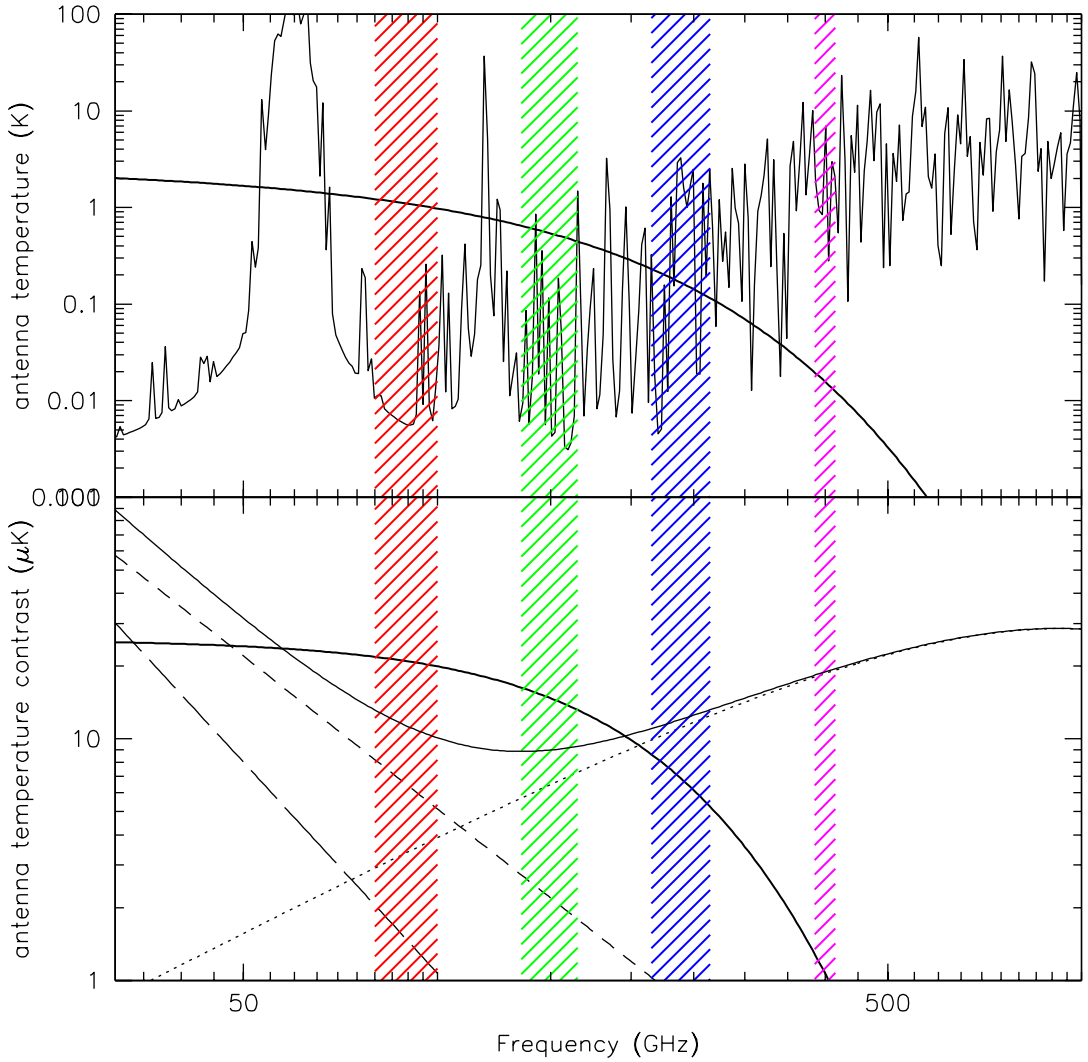

Figure 3.4:
The BOOMERANG bands compared with spectra of sources on the sky. The upper panel shows a model of the atmosphere at balloon float atmosphere (HITRAN model, http://www.hitran.com). The thick line shows the spectrum of the CMB. The lower panel compares the spectrum of CMB anisotropy with various galactic foregrounds. The heavy solid line shows the spectrum of a CMB anisotropy. The small-dashed line shows the spectrum of free-free radiation, the large-dashed line shows the spectrum of synchrotron radiation, and the dotted line shows the spectrum of thermal dust emission. The light solid line shows the sum of the three galactic components. In each panel, the hatched columns show the selected BOOMERANG bands.

The entrance feeds are smooth-walled conical feeds designed to illuminate the tertiary mirror with a -5dB edge taper. Using Gaussian optics, the desired edge taper defines the

beam waist at the phase center of the horn, which in turn defines a relation between the horn aperture diameter and the horn length as follows.

For a smooth walled conical feed, the beam waist at the aperture is $w_a = 0.768a$, where a is the aperture radius. For a horn propagating a single Gaussian mode, the waist diameter at the phase center is

$$w_0 = w_a \sqrt{1 + \left(\frac{\pi w_a^2}{\lambda L}\right)^2} \tag{3.1}$$

where L is the length of the horn. The waist size as a function of distance z from the phase center is given by:

$$w(z) = w_0 \sqrt{1 + \left(\frac{z\lambda}{\pi w_0^2}\right)^2} \tag{3.2}$$

The horn aperture size is then determined by requiring a desired edge taper at the Lyot stop. Let the Lyot stop have radius r_L and distance z_L from the phase center. The edge taper is:

$$T = 10 \log_{10} \exp\left(\frac{-2r_L^2}{w^2(z_L)}\right) \tag{3.3}$$

Specifying the edge taper T yields a beam waist at the Lyot stop:

$$w(z_L) = r_L \sqrt{\frac{8.686}{T(dB)}} \tag{3.4}$$

Solving for w_0, a range of aperture sizes (a) and horn lengths (L) are specified:

$$L = \frac{\pi w_a^2}{\lambda} \sqrt{\left(\frac{w_a}{w_0}\right)^2 - 1} \tag{3.5}$$

The solution with minimum length is selected, which gives diameters of 19.66 mm and 11.8 mm and flare angles of 19.7° and 10.5° for the 90 GHz and 150 GHz structures.

At the throat of the entrance feed, a 3λ length of waveguide with a radius $r = 0.35\lambda$ defines the low frequency edge of the passband and sets the throughput of the feed structure such that only the lowest order Gaussian mode is propagated through the rest of the system. For the 90 and 150 GHz structures, 2.54 mm and 1.33 mm diameter guides define cutoffs at 69 GHz and 132 GHz, respectively.

Capacitive metal mesh filters define the upper edge of the band [72] [34]. Each of these has high-frequency leaks at twice and three times the cutoff frequency and must be used in combination with another filter which blocks the leaks. In the 150 GHz feeds, filters with cutoffs at 168 GHz and 198 GHz are used, and in the 90 GHz feeds, 99 GHz and 177 GHz filters are used. An f/4 re-expanding feed re-emits the light through the filters and an identical re-concentrating feed concentrates the light into the bolometer cavity. An alkali-halide/carbon layered polyethylene filter [74] blocks infrared and optical light ($\nu >$ 1650 GHz) and is tuned in thickness to maximize transmission at the center of the band.

Identical low density polyethelylene hyperbolic lenses are placed at the aperture of each of the two face-to-face horns. The focal length of the lenses is set to maximally match the lowest order Gaussian mode propagating from each of the horns through the intervening filters in the thin lens approximation.

A re-entrant black baffle heat sunk to the 1.8 K stage surrounds the gap between the two horns, preventing stray light from entering the optical system. The inner surface of the baffle is painted with Bock black [6].

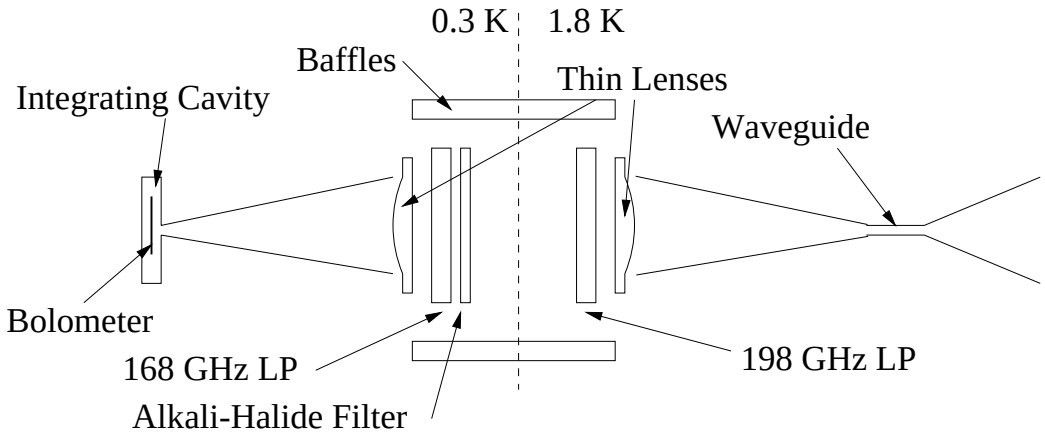

Figure 3.5:
Schematic of a 150 GHz single frequency feed structure.

3.7 Multi-color Photometer

The focal plane for the Antarctic LDB flight of BOOMERANG contains 4 three-color photometers (see Figure 3.6) similar to those used in SuZIE [45], MAX [22], and the FIRP on IRTS [33]. These structures have the advantage of simultaneous observation of the same

region of sky through the same column of atmosphere in three frequency bands.

The photometers are fed by back-to-back parabolic concentrators (Winston horns) mounted on the 2 K stage. The input horn is set at f/3.4 to maximally couple to the re-imaging optics. The horn has an entrance aperture diameter of 1 cm producing a $12'$ beam on the sky, corresponding to the diffraction limit at 150 GHz. The horn has a short flare in the shape of a 45° section of a circle with a diameter of 1.3 cm to reduce sidelobes at low frequency.

The throughput of the photometer is defined by the 1.45 mm diameter exit aperture of the Winston horn to be 0.05 cm^2 sr. The re-expanding Winston horn has an aperture which matches light pipe located on the 0.3 K stage across a 0.5 mm gap. At the entrance to the light pipe, there is a metal mesh lowpass filter with a cutoff of 480 GHz to improve the out-of-band rejection.

In the light pipe, two dichroic filters tipped 22.5° off-axis direct light at frequencies greater than 270 GHz and 180 GHz through inductive multi-layer metal mesh bandpass filters which pass 400 GHz and 240 GHz, respectively. Radiation at frequency less than 180 GHz is transmitted through the two dichroics and through a 150 GHz bandpass filter. Parabolic horns concentrate the light into integrating bolometer cavities where it is detected.

3.8 Calibration Lamp

A 1 cm diameter hole located in the center of the tertiary mirror contains a handmade micromesh bolometer with copper leads for use as a calibration lamp. An NTD-4 chip provides high impedance at 2 K. The electronics send a fixed current on the order of a few microamps through the bolometer for 1 second every 13 minutes which provides an optical source to be used as a transfer calibrator.

The calibration lamp was used to determine the detector bias at which maximum optical responsivity occurs and to track drifts in responsivity during the flight.

3.9 Detectors

BOOMERANG uses silicon nitride micromesh "spider web" bolometers developed at Caltech and JPL [43] (Figure 3.7) specifically for use in an environment with a high cosmic ray flux,

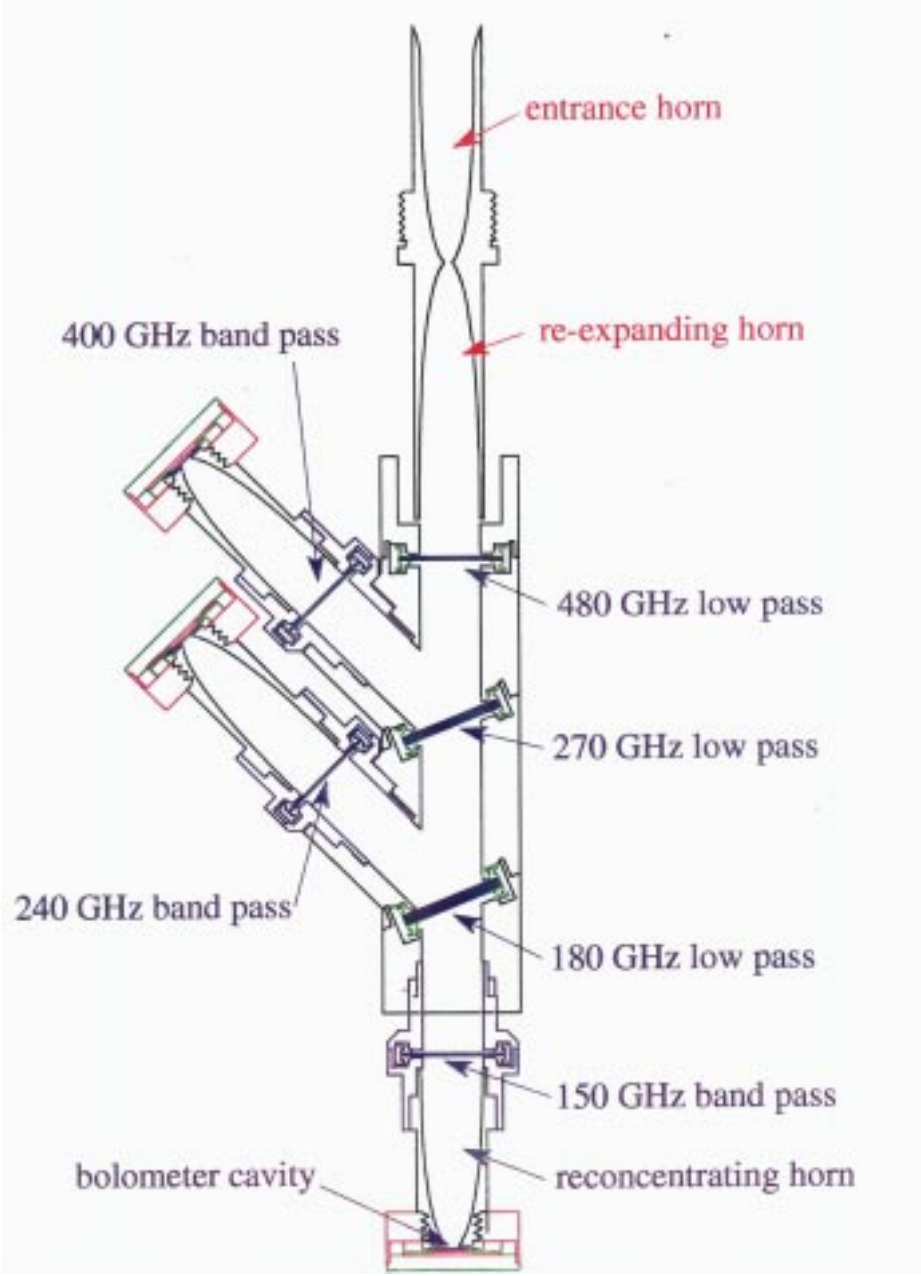

Figure 3.6:
Schematic of the BOOMERANG multi-color photometer.

such as above the Earth's polar regions. The bolometer absorber consists of a silicon nitride mesh rather than a solid. A Neutron Transmutation Doped (NTD) germanium thermistor is used to measure the temperature rise of the absorber.

The fundamental limit of the sensitivity of a bolometer is the phonon shot noise in the thermal link between the absorber and the bath [40]. The BOOMERANG detectors

Figure 3.7:
A bolometer used by BOOMERANG. The web absorber shown here is 4 mm in diameter. The entire ring is $3/4''$ in diameter.

ν_0 (GHz)	n	d (mm)	s (μm)	G (pW/K)	τ (ms)
90	2	5.6	400	60	24
150	6	3.4	425	60	15
240	4	4.0	150	180	10
400	4	4.0	150	360	6

Table 3.2:
BOOMERANG bolometer design parameters, including the web diameter d, the grid spacing s, the target thermal conductance, G and target time constant, τ.

use semiconductor thermistors, so Johnson noise is also a contributor to the overall noise. In this case the Noise Equivalent Power $NEP = \gamma\sqrt{4k_BT^2G}$, where G is the thermal conductance, T is the bath temperature, and $\gamma \sim 1.2$ for our choice of thermistor material. For a given background load, Q, maximum sensitivity is achieved for $G \sim Q/T$. The desired time constant of a bolometer $\tau \sim C/G$ for a given modulation scheme sets a limit on the minimum thermal conductance that can be selected. The bolometers are optimized for a 10 K RJ spectrum background using the optimization scheme of [26], and the resulting parameters and the web diameter (d) and grid spacing (s) are listed in Table 3.9.

3.10 Integrating Cavity

Since an electric field goes to zero at the surface of a conductor, a naive guess would place the bolometer absorber at a distance $\lambda/4$ from the exit aperture of the reconcentrating horn and at a distance $\lambda/4$ from a backshort in order to maximize the electric field in the cavity at the absorber. Simulations of a bolometer cavity using the HFSS software package (Hewlett-Packard) show that the $\lambda/4$ distance is indeed correct [24].

3.11 Readout Electronics

The slow scan observation scheme requires stability of the detector and the readout electronics from the bolometer thermal cutoff frequency ($\sim$ 10 Hz) down to the characteristic scan frequency at tens of mHz. The detector readout scheme implements an electronic modulation/demodulation technique to provide stability at low frequency, by moving the signal bandwidth well above the 1/f knee of the JFET and the warm electronics. Modulation is achieved by biasing the bolometer with AC current, hence modulating its responsivity by a known periodic function.

The detectors are AC voltage biased with a 318 Hz sine wave. Dual 10 MΩ load resistors provide an approximate current bias. The signal from each detector passes through a JFET source follower circuit on the 2 K stage. It provides gain of the bolometer signal power, thus reducing the susceptibility to microphonics. The JFETs were selected for low power dissipation and are packaged by IR Labs (IR Labs TIA).

The signal from the cold JFETs passes through a preamplifier stage and a Band Pass Filter stage prior reaching the synchronous detector. The synchronous demodulator (Lock-In) multiplies the signal synchronously by +1/-1 times the bias reference. A 4-pole Butterworth low pass filter with cutoff at 20 Hz removes the high-frequency terms of the product and acts as an anti-aliasing filter for the Data Acquisition System (DAS). An AC-coupling high pass filter with a cutoff at 0.016 Hz and extra gain is applied to the signal to match the signal dynamics to the DAS dynamic range.

Including the cold JFETs, the entire readout electronics contribute less than $10nV_{rms}/\sqrt{Hz}$ to the signal noise in the frequency range of 0.016 Hz to 20 Hz. The AC-coupled signals are sampled by the DAS at 60 Hz. A block diagram of the electronics is shown in Figure 3.8.

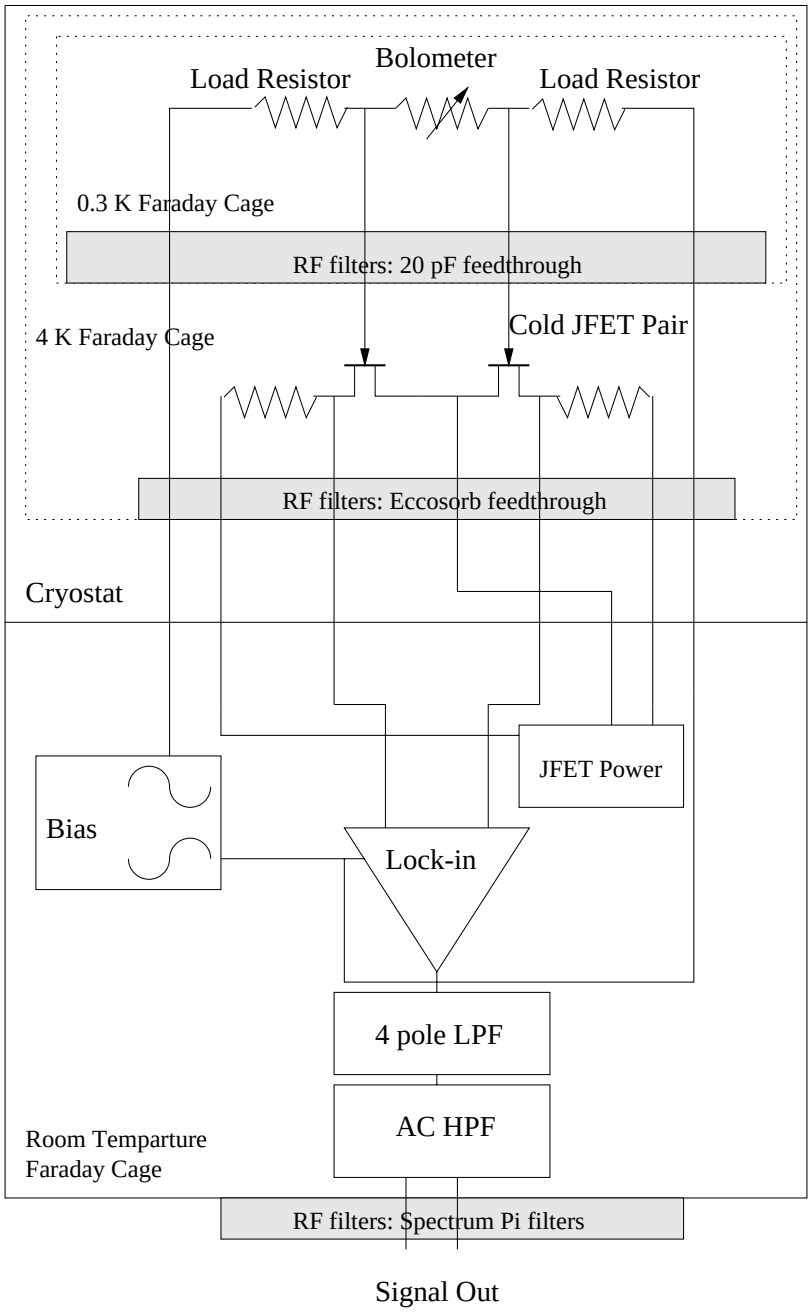

Figure 3.8:
A schematic of the BOOMERANG readout electronics.

3.12 Rejection of RF and Microphonic Pickup

Bolometric detectors are susceptible to spurious heating from RF dissipated in the thermistor or to pickup from microphonic response of the bolometer or wiring. This is especially of concern at the high impedance portion of the wiring between the bolometer and the cold

JFET source followers. There are several microwave transmitters for satellite communications on board the BOOMERANG payload which are potentially sources of RF pickup in the bolometers. The frequencies of concern are an ARGOS transmitter at 400 MHz and a TDRSS 2.3 GHz transmitter.

To guard against degradation of the detector performance, the bolometer cavity defines a Faraday cage into which the only entrance is through the feed horn. Interfering RF is kept out of this entrance path by the waveguide cutoff in each feed. The wires exit the cavity through surface mount 20 pF feed-through capacitors to ground mounted on the wires exiting the Faraday cage which provide protection from RFI close to the detector. All bolometer leads from the JFET preamp stage to the warm amplifiers run through cast eccosorb filters. The cast eccosorb filters consist of stripline cables potted in cast eccosorb (EV Roberts CR-124) and have significant attenuation above a few GHz. These provide the only exit from a second Faraday cage surrounding the 2 K stage.

A third Faraday cage surrounds the bolometer, cryostat electronics and wiring. The amplified signals are fed through Spectrum Π filters (Spectrum 1212-0502) to the DAS.

The low suspended mass of the micromesh bolometers naturally provides a reduction in microphonic response (measured resonant frequency >1 kHz); however, care was taken to securely tie down the high impedance wiring connecting the bolometers to the JFET follower stage. The wiring on the 0.3 K stage consists of 27 AWG shielded twisted pair which was strapped down with Teflon tape and nylon cord. Between the 0.3 K and 2 K stages, cables made with low thermal conductivity 50 μm manganin wire were strapped to the vespel posts. Inside the JFET box, all high impedance wires were potted in silicone RTV.

Chapter 4 Instrument Characterization

This chapter describes the testing of the receiver components described in Chapter 3, both as separate components and as an integrated receiver. Appendix A contains a summary of bolometer parameters, measured both pre-flight and in-flight.

4.1 Optics Testbed

A testbed was set up to test various optical components, including the in-band transmission of the blocking filters, the transmission of the optics box, and the beam pattern of the feed horns. The testbed consisted of a dewar with a 300 mK bolometer fed by a Winston horn and a universal mount on the outside of the dewar window to which any horn to be tested could be mounted. The bolometer was run in two different filter configurations; 90 GHz to test the 90 GHz single mode feed, and 150 GHz to test the 150 GHz single mode feed and the multi-color photometer feed at 150 GHz. In both cases, the above band leak was measured with a thick grill filter to be less than 5%. The testbed achieved a Noise Equivalent Power (NEP) of $\sim 10^{-15}$ W/$\sqrt{Hz}$ with a bolometer with a thermal roll-off at 5 Hz.

4.2 Blocking Filters

The in-band transmission of the blocking filters was measured at two difference angles of incidence using the optics testbed and a chopped 77 K blackbody. The band-integrated transmission of the filters were measured at f/2 by mounting them in their proper position in the optics box, and at f/3.3 by placing the filters directly between the feed and the source. In both the 150 GHz and 90 GHz cases, the filters had higher in-band transmission at higher f/ number. This is due to the fact that there are more off-axis rays in a low f/ number beam and the effective thickness seen by these rays is different than that of the on-axis rays. See Table 4.2 for a summary of the results.

The predicted in-band transmission at 150 GHz of the combination of filters is approximately 95%, in good agreement with this measurement.

The thickness of the alkali-halide filter (1650 GHZ LP) measured in the testbed was

Filter	Type	150 GHz f/2	150 GHz f/3.3	90 GHz f/2	90 GHz f/3.3
480 GHz LP	metal mesh	0.95	0.96	0.94	0.96
540 GHZ LP	metal mesh	0.98	0.98	0.95	0.94
1650 GHZ LP	alkali-halide	0.94	0.95	0.81	0.85
total		0.88		0.69	

Table 4.1:
The in-band transmission of the three blocking filters measured in the optics testbed.

designed for maximum transmission at 150 GHz, which is near minimum transmission at 90 GHz. As seen in Table 4.2 it is readily apparent that including the alkali-halide filter takes away a large amount of optical efficiency. Due to these tests, it was decided to use smaller filters and place them within each feed structure, so that the thickness could be optimized for each frequency.

4.3 Beam Maps of Horns

The main lobe response of the feed horns was mapped using two methods. First, a two-dimensional map was made using a 200° C source viewed through a 19 mm aperture at a distance of 15 cm from the feed mounted on the front of the optics testbed cryostat. Second, a one-dimensional slice of the beam pattern was made using a 900° C blackbody source viewed through a 25 mm aperture at a distance of 28 cm from the feed. The 2D maps were made to a noise-limited sensitivity of around -15 dB from the peak, while the 1D maps achieved a sensitivity of -20 dB of the peak signal.

Two corrections were made to the data. First, a view factor of the cosine of the off-axis angle was removed. A correction was then made for the angular size of the source. All of the beams were well fit by a Gaussian as expected for a horn which propagates a single mode. These corrections reduced the measured beam FWHM by 7-8%. See Table 4.3 for a summary of the corrected beam size and the edge taper at the tertiary mirror. Figure 4.1 shows the beam maps of the entrance feed. Vertical lines indicate the location of the edge of the tertiary mirror. The measured edge taper at the tertiary agrees well with the design edge taper of -5dB.

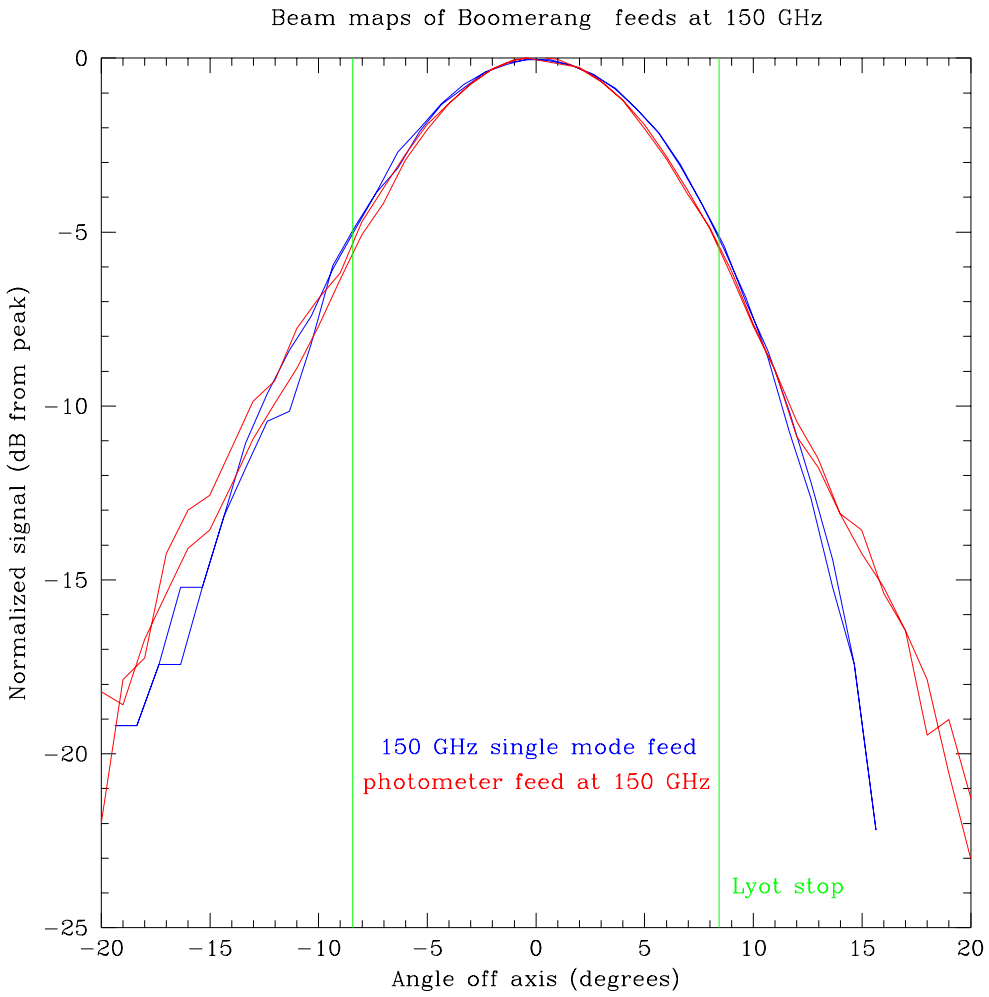

Figure 4.1:
Beam maps of the two 150 GHz entrance horns. The vertical lines indicate the edge of the tertiary mirror. The design edge taper is -5dB.

Horn	FWHM (degrees)	FWHM (cm on tertiary)	edge taper on tertiary (dB from peak)	design edge taper (dB from peak)
90 GHz	16.5	9.8	-4.5	-5
150 GHz sm	11.0	6.4	-6.4	-5
150 GHz mm	11.2	6.5	-6.1	-5

Table 4.2:
The measured beam size and tertiary edge taper of three feed horns.

4.4 Optics Box

The integrated truncation of the beam of the Lyot stop was measured by viewing the chopped source with the horn and optics testbed mounted in its position on the focal plane

of the optics box. This signal was compared to the signal from the source observed without the optics box intervening.

The transmission of the optics box was also measured with the blocking filters in place. See Table 4.4 for a summary.

Position	90 GHz	150 GHz	90 GHz + filters	150 GHz + filters
90A	0.68	0.65	0.47	0.57
150A	0.65	0.66	0.45	0.58
90B	0.68	0.66	0.47	0.59
150B	0.64	0.67	0.44	0.58
A1		0.77		0.68
A2		0.76		0.67
B1		0.76		0.67
B2		0.79		0.70

Table 4.3:
The measured transmission of the optics box with feeds mounted in the eight positions, with and without the blocking filters installed. The first four rows of the 150 GHz column are using data from the single mode feed and the last four are using data from the multimode feed.

The multimode feed transmits better through the optics box than the single mode feed, despite the fact that their beam patterns are virtually identical. This is due to the fact that the single mode feeds view the tertiary at a larger off-axis angle and therefore view a smaller effective mirror area than the multimode feeds.

4.5 Feed Testbed

The full feed structures were tested in a dewar with a 300 mK bolometer. The dewar was configured in three different ways; with the multi-color photometer, the 90 GHz single mode feed and the 150 GHz single mode feed. The front-end blocking filters were identical to those used in the final BOOMERANG receiver. The bolometer used in the optics testbed was used in the feed testbed.

A 77K thermal source was often used as a measurement source; this consisted of eccosorb soaked in a bath of LN_2. A styrofoam bucket containing a piece of eccosorb large enough to fill the entire beam was used. A large chopper wheel at room temperature with eccosorb mounted on the blades was used to modulate the signal.

4.6 Optical Efficiency of Feed Structures

Optical efficiency of each of the feed structures was measured by comparison of two I-V curves viewing loads at two different temperatures (77 K and 300 K). See Figure 4.2 for two load curves measured with the 150 GHz single mode feed. At equal bolometer resistances (equivalent to equal bolometer temperatures), the total power dissipated in the bolometer is equal:

$$R^{77} = R^{300} \tag{4.1}$$

$$T^{77} = T^{300} \tag{4.2}$$

$$\frac{P_e^{77} + Q_{opt}^{77}}{G} = \frac{P_e^{300} + Q_{opt}^{300}}{G} \tag{4.3}$$

where the superscripts 77 and 300 refer to the thermal load temperature, R is the bolometer resistance, G is the thermal conductance, T is the bolometer temperature, Q_{opt} is the incident optical power, and P_e is the electrical power dissipated in the bolometer. Since the thermal conductivity is a function of temperature, it is equal in the two cases. Therefore, the difference in electrical power (P_e) between the two cases is equivalent to the difference in incident optical power (Q):

$$P_e^{77} + Q_{opt}^{77} = P_e^{300} + Q_{opt}^{300} \tag{4.4}$$

$$Q_{opt}^{77} - Q_{opt}^{300} = P_e^{300} - P_e^{77} \tag{4.5}$$

The assumption that equal bolometer resistance implies equal bolometer temperature breaks down in the case where the "electric field effect" contributes to the bolometer resistance. In this regime, the bolometer resistance becomes a function of voltage as well as temperature:

$$R = R_0 \exp\left(\sqrt{\frac{\Delta}{T}} - \frac{BV}{T^{m+1}}\right) \tag{4.6}$$

where Δ, R_0, and B are constant parameters dependent on the NTD material, V is the bolometer voltage, and T is the bolometer temperature. In normal operation, only the

first term in the exponential contributes. If the second term contributes, however, an equal resistance does not imply an equal temperature. A test for this effect is to measure the difference in electrical power at several different bias voltages and to check that the difference in power is equal.

The predicted difference in optical power can be determined by integration of the blackbody curve:

$$\Delta Q = A\Omega \left(\int B_\nu(300K) t_\nu d\nu - \int B_\nu(77K) t_\nu d\nu \right) \tag{4.7}$$

where $A\Omega$ is the throughput of the feed, B_ν is the blackbody function, and t_ν is the bandpass function of the filters. The measured difference in power is compared to this predicted incident power to determine an optical efficiency.

With this method, the 150 GHz and 90 GHz feed structures are found to have optical efficiencies of 42% and 36%, respectively, while the multi-color photometer channels are found to have efficiencies of 27% and 23% at 150 GHz and 240 GHz, respectively. The optical efficiency at 400 GHz was not measured until the photometers were integrated into the flight receiver.

Combining the measurements of the feed structure optical efficiency with the measurements of the transmission of the optics box provides a prediction of the optical efficiency of each BOOMERANG channel. For the single mode channels, 24% is expected at both 90 GHz and 150 GHz. In the multi-color photometer, 18% and 15% efficiencies are expected at 150 GHz and 240 GHz, respectively.

4.7 Characterization of Neutral Density Filters

The neutral density filters (NDF) used in BOOMERANG consist of a lightly metallized thin (25 μm) film of polyethylene mounted in an aluminum ring. The ring is "wedged" so as to tip the film at a small angle relative to the principal optical axis to avoid the creation of reflective cavities in the optics.

Measurement of the transmission of the NDF using the BOOMERANG bolometric photometers is difficult because the optical power difference between the filtered and unfiltered cases is large and non-linearity in the responsivity of the bolometer is an important effect. The expected transmission of the NDF is on the order of one or two percent; therefore, the

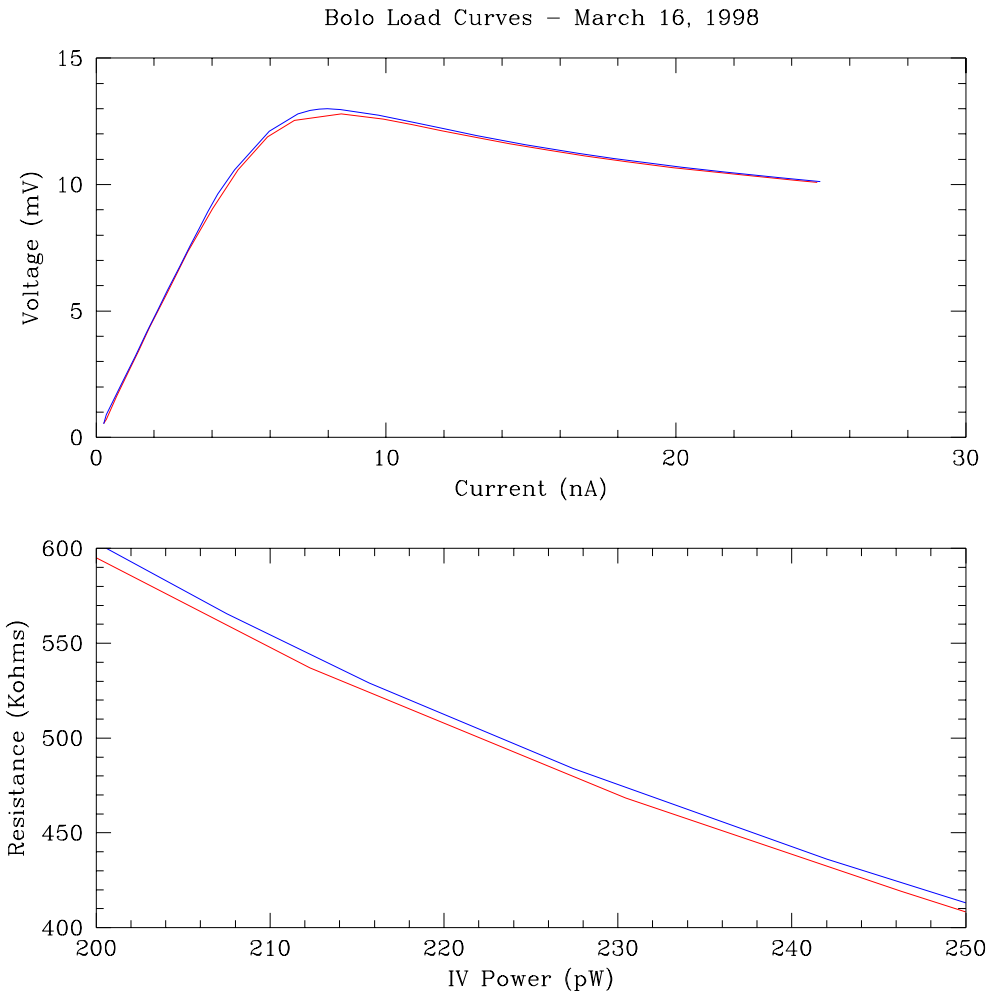

Figure 4.2:
Comparison of load curves of the 150 GHz single mode feed with the bolometer viewing a 77 K load (blue curve) and a 300 K load (red curve) through the neutral density filter. The upper panel shows current versus voltage. The lower panel shows electrical power versus resistance. The difference in electrical power is found to be 1.5 pW. The predicted power difference is 224 pW times the neutral density filter's transmission of 1.6%, yielding an optical efficiency measurement of 42%. The difference in power is independent of the bias voltage, showing that the electric field effect is not contributing.

optical power incident on the bolometer is a factor of 50 to 100 different between the filtered and unfiltered cases. To bypass the non-linearity problems, the bolometer was biased with enough electric power that the change in optical power was tiny ($\sim 1\%$ of the electric power) in comparison, thereby keeping the bolometer at the same responsivity in both the filtered and unfiltered cases.

The test spanned two separate days and used the feed testbed configured with a BOOM-

ERANG multi-color photometer. On the first day, the bolometers viewed the chopped 300 K/77 K source directly. On the second day, the bolometers viewed the source through the NDF, which was mounted on the 2 K stage in the feed testbed. The signals were measured at a range of bolometer bias powers and compared between days.

The background optical load on the 150 GHz bolometer is estimated to be 150 pW without the NDF in the beam and 2 pW with the NDF in the beam. The bias on the detector was increased so that the electrical power dissipated in the detector is at least a factor of 100 greater than the optical power difference.

Figure 4.3 shows the measured transmission as a function of bolometer bias power. The transmission at each of the frequencies 150, 240, and 400 GHz were measured. At large bias, the results become independent of bias, showing that non-linearities in the detectors were overcome. This particular filter shows a transmission of 1.5%. The scatter in the measured transmission show that the results are good to $\sim$ 20%. Additionally, the transmission of the NDF is seen to be independent of electromagnetic frequency.

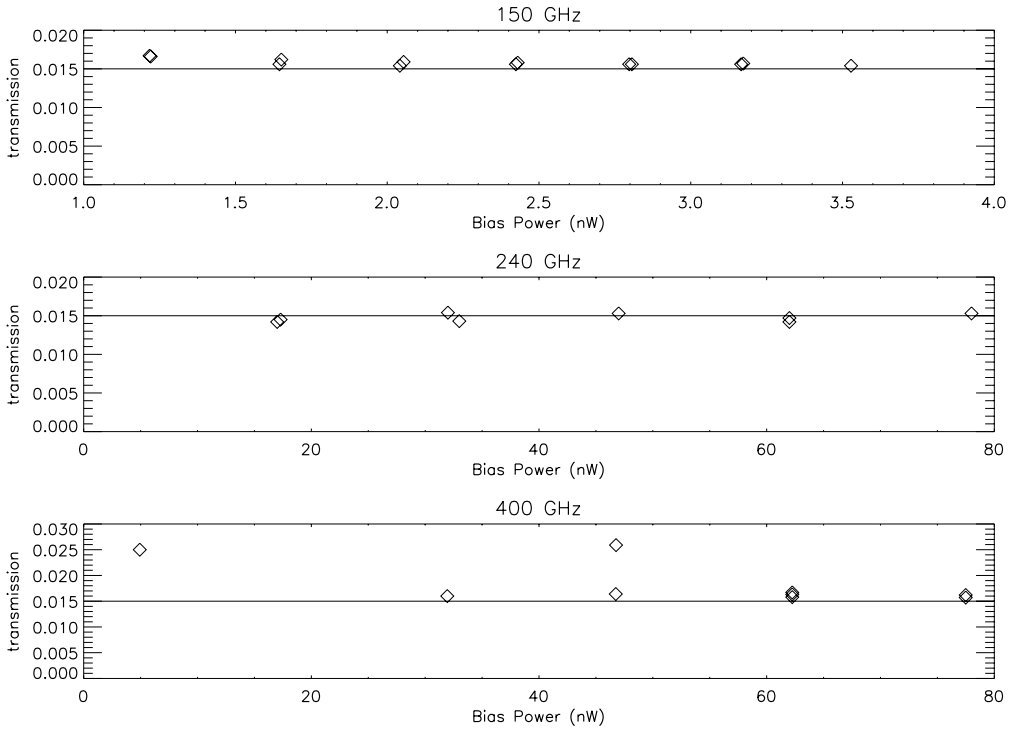

Figure 4.3:
Measured transmission of the neutral density filters as a function of bolometer bias power at the three frequencies 150, 240, and 400 GHz. The results converge to a transmission of 1.5% at large bias power, which is indicated in each panel by a solid horizontal line.

The transmission of the two NDF's that were measured in this manner was found to increase from their 300 K transmission when cooled to 2 K. The typical increase was about 10%, which is consistent with an increased conductivity of the metal film at low temperature.

4.8 Integrated Focal Plane

The focal plane consists of two each of the 90 GHz and 150 GHz single mode feeds and four multi-color photometers, for a total of 16 optical bolometers. Two dark bolometers and a 5 $M\Omega$ resistor were installed on the focal plane as diagnostic channels. One bolometer (Dark A) was in the same bolometer mount as the other detectors to provide a monitor of thermal fluctuations in the cold stage. The second (Dark B) is mounted directly on the focal plane. A grounded JFET was also read out to monitor problems with the JFET stage. As a monitor for problems with the bias generator and the warm electronics, the bias voltage for each readout box was also amplified (Bias 1-4) and read out by the DAS.

The detectors were read out by four electronics boxes. The AC bias generators in each electronics box were slaved to a master bias generator. With a slaved bias, signal crosstalk between boxes occurs at zero frequency. The first box read out the single mode channels (90A, 90B, 150A, and 150B) and the grounded JFET channel (GNDFET). The second box read out the multi-moded 150 GHz channels (150A1, 150A2, 150B1, and 150B2) and one dark channel (Dark A). The third box read out the 240 GHz channels (240A1, 240A2, 240B1, and 240B2) and the other dark channel (Dark B). The final electronics box read out the 400 GHz channels (400A1, 400A2, 400B1, 400B2) and the resistor (Load Res).

See Figure 3.3 for a schematic of where each beam appears on the sky.

4.9 Spectral Bandpass

The spectral bandpass of the instrument was measured before flight using a Fourier transform spectrometer (FTS). Interferograms are measured for each channel and Fourier transformed to measure the spectral response. The final spectra are corrected for the 250 μm thick polypropylene beam splitter and the spectrum of the 77K thermal source. A bandpass of one channel at each frequency is plotted in Figure 4.4.

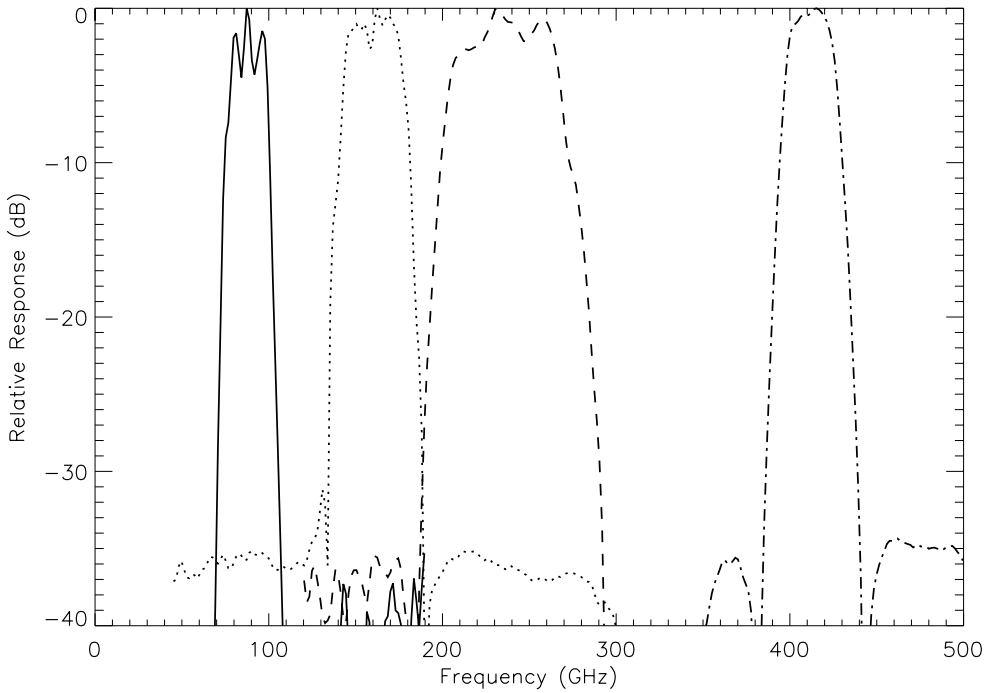

Figure 4.4:
Relative spectral response of the four BOOMERANG channels. The peak response in each band has been normalized to unity. The signal seen below -35dB is thought to be rectified noise.

4.10 Blue Leaks

Blocking each band with a high pass filter (thick grill filter) with a cut-off frequency just above the band allows a search for spectral leaks at high frequency. Since this test is sensitive to integrated leaks, a much higher signal to noise measurement can be made than with the FTS. The signals produced by a chopped LN_2 source viewed with and without a thick grill high pass filter in the beam were compared. Table 4.10 lists the results. The thick grill filter reduces the throughput of the beam, so a conservative factor of two was included to correct for this effect.

A high frequency leak in the bandpass can potentially make a channel more sensitive to galactic dust emission than to CMB anisotropy. Therefore, it is useful to determine the signal due to a source with a dust spectrum.

The quantity measured is the ratio of in-band to out-of-band power from a source with a chopped Rayleigh-Jeans spectrum:

$$R_{RJ} = \frac{\int (B_\nu^{300} - B_\nu^{77})\, t_{leak}(\nu) d\nu}{\int (B_\nu^{300} - B_\nu^{77})\, t_{band}(\nu) d\nu} \tag{4.8}$$

The desired quantity is the ratio of in-band to out-of-band power from a dust source:

$$R_{dust} = \frac{\int B_{dust} t_{leak}(\nu) d\nu}{\int B_{dust} t_{band}(\nu) d\nu} \tag{4.9}$$

Without detailed spectroscopy, assumptions must be made about the spectral characteristics of the leak and about the spectrum of dust. We assume that the spectral leak is flat in response from the cutoff of the highpass filter to the cutoff of the alkali-halide filter (1650 GHz). The amplitude of the leak is therefore:

$$T_{leak} = \frac{R_{RJ} \int_{band} (B_\nu^{300} - B_\nu^{77})\, t_{band}(\nu) d\nu}{\int_0^{1650\ GHz} (B_\nu^{300} - B_\nu^{77})\, t_{band}(\nu) d\nu} \tag{4.10}$$

For a dust spectrum, we choose a single-component model with a frequency-varying emissivity:

$$B_{dust} = \nu^\alpha B(\nu, T_{dust}) \tag{4.11}$$

We choose favored values of the emissivity spectral index and the dust temperature, $\alpha = 1.7$ and $T_{dust} = 20$ K [21]. The estimated in-band to out-of-band ratios are shown in Table 4.10. While the numbers appear high for the lowest frequency channels, they are no call for alarm. Roughly a quarter of the signal due to dust in the 90 GHz channels comes from the out-of-band leak rather than from the band. As shown later, the absolute response of the 90 GHz channels to dust is very weak.

4.11 Load Curves

Current versus voltage curves were measured for each of the detectors under "flight" loading conditions where a 300 K black load was viewed through the 1.5% neutral density filters.

The load curves were taken automatically; each detector was biased with a DC current which was ramped between 0 A and twice the current at which peak voltage was obtained. The load curves allow measurement of thermal conductivity and a measurement of electrical responsivity.

ν_0 (GHz)	Thick grill filter cutoff (GHz)	out-of-band power (R-J)	out-of-band power (dust)
90	150	1.7%	23%
150 sm	230	0.5%	3.1%
150 mm	230	0.9%	5.7%
240	300	0.8%	2.6%
400	540	0.5%	0.8%

Table 4.4:
The integrated power from above-band leaks in each channel for a source with a Rayleigh-Jeans spectrum and with a dust spectrum. The results shown are the average over channels at each frequency. Because of different filtering schemes, the 150 GHz channels are divided into single-mode (sm) and multi-mode (mm) here.

The thermistor material (NTD Germanium) gives a resistance as a function of temperature as follows:

$$R = R_0 \exp\left(\sqrt{\frac{\Delta}{T}}\right) \tag{4.12}$$

The parameters Δ and R_0 are set by the material properties and geometry of the thermistor. In this case $R_0 = 300\ \Omega$ and $\Delta = 30$ K.

Figures 4.5 through 4.8 show the load curves of all of the detectors measured on the ground. The thermal conductivity, G, is measured from the slope of temperature versus electrical power (Table 4.11). The electrical responsivity is the derivative of the voltage with respect to electrical power.

The bias at which peak responsivity occurs is the bias used in flight. To verify that this bias value provides peak responsivity, response to the calibration lamp was maximized as a function of bias.

4.12 Time Constant

The transfer function of a bolometer can be modeled as a low pass filter with transfer function $g = \frac{1}{1+i\omega\tau}$. The measured amplitude of the signal and the modulation frequency can be fit to the function $|g| = \frac{1}{\sqrt{1+\omega^2\tau^2}}$ where the time constant τ is a free parameter.

The target time constant for the BOOMERANG experiment was set by the observation strategy. To avoid 1/f noise in the bolometers, the beams are modulated on the sky as

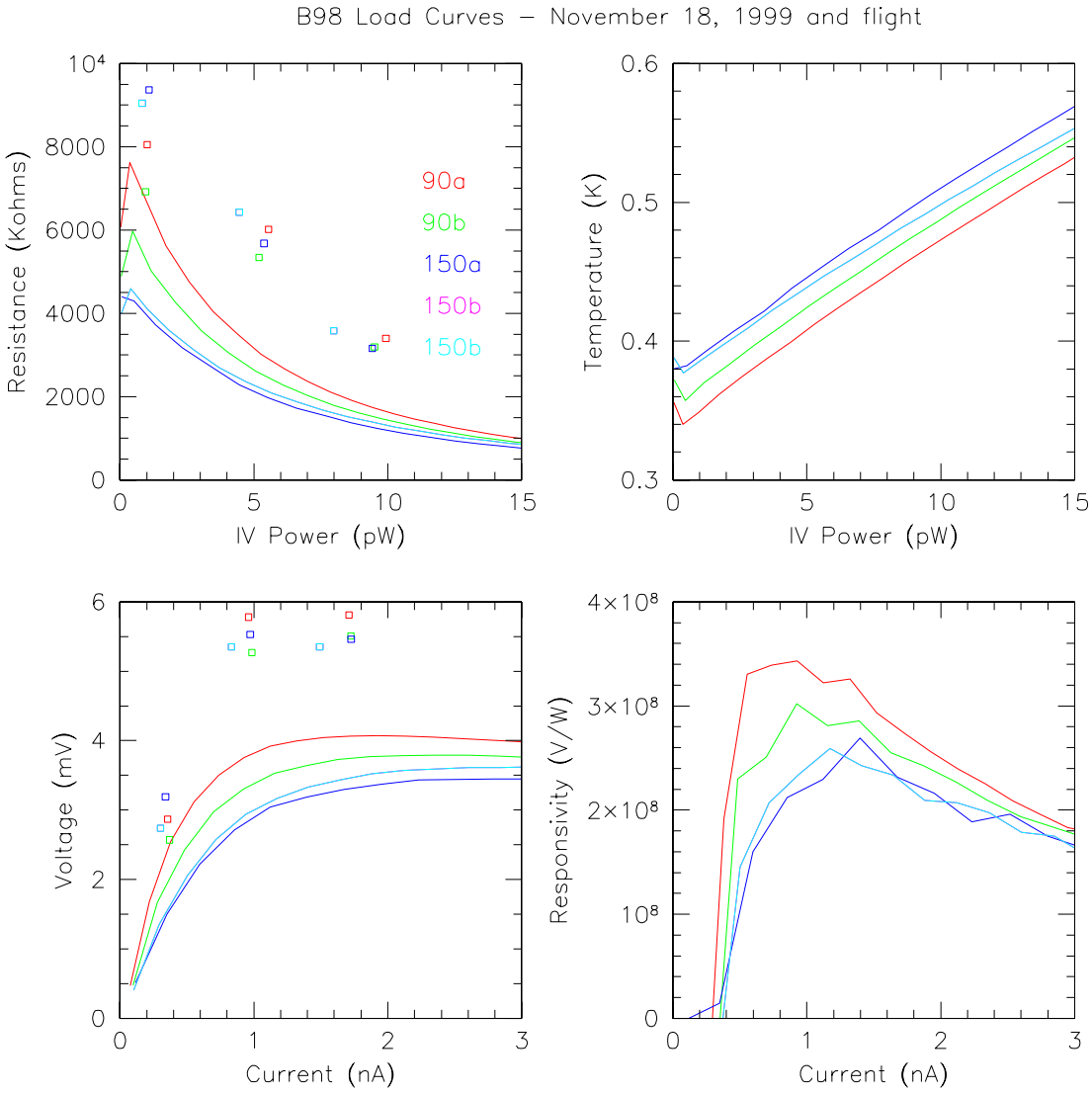

Figure 4.5:
Load curves of 90 GHz and 150 GHz detectors measured pre-launch. The lower left panel shows the raw voltage versus current. The upper left panel shows resistance plotted versus electrical power dissipated in the detector. The upper right panel shows temperature plotted versus bias power. The slope of this curve gives the thermal conductivity G (summarized in Table 4.11). The lower right panel shows electrical responsivity versus bias current.

rapidly as possible. The primary experimental goal of BOOMERANG is the measurement of the first acoustic peak which appears at an angular scale of $\sim 1^{\circ}$. This signal must appear in the bolometer time stream at a frequency well above the 1/f knee of the detector, but not at such high frequency that the bolometer time constant attenuates the signal. The time constant of the detector must allow a reasonable amount of bandwidth above the 1/f

Channel	target G (pW/K)	G (pW/K)
90A	60	81
90B	60	82
150A	60	81
150B	60	88
150A1	60	88
150A2	60	104
150B1	60	90
150B2	60	73
240A1	180	181
240A2	180	180
240B1	180	195
240B2	180	202
400A1	360	519
400A2	360	412
400B1	360	422
400B2	360	424
Dark A	360	377
Dark B	60	28

Table 4.5:
Thermal conductivity of each detector measured in the load curves, compared to the target conductivity.

knee (which appears at around 5 mHz). For a typical BOOMERANG scan speed of 1°/s, the first acoustic peak appears at ~ 0.4 Hz. The target bolometer time constants (see Figure 3.9) which are all less than 25 ms (corresponding to a cut-off at 6.3 Hz) allow a decade of bandwidth above the 1/f knee.

The time constant of the detectors in BOOMERANG were measured by measuring the response to a modulated thermal source. The modulation frequency was varied in discreet steps and a signal was recorded for each. The signal as a function of frequency was fit to the above transfer function. It was found that in order to get a good fit to the transfer function, it is necessary to have data at a frequency well below the time constant cut off.

The first column of Figure 6.8 shows the bolometer time constants measured with this method.

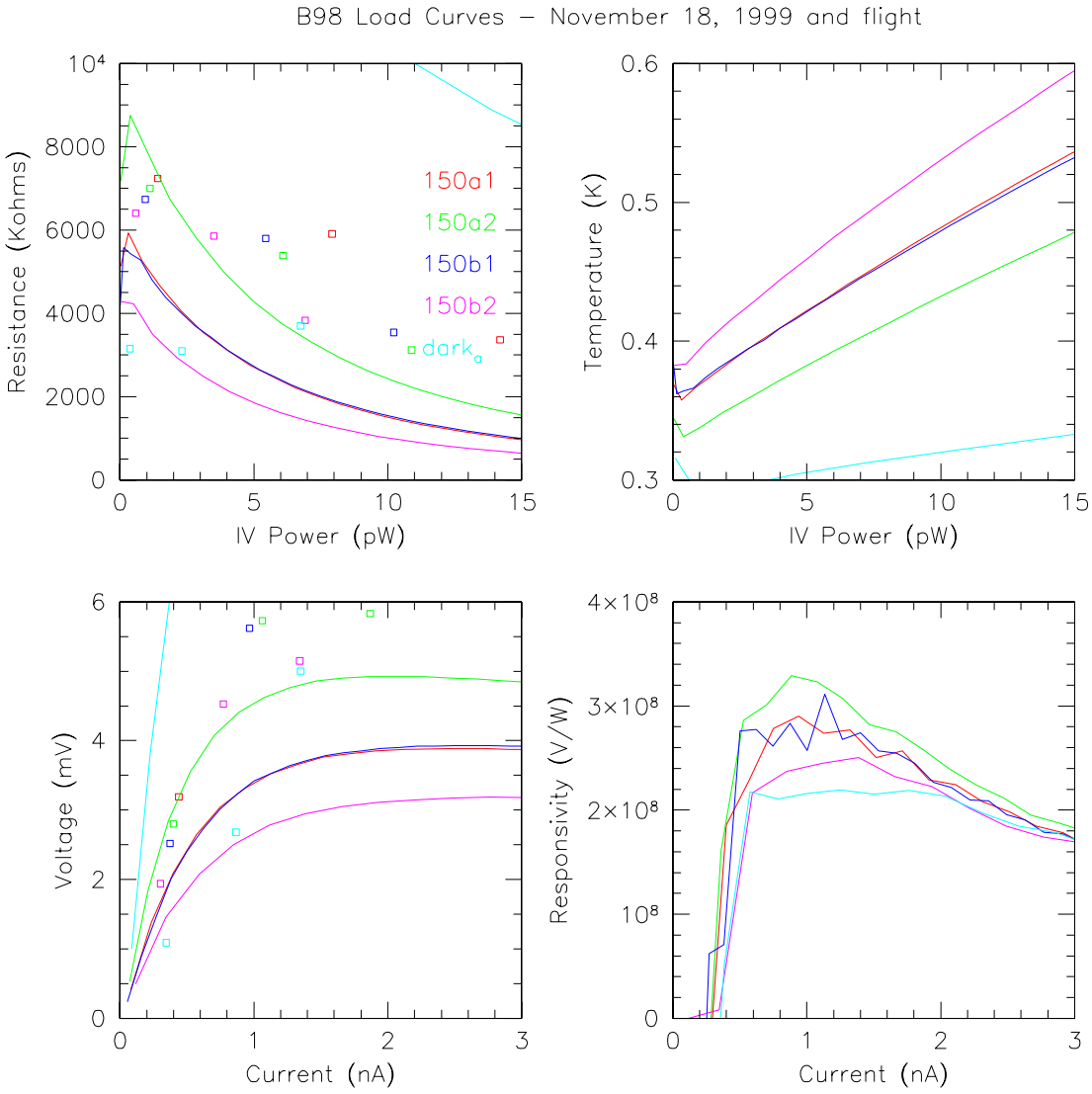

Figure 4.6:
Load curves of 150 GHz detectors measured on the ground. Channel Dark A is a 400 GHz detector and has a much higher thermal conductivity than the other bolometers in this figure.

4.13 Noise Performance

Before cooling the instrument, noise spectra were measured (Table 4.13). A section of time stream data was recorded using the DAS and Fourier transformed in software.

At room temperature, the impedance of the bolometers is ~ 1 kΩ, so bolometer noise is negligible compared to JFET noise. The bias monitor channels measure the noise of the bias generator plus the warm readout electronics. Each channel was found to be have a

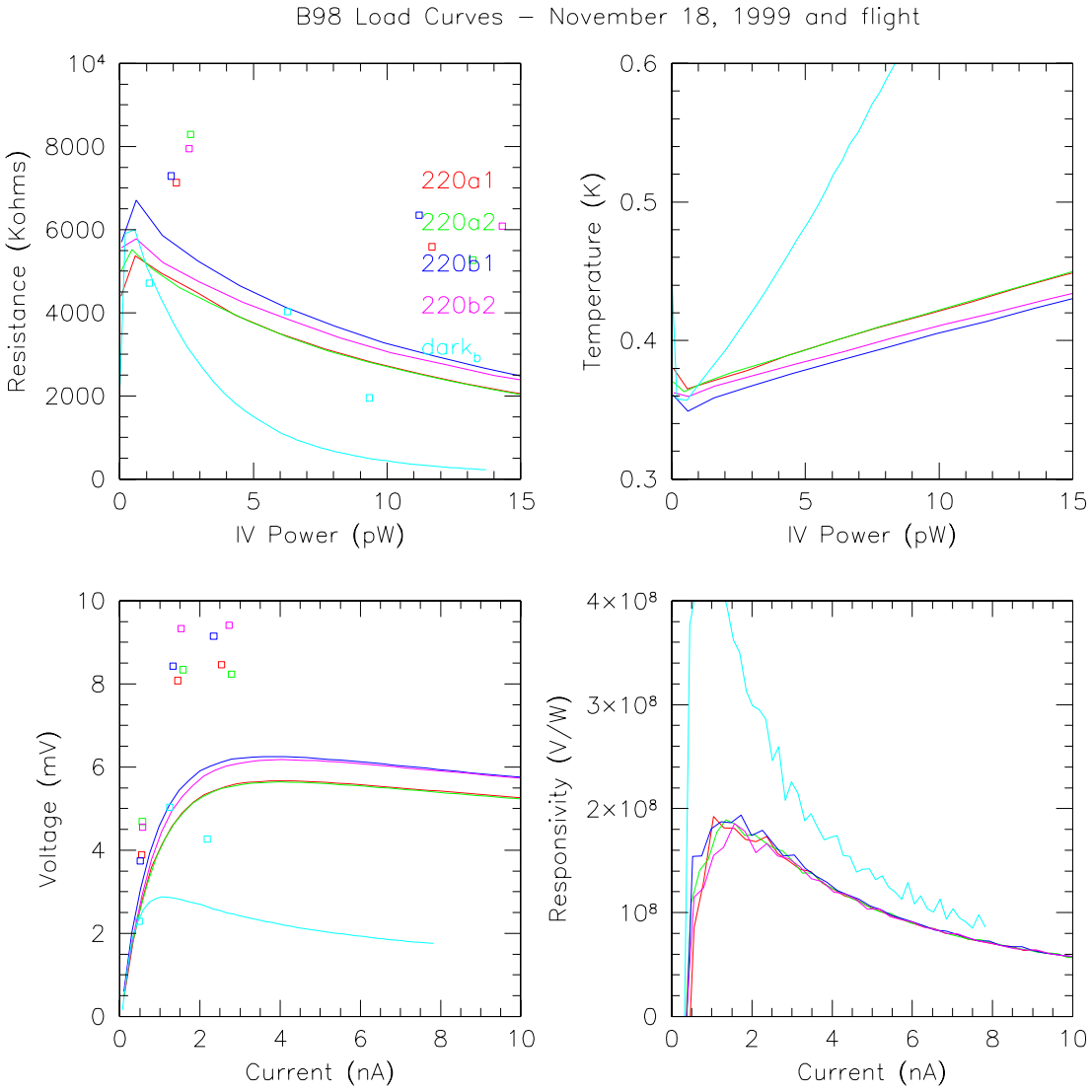

Figure 4.7:
Load curves of 240 GHz detectors measured on the ground.

white spectrum with JFET noise varying between 6 and 10 nV/$\sqrt{Hz}$. The noise of the bias monitor channels was 4-5nV/$\sqrt{Hz}$, so between 4-9nV/$\sqrt{Hz}$ of the noise in the detectors is due to JFET noise. The resistor channel was measured to have noise at the level of 30 nV/$\sqrt{Hz}$.

With the detectors at 0.280 K and viewing a 300 K source through the neutral density filters, noise spectra were taken again. Most channels have some excess noise at low frequency. Table 4.13 shows the measured white noise level and the frequency of the 1/f knee (defined to be the frequency at which the noise level is twice that of the white level).

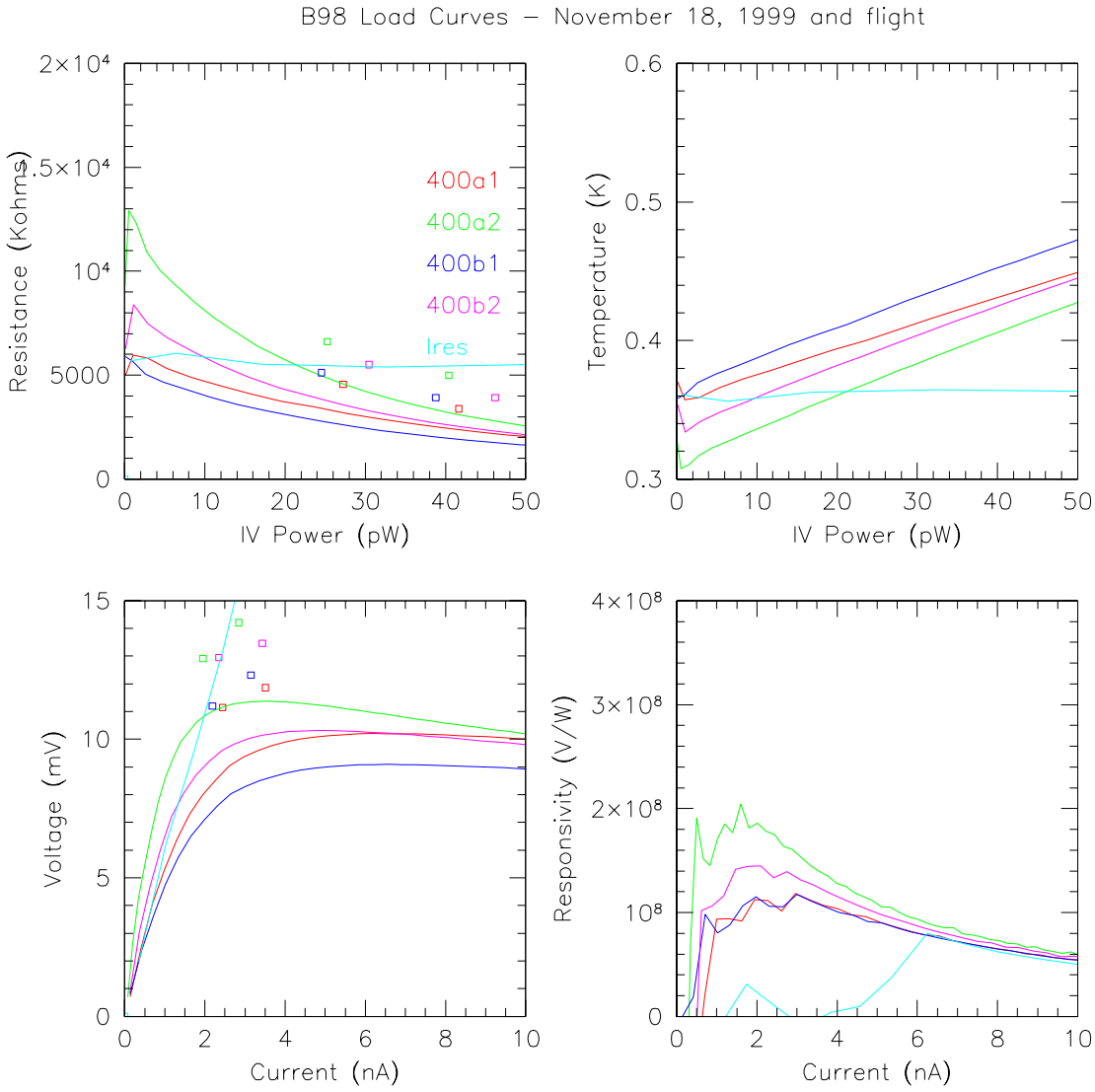

Figure 4.8:
Load curves of 400 GHz detectors measured on the ground.

Channels shown with upper limits in the 1/f knee column were not seen to have any excess noise at frequencies down to the lowest measured.

Several channels also had excess white noise: 240B2, 400A1, and Dark B. Swapping the JFETs, the bolometers, and the readout electronics of these channels with good channels had no effect on the noise performance. Therefore, the source of this excess noise is thought to be in the cold wiring. Due to time considerations, these channels were not repaired before flight.

Channel	warm noise $nV/\sqrt{Hz}$	cold white noise $nV/\sqrt{Hz}$	cold 1/f knee Hz
90A	8	12	0.01
90B	8	12	<0.01
150A	8	13	<0.01
150B	7	13	0.1
150A1	7	13	0.05
150A2	7	14	0.02
150B1	6	13	0.1
150B2	7	12	<0.01
240A1	6	15	0.03
240A2	6	15	0.03
240B1	9	15	0.03
240B2	7	50	0.1
400A1	6	30	0.1
400A2	6	17	0.05
400B1	10	18	0.1
400B2	10	20	0.1
Dark A	6	11	0.2
Dark B	6	35	0.1
Load Res	30	15	<0.01
GND FET	8	9	<0.01
Bias 1	4	4	0.05
Bias 2	4	4	0.05
Bias 3	5	4	0.05
Bias 4	5	4	0.1

Table 4.6:
Noise characteristics of each BOOMERANG channel measured in the lab, at room temperature and at 0.28 K. The white noise level is measured before and after cooling. The 1/f knee is the frequency at which the noise level reaches twice the white noise baseline level. In some channels, no 1/f spectrum was detected; an upper limit in frequency is listed for these channels. Tests show that the excess white noise seen in channels 240B2, 400A1, and Dark B is due to the cold wiring.

4.14 Beam Maps

Before launch, the beam shape was measured by mapping an eccosorb ball suspended by a tethered balloon. The ball consisted of foam eccosorb (EV Roberts LS-30) inside a sphere constructed of chicken wire. A small ball ($\sim 6''$ diameter) was used to map the main lobe and a large ball ($\sim 18''$ diameter) was used to measure the sidelobe response (see Figure 4.9). The ball was suspended by a tethered small weather balloon and anchored by a tripod

of kevlar cords (1 mm) diameter. The ball was approximately 500 m from the telescope during the mapping.

A shoulder in the beam was modeled using ZEMAX ray tracing code (Focus Software, Inc.). The result for one of the 150 GHz channels is shown in Figure 4.10. A shoulder is expected at the level of less than 1% of the main lobe. The model agrees well with the tethered balloon data to about -25dB (see Figure 4.9).

The width of the main lobe measured by cuts in azimuth across the small tethered source are listed in Table 4.14.

Channel	FWHM (arcminutes)
90A	19.5
90B	18.45
150A	9.42
150B	9.68
150A1	10.11
150A2	10.62
150B1	10.46
150B2	10.32

Table 4.7:
The FWHM of each of the 90 GHz and 150 GHz channels as measured by cuts in azimuth across the tethered source.

4.15 Lab Calibration

The absolute calibration of the BOOMERANG receiver was determined by measurement of the bolometers' response to a chopped thermal load. The chopped source consisted of an inverted plastic cone in a bucket of ice water (at 0° C) and a piece of room temperature (15° C) eccosorb. Both sources were large enough to fill the entire beam. The detectors viewed the source through the neutral density filters to reduce the background and the chopped signal.

The calibration on the ground was limited by knowledge of the transmission of the Neutral Density Filter, limiting the measurement to a precision of $\sim 20\%$. The lab calibration is discussed further in Chapter 7 in reference to calibrating the instrument in flight. Table 7.7 includes a summary of the lab calibration scaled to flight conditions via the background

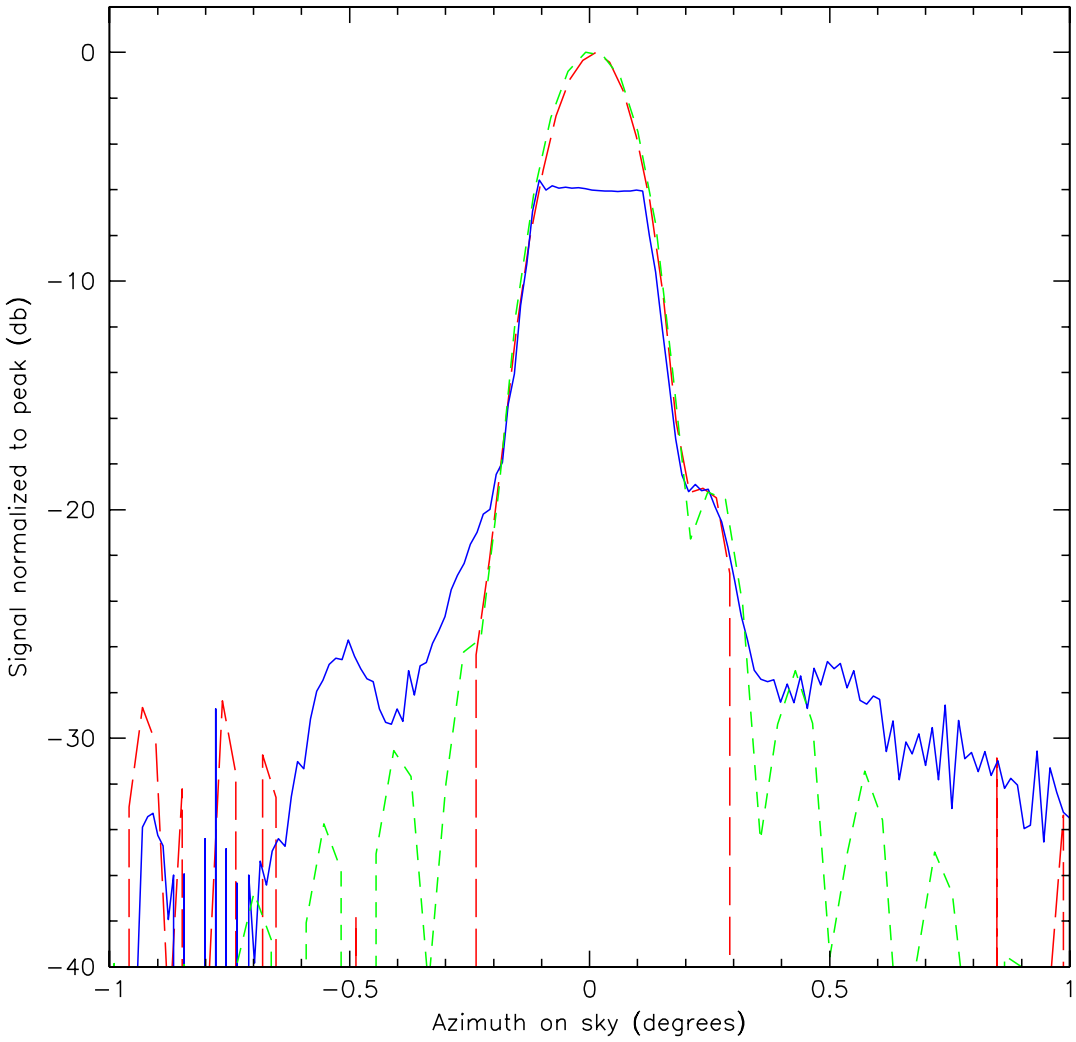

Figure 4.9:
150 GHz bolometer data from one scan in azimuth across the tethered sources. The solid blue line shows the signal from the large source, and is saturated at the center of the beam. The red dashed line shows the signal from the small source. The green dotted line shows the ray traced model. The data shown here is from one of the single-mode 150 GHz channels (150B).

loading.

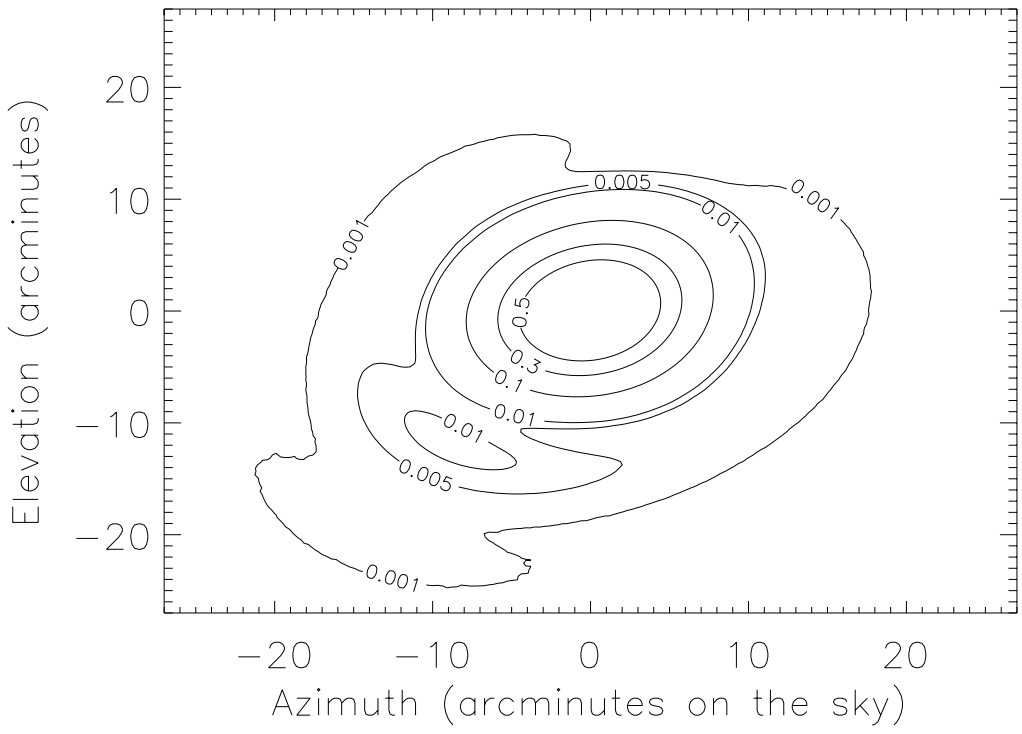

Figure 4.10:
Ray trace model for one of the 150 GHz beams (channel 150A).

Chapter 5 1997 Test Flight

To qualify for the Antarctic flight, a test flight was made from Palestine, Texas, in the summer of 1997. BOOMERANG/NA was less sensitive, had coarser angular resolution and fewer channels, and observed a much smaller region of the sky than planned for the Antarctic flight. Nonetheless, a map and a measurement of the power spectrum was made which had scientific merit of its own. A more detailed discussion of the results of the test flight can be found in [44] and [47].

5.1 Test Receiver

The receiver flown in the test flight was a test version of the instrument described in this thesis and is described in detail in [57]. There were 6 optical bolometer channels; 2 at 90 GHz and 4 at 150 GHz. The result described below is derived entirely from data from one of the 150 GHz channels and is checked with data from one of the 90 GHz channels. The system was multi-moded in an attempt to achieve greater sensitivity to CMB fluctuations at the expense of angular resolution. The parameters of the receiver are shown in Table 5.1.

ν_0 (GHz)	$\Delta\nu$ (GHz)	FWHM (arcmin)	τ (ms)	NET$_{CMB}$ (μK/$\sqrt{Hz}$)
96	33	26	71 $\pm$ 8	400
153	42	16.5	83$\pm$ 12	250

Table 5.1:
Parameters of the 1997 BOOMERANG test receiver.

5.2 Observations

The instrument was launched on August 30, 1997, and spent 6 hours at an average float altitude of 38.5 km. 4.5 hours were spent observing the CMB in 40 degree peak-to-peak azimuth scans centered on the South at an elevation angle of 45 degrees. The scans were

smoothed triangle waves with a peak scan speed of 2.1 azimuth degrees per second. As the Earth rotated, the scans mapped out a wide strip of sky from -73 $< \alpha <$ 23 and -20 $< \delta <$ -16. Figure 5.1 shows a map made from the data. The signal to noise per pixel in the map is approximately 1, so no structures are readily visible.

Observations of Jupiter, which was mapped twice during the flight, provided a measurement of the solid angle of the beam and a responsivity calibration. The precision of the calibration at 150 GHz and 90 GHz is 8.1% and 8.5%.

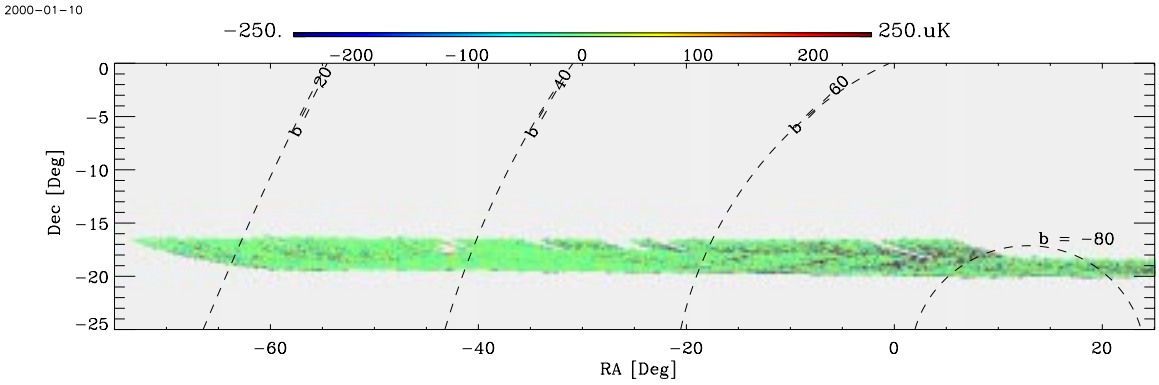

Figure 5.1:
The map produced by the BOOMERANG/NA experiment. The signal to noise ratio per pixel in the map is too low to see any structures by eye; the detection of anisotropy is statistical.

5.3 Power Spectrum Estimation

To produce a map and a power spectrum, the calibrated data are processed using the MADCAP software package [10] on the Cray T3E-900 at NERSC and the Cray T3E-1200 at CINECA. MADCAP produces a maximum likelihood map and pixel-pixel correlation matrix of 23,561, 1/3 beam sized (6′) pixels from the time-ordered 150 GHz data, the noise correlation function, and the telescope pointing information. The maximum likelihood power spectrum is estimated from the map in eight bins between 25 $< \ell <$ 1125. and is shown in Figure 5.2.

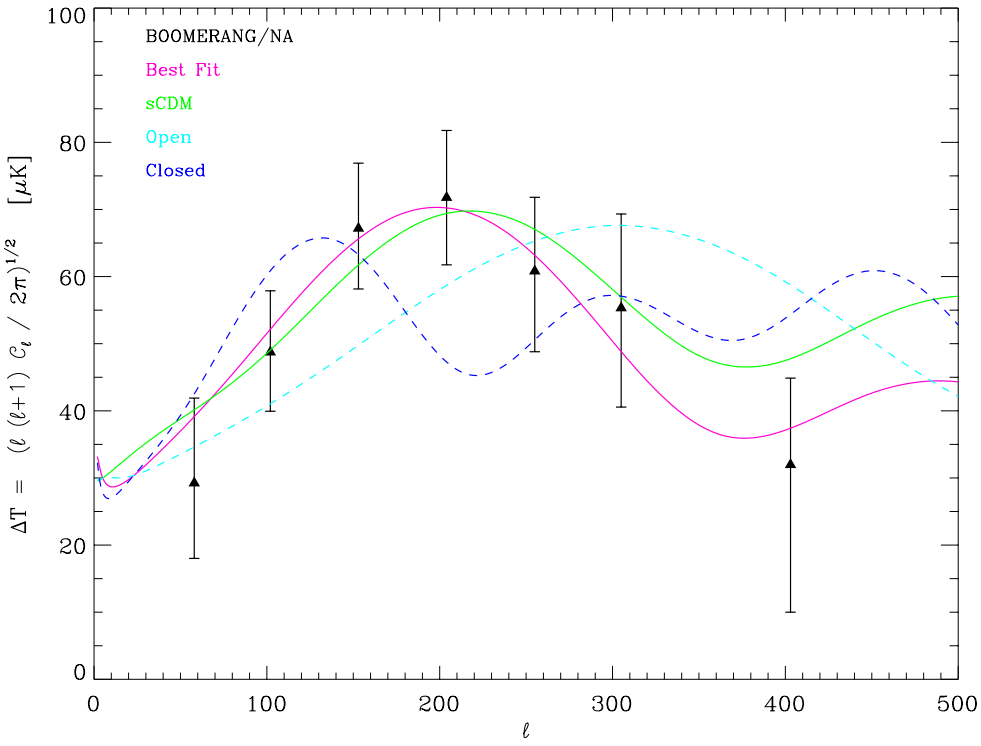

Figure 5.2:
The angular power spectrum of the CMB as measured by BOOMERANG/NA. Superposed is the best-fit model of [47], a standard cold dark matter spectrum, and open and closed models.

5.4 Systematics Tests

The scan strategy and the analysis allow a variety of tests for systematic effects to be performed on the data. First, we analyze coarsely pixelized maps made from combinations of data which we expect to produce a null result: 1) the difference between left-going and right-going scans which are adjacent in time, and 2) the dark bolometer. The amplitude of a flat power spectrum for $25 < \ell < 475$ for the left-right difference is $\ell(\ell+1)C_\ell/2\pi =$ -400±200 μK^2 and -100±100 μK^2 for the dark channel. The negative power in the left-right difference is due to the effects of noise which is correlated from scan to scan and both results are consistent with zero.

To check that our measured power is indeed CMB anisotropy, we compare the 150 GHz power spectrum to that of the 90 GHz channel. Flat band powers for a single bin ($25 < \ell <$ 475) of $\ell(\ell+1)C_\ell/2\pi =$ 3100±500 μK^2 and 2500±700 μK^2 are found for 150 GHz and

90 GHz respectively.

The mapped region lies over a wide range of galactic latitude, from b=-15 to b=-80. To test for the presence of galactic foregrounds in the map, the data is divided into two halves: low galactic latitude (-15 < b < -45) and high galactic latitude (-45 < b < -80). These two halves are analyzed separately, and a consistent flat band power from $25 < \ell < 475$ of $\ell(\ell+1)C_\ell/2\pi = 3580 \pm 700\ \mu K^2$ and $2980 \pm 700\ \mu K^2$ are found for the low galactic latitude and high galactic latitude halves, respectively.

5.5 Measuring Curvature

The BOOMERANG/NA data cover a range of ℓ space corresponding to the horizon size at last scattering. The angular scale of a peak at degree angular scales in the angular power spectrum at $\ell = 200$ is primarily sensitive to the angle/distance relationship to last scattering and can be used to constrain the total energy density of the universe, $\Omega = \Omega_M + \Omega_\Lambda$.

We perform a maximum likelihood search in cosmological parameter space following the methods of [9] (explained in further detail in Section 8.3 of this thesis). We restrict our search to the family of adiabatic inflationary cosmological models and vary only the parameters Ω_{CDM},Ω_Λ,Ω_B,h,n_s, and C_{10}. We search a grid in the plane ($\Omega_M = \Omega_{CDM} + \Omega_B$, Ω_Λ) over the range [0.05,2] and [0,1]. As in [20], at each point on the grid, we maximize the likelihood with respect to the four remaining parameters. Using constraints from other cosmological measurements, we restrict the parameters to lie within $0.8 \leq n_S \leq 1.3$, $0.5 \leq h \leq 0.8$, $0.9 \leq C_{10}/C_{10}^{COBE} \leq 1.1$, and $0.013 \leq \Omega_B h^2 \leq 0.025$.

Using BOOMERANG/NA data alone, we obtain the results in Figure 5.3.

5.6 Discussion

Within the class of models considered, we strongly constrain $\Omega = \Omega_M + \Omega_\Lambda \sim 1$ using BOOMERANG/NA data alone. The constraints can be improved further by including data from other experiments. Figure 5.6 shows the results of the analysis including the result of COBE and SN1A measurements [56]. We find 1σ constraints $0.2 \leq \Omega_M \leq 0.45$ and $0.6 \leq \Omega_\Lambda \leq 0.85$. These results are further refined in later chapters with the data from the

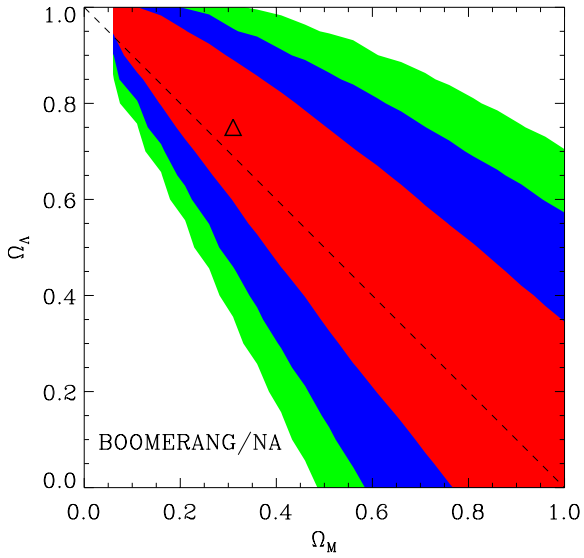

Figure 5.3:
Likelihood contours for the Boomerang/NA power spectrum alone. Colors represent contours corresponding to 0.32, 0.05, and 0.01 of the peak likelihood. The triangle represents the maximum likelihood model. 68% of the integrated likelihood corresponds to $0.85 \leq \Omega \leq 1.25$.

Antarctic flight of Boomerang.

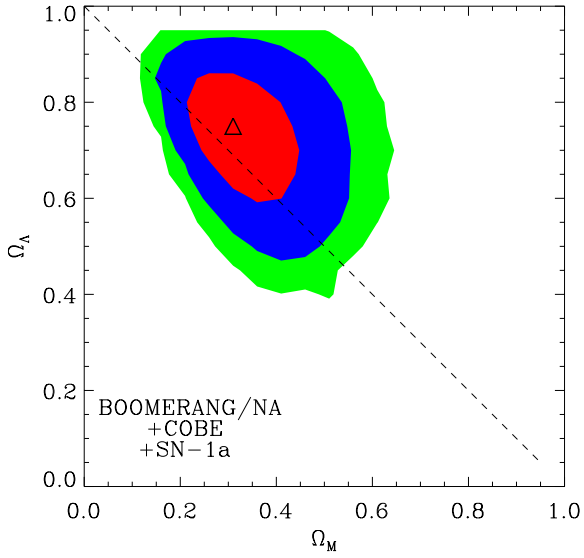

Figure 5.4:
Likelihood contours including COBE and high redshift supernovae data from [56].

Chapter 6 1998 Flight Performance

BOOMERANG was launched from Williams Field at McMurdo Station (Antarctica) on December 29, 1998, at 3:30 GMT. The instrument reached float altitude (∼38km) three hours later and began observations immediately. The telescope remained within 1.5° of ∼ 78° S latitude as it circumnavigated the continent (Figure 6.1). The flight lasted 259 hours and was terminated 50 km south of the launch site at 78°35′ S 168°22′ E.

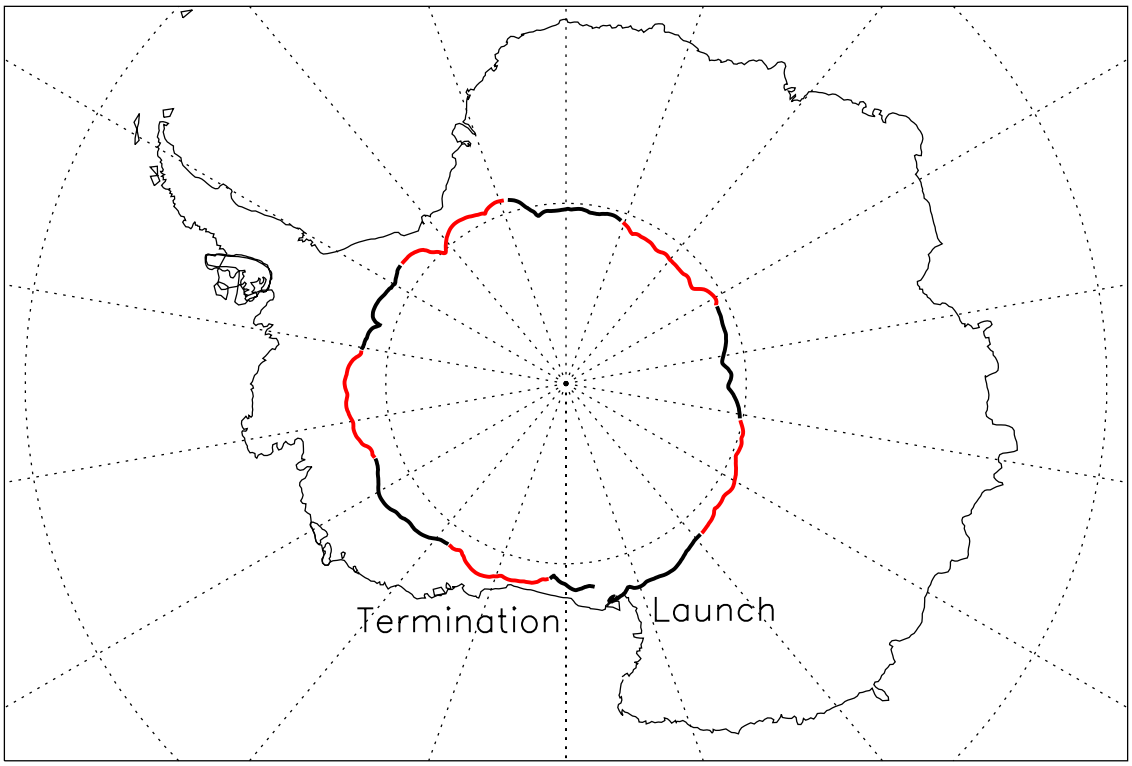

Figure 6.1:
The path of the LDB flight of BOOMERANG. The alternating colors indicate days from launch.

The majority of the flight was spent in CMB mode, which consisted of scanning the telescope in a smoothed triangle wave with a 60° peak- to-peak amplitude in azimuth at fixed elevation. The center of the scan was set so that the region of sky away from the galactic plane was mapped within the constraint of solar avoidance. As the Earth rotated,

the scan center and scan direction on the celestial sphere changed. At a single elevation, one day of scanning provided a coverage of 22° in declination and gave scans tipped at ±11°, providing cross-linking of the scans.

Two scan speeds were used in CMB mode; 1°/s and 2°/s. The elevation of the telescope was changed roughly daily between angles of 40°, 45°, and 50°. Every 90 minutes, a 120° peak-to-peak scan centered on the anti-Sun direction was conducted for 5 minutes as a check for systematic effects due to the Sun. Several HII regions in the galactic plane were targeted during the flight as potential cross-calibrators and beam mapping sources. These were RCW38, RCW57 (a double source composed of NGC3603 and NGC3576), IRAS/08576, IRAS/1022, and the Carina Nebula. Three known clusters (A3158, A3112, A3226) were targeted in a search for the Sunyaev-Zel'dovich effect. Three extragalactic point sources were observed serendipitously in the CMB map: the blazar 0537–441 (8544), the BL Lac quasar 0521–365 (8036), and the QSO 0438–443 (7044). The total time spent in each scan mode is shown in Table 6.

Target	time(hours)
1°/s CMB	105.8
2°/s CMB	82.0
WIDESCAN	10.7
A3158	9.9
IRAS/08576	9.2
Diagnostics	8.9
RCW38	7.4
A3226	6.4
A3112	3.3
η Car	3.3
IRAS/1022	2.7
Cen A	2.2
RCW57	1.4

Table 6.1:
The time in hours spent in each mode during the BOOMERANG flight.

6.1 Electronics

The high cosmic ray flux above the Antarctic was a concern for digital electronics; however, most digital electronics performed well. The Data Acquisition System performed flawlessly

with no interruptions. In addition, the Attitude Control System (with 386 CPU's) had no in-flight lockups. The two data storage computers (with 486 CPU's) had two lockups each during the 10.5 day flight, but were successfully rebooted by the watchdog system. The redundancy of the two data-logging computers provided a continuous final data stream.

6.2 In-flight Calibration of the Sun Sensor

The azimuth Sun sensor was initially calibrated on the ground using a bright lamp. The measured Sun azimuth depends on the Sun elevation, so a two-dimensional map was made. However, a difference in flight and ground calibrations was found.

In-flight wide scans of the telescope were used to cross-calibrate the azimuth Sun sensor as a function of Sun elevation with the integrated gyroscope signal. Thirty-two wide scans were done throughout the entire flight and covered a range between 11 and 32 degrees solar elevation. The gyroscope signals are stable to an accuracy which is less than an arcminute over the time period of several minutes. Therefore, the short period of this scan allows the gyroscope signal to be a good absolute calibrator over this interval. Lookup tables were created for each of the Sun elevations and a linear interpolation is used to determine the Sun sensor azimuth for Sun elevations which are in between those covered by the 32 galaxy scans.

See Figure 6.2 for a plot of all of the lookup tables as a function of Sun elevation. While the general shape of the correction is similar at all Sun elevations, the amplitude of the correction near an azimuth of zero varies by more than a degree between the two extremes of Sun elevation.

6.3 Attitude Reconstruction

The Sun sensor provides a repeatable and precise measure of gondola elevation and azimuth relative to the Sun. The Sun sensor signal is difficult to calibrate, however, due to its dependence on both Sun elevation and Sun azimuth. Therefore, the gyroscopes are used as the primary pointing sensor in the final reconstruction.

The azimuth, pitch, and roll of the telescope are reconstructed by integrating the signal from the rate gyroscopes. The three signals are orthogonalized by rotating until the corre-

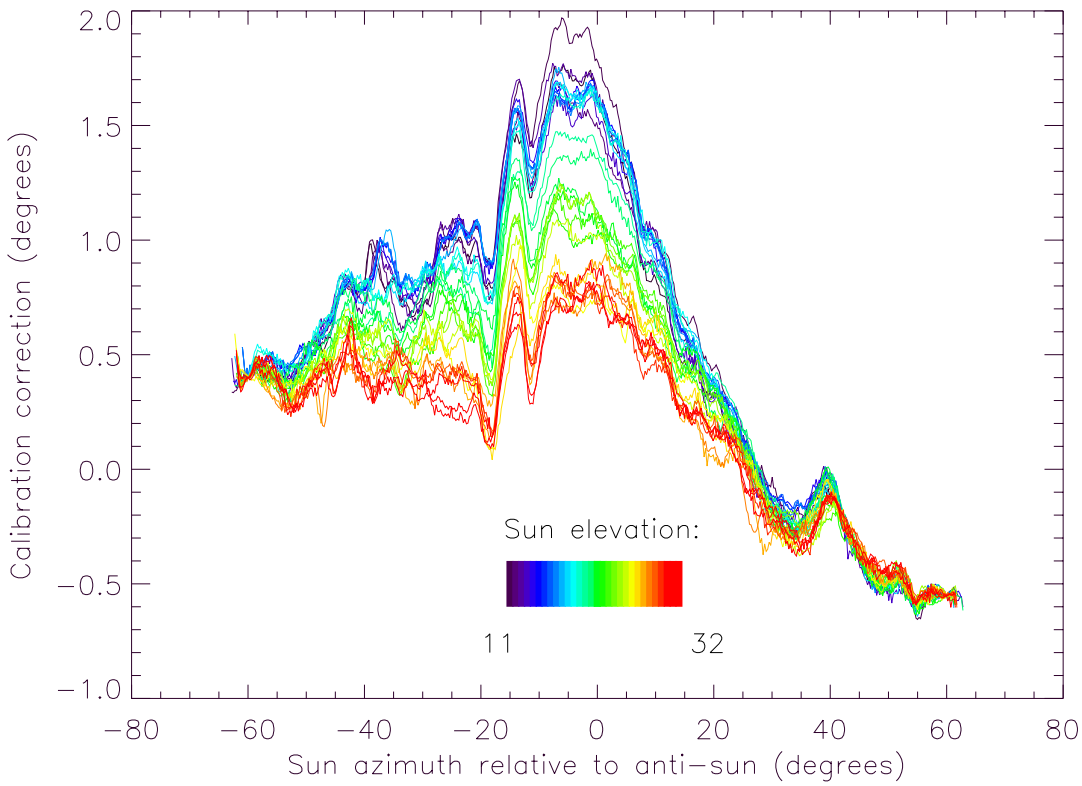

Figure 6.2:
Correction to the calibration of the Sun sensor as determined by the gyroscope lookup tables. The dependence on Sun elevation and the error on order of a degree in the ground calibration are evident.

lated signal is minimized. The integrated azimuth rate gyroscope signal is then fit to the Sun sensor data to determine the offset of the gyroscope. The azimuth is corrected for roll with the integrated roll gyroscope signal (Appendix C). Telescope elevation is determined by integrating the pitch gyroscope and adding the integrated signal to the elevation encoder.

The offset of each beam from the telescope boresight is determined from observations of the HII regions. See Appendix B for the method of determining the beam offset. Table 6.3 lists the average offset parameters measured on the 17 sources. Repeatability of the measured position of sources shows that the pointing has been reconstructed to an accuracy of $3'$ rms (see Figure 6.3 and Table 6.3). This is more than a factor of 2 improvement over using the original calibration of the Sun sensor. The reconstructed beam elevation and azimuth are combined with latitude, longitude, and time measured with GPS receivers to determine the right ascension and declination of each beam at each sample.

Channel	Elevation offset (α) (degrees)	Azimuth offset (β) (degrees)
90A	0.101	-1.633
90B	0.106	2.263
150A	0.646	-1.395
150B	0.681	2.024
150A1	0.080	-0.948
150A2	0.574	-0.736
150B1	0.083	1.617
150B2	0.595	1.424

Table 6.2:
The average offset parameters for each channel.

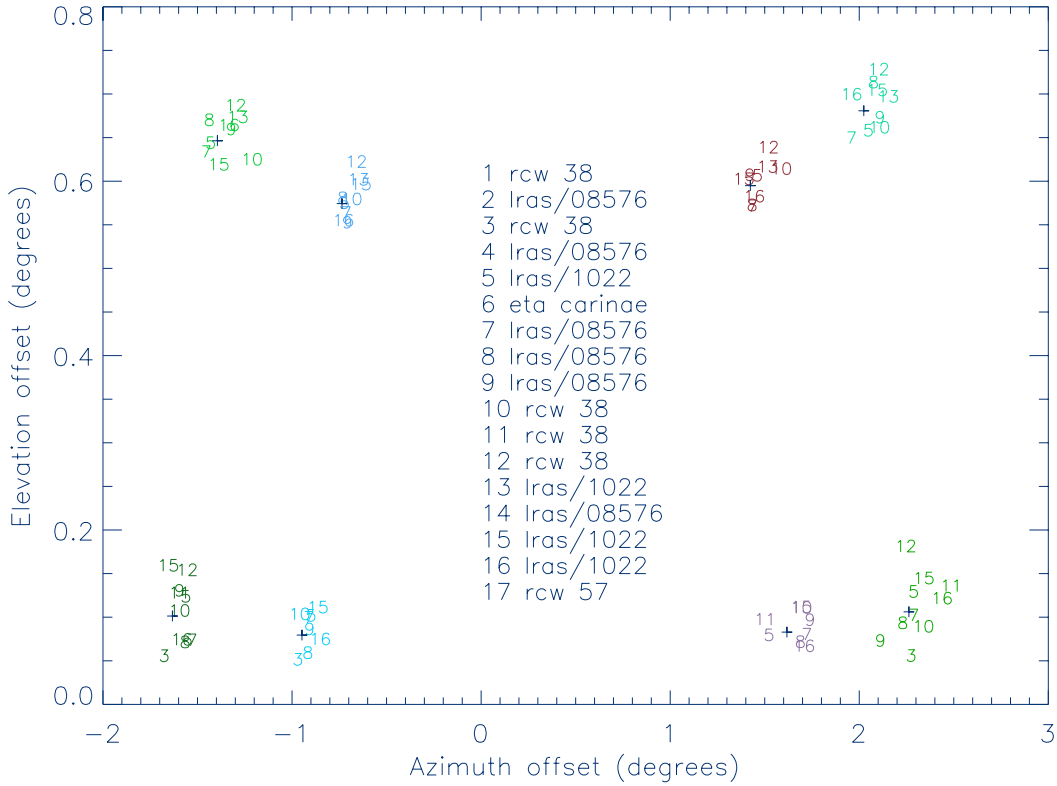

Figure 6.3:
The scatter in beam offsets as measured from observations of sources. Each source observation is denoted by a number. The average offset for each channel is denoted by a small cross.

6.4 Thermal Performance

See Table 6.4 for a comparison of predicted temperatures with actual achieved temperatures.

In order to increase the temperature of some of the electronics, white nylon blankets were

Channel	rms in α	rms in β
90A	$2.10'$	$2.82'$
90B	$2.12'$	$5.47'$
150A	$1.33'$	$4.04'$
150B	$1.55'$	$3.69'$
150A1	$1.24'$	$2.14'$
150A2	$1.30'$	$1.59'$
150B1	$0.967'$	$5.35'$
150B2	$1.25'$	$3.18'$
total	$1.48'$	$3.53'$

Table 6.3:
The r.m.s. scatter in the offset parameters for each channel. This measures the pointing jitter of the experiment to be on the order of a few arc minutes.

placed over the electronics boxes. This had the effect of producing in-flight temperatures which were roughly 20°C warmer than predicted. All temperatures were in an acceptable range.

Component	Predicted temperature °C	Measured temperature °C
Attitude Control System	-8° to 12°	15° to 30°
Data Storage System	17° to 27°	33° to 42°
Data Acquisition System	-7° to 6°	18° to 29°
Cryostat	-29° to 27°	-5° to 13°
Bolometer Readout Electronics	-31° to 2°	21° to 27°
Solar Array	55° to 92°	57° to 68°
Ground Shield	no prediction	-37° to -17°
Primary Mirror	no prediction	-12° to 1°
Gondola Frame	no prediction	15° to 28°

Table 6.4:
A comparison of the payload thermal model with the temperature achieved in flight. The two predicted values are for the "cold" and "hot" cases. The two measured values are the minimum and maximum temperatures reached during the daily cycle.

6.5 Cryogenics

The cryogenic system performed well, keeping the detectors well below their required operating temperature of 0.3 K for the entire flight. A plot of the important temperatures

recorded during the 10.5 days flight is shown in Figure 6.4. The small daily oscillation of the main helium bath temperature is due to daily fluctuations of the external pressure. The external pressure variation correlates well with the altitude of the payload. The altitude of the payload varies with the elevation of the sun, which oscillates between 11° to 35° diurnally. We have searched for scan synchronous temperature fluctuations in the ^{3}He evaporator and in the ^{4}He temperature, and we find upper limits of the order of 1 μK_{rms}, and drifts with an amplitude of a few μK during the 2°/s scans. No active temperature control was used.

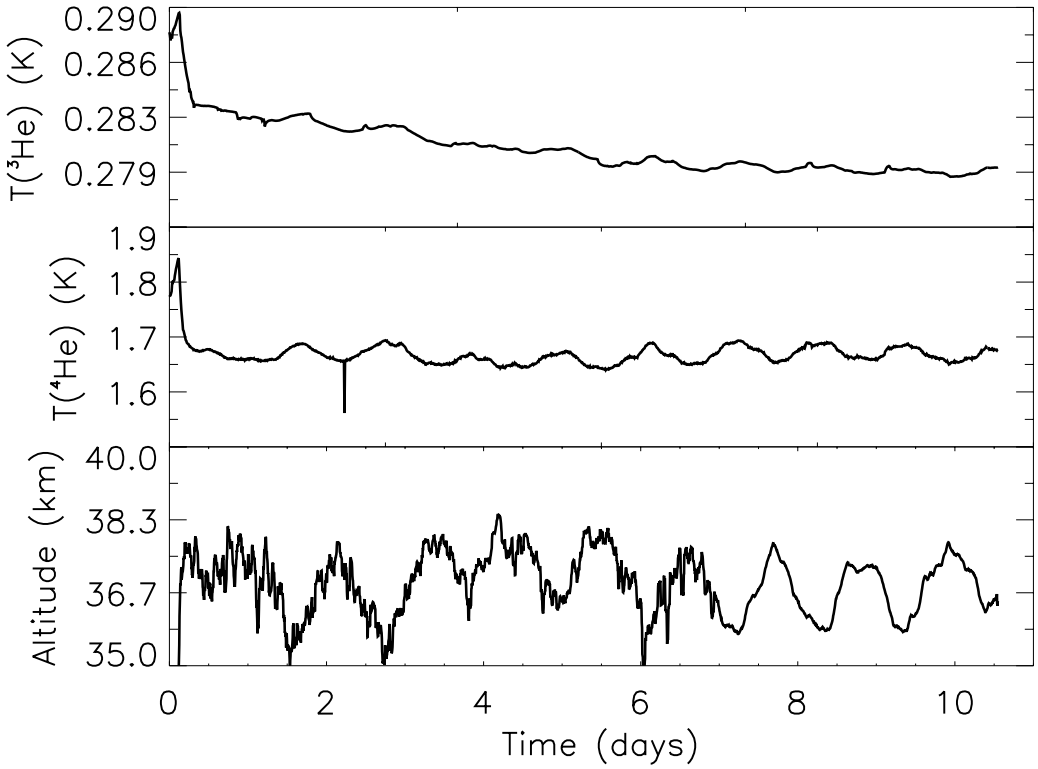

Figure 6.4:
The temperature of the ^{4}He cold stage and of the ^{3}He evaporator during the flight. The lower panel shows the altitude of the payload (measured using the onboard GPS) which anticorrelates well with both cryogenic temperatures.

6.6 Beam Map

To measure the beams in flight, observations were made of Galactic HII regions and of the extragalactic point sources. The HII regions are bright, but are not point-like and do not

lie in the same region of the sky as our main CMB map and are therefore not subject to the same pointing jitter. The extragalactic sources are point-like and reside in the CMB region, but are quite dim. As a compromise, we estimate the beam size with three different methods.

The primary in-flight method for estimating the beam is through the measurement of radial flux profiles of the sources. The timestream data are binned in annuli around the center of the source. The timestream data are high-pass filtered at 0.2 Hz and 0.05 Hz for the extragalactic and galactic sources, respectively. The right ascension (α), declination (δ) and bolometer signal for unflagged data within approximately 1-2° of the source are extracted from the timestream. The average signal in each annulus is computed, yielding a radial flux profile of the source. A Gaussian plus a second order polynomial baseline are fit to the radial profiles. This process is repeated on an (α, δ) grid around the nominal center coordinates in case the source is not located exactly at the nominal coordinates due to pointing offsets. The centroid of the source is found by choosing the center coordinates which result in the minimum variance for the fit Gaussian FWHM. An example radial profile fit is shown in final centroid coordinates in Figure 6.5.

While most observations of the Galactic sources in BOOMERANG were specifically targeted, there were a few (1-3) scans across sources in each channel that were serendipitously made during CMB observations. As a second method of in-flight beam estimation, we fit a Gaussian to each of these scans. A Monte Carlo model of the pointing uncertainty indicates that there is $4.5'$ FWHM jitter in the current pointing solution. It is best to use the scans which were taken in CMB observation mode, rather than scans taken in source observation mode to estimate the pointing jitter expected in the main CMB region.

The third in-flight method for estimating the beam is by making one-dimensional Gaussian fits to RCW38 single scan cuts. The estimated FWHM, with amplitude normalized to 1.0, and center are passed as initial guesses to a nonlinear fitting routine, with free parameters for an offset and linear, quadratic, and quartic baseline. The FWHM in samples are converted to FWHM in arcminutes on the sky.

Figure 6.6 summarizes the FWHM derived from the above three methods. We conclude that the beams have an effective FWHM (including pointing jitter) of $18' \pm 2'$ for the 90 GHz single-mode channels, $10' \pm 1'$ for the single-mode 150 GHz single-mode channels, $10.5' \pm 1'$ for the 150 GHz multi-color photometer channels, $14' \pm 1'$ for the 240 GHz

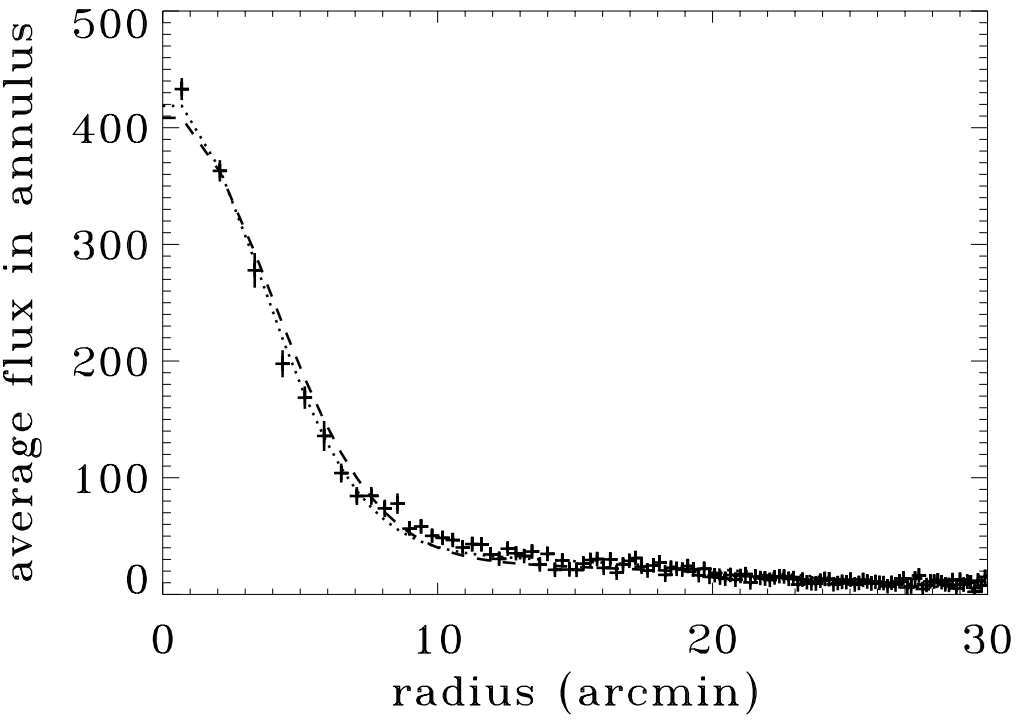

Figure 6.5:
Radial profile of RCW38 as seen by channel 150A. The crosses indicate the signal in each annulus. The dotted and dashed lines show two methods to fit a Gaussian plus second order polynomial baseline. The dashed line shows a fit using a gradient-expansion algorithm and the dotted line shows the fit using a non-linear least-squares fit. The two methods agree well.

channels and $13' \pm 1'$ for the 400 GHz channels, where the uncertainty is systematic and is determined by uncertainty in the pointing due to jitter.

The beam sizes derived from in-flight observations are generally larger than those obtained before launch with the tethered source (see Table 4.14) because in-flight pointing jitter degrades the resolution of the experiment. This can be improved in the future with a further calibration of the Sun sensor.

The beam for each of the 90, 150 and 400 GHz channels is well-described by a Gaussian. The 240 GHz beams can be modeled by 2 superimposed Gaussians. Figure 6.7 shows the radial flux profile and corresponding 2-lobe fit for one source and channel.

In order to place limits on a shoulder in the beam, the amplitude of which could vary with angle, radial flux profiles were calculated in 4 semi-annuli (halves) and 8 quadrant-annuli

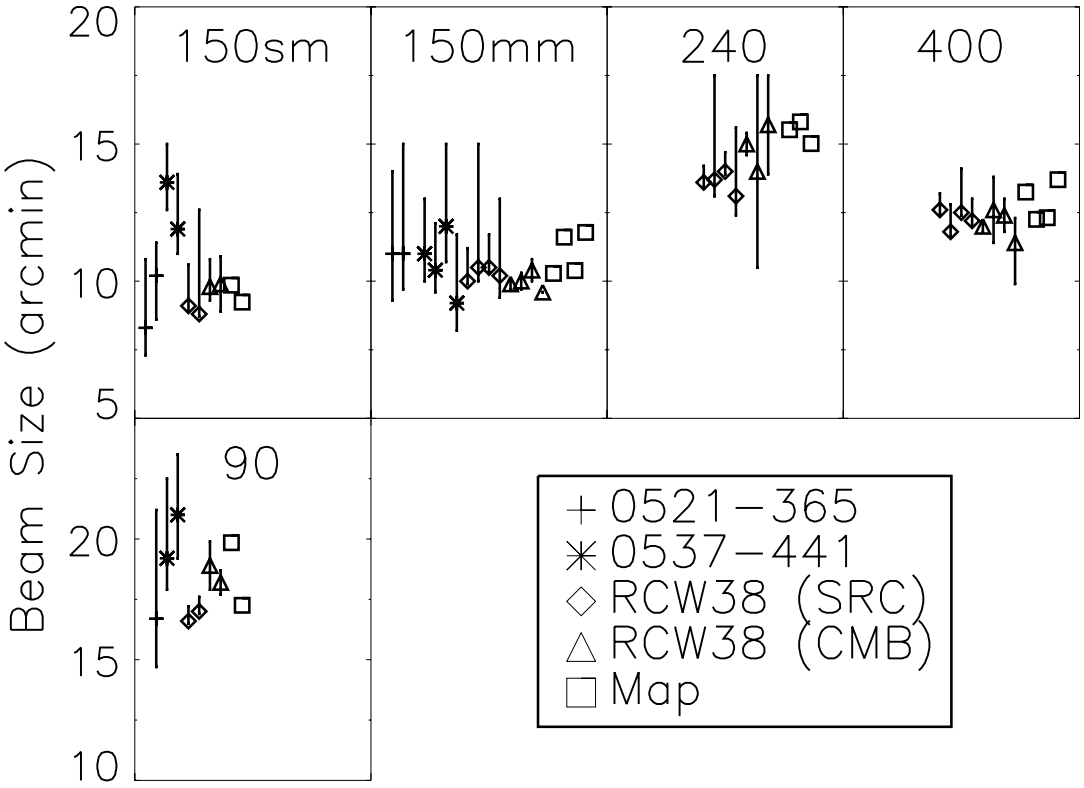

Figure 6.6:
Summary of the beam FWHMs for all the channels derived using the three in-flight methods. "0521-365" and "0537-441" are the beam sizes derived from the radial profile of the two brightest extragalactic point sources. "RCW38 (SRC)" is the beam size derived from the targeted observation of RCW38, and "RCW38 (CMB)" is from the serendipitous observation of RCW38. "Map" is the beam size derived from the 2D binned source maps.

(quadrants) for the Galactic HII regions RCW38, IRAS/08576, IRAS/1022, NGC3603 and NGC3576. The extragalactic point sources did not have high enough signal-to-noise to place constraints on the shoulder.

A Gaussian plus a constant were fit to the radial profiles for each quadrant. For the 150 GHz channels, the constant was fit to data with radius $25' < r < 30'$ and the Gaussian was fit to the data with radius $0' < r < 8'$. For the 90 GHz channels, the constant was fit to data with radius $35' < r < 45'$ and the Gaussian was fit to the data with radius $0' < r < 12'$. Since NGC3603 and NGC3576 are only separated by $23'$, a circular region around the other source was masked out before the radial profile was computed.

The amplitude and power contained in the residual shoulder is calculated. The residual

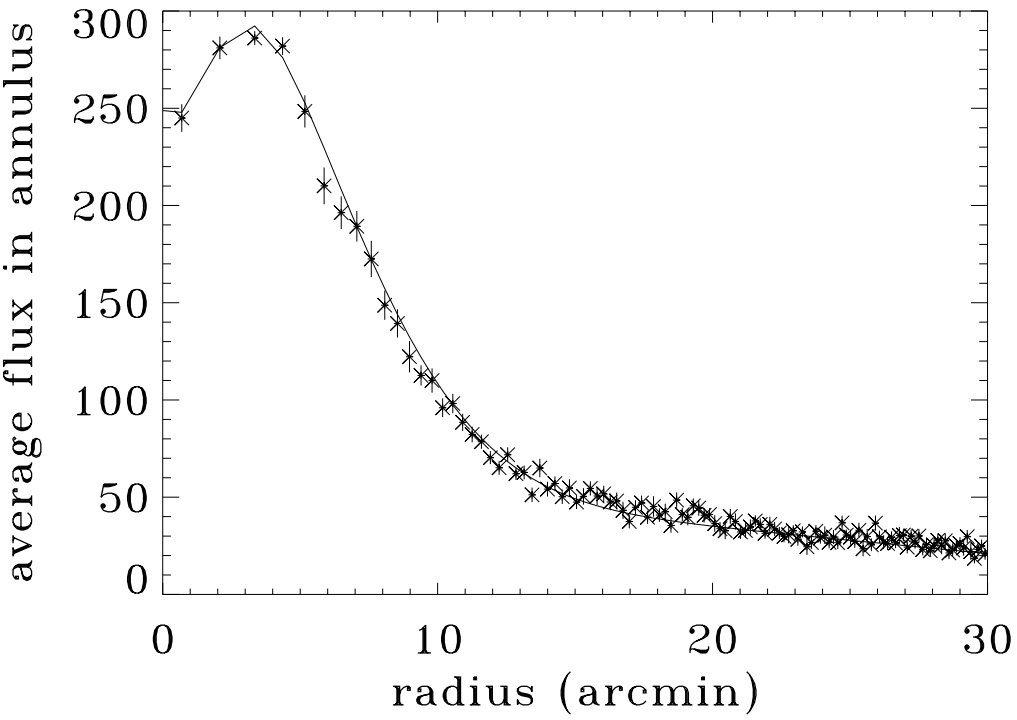

Figure 6.7:
Double-Gaussian fit to RCW38 B220A2. The FWHM of the main lobe is 13.0′ and the FWHM of the smaller inverted lobe is 4.2′.

area is defined to be area(residual)/area(data-const) for those same two fits, or $\sim$ shoulder/total. The area of data-const is measured between 0′ and 30′. The residual area is measured for r between 5′ and 30′. The area is in terms of power (throughput) in the beam. An example plot for one source and quadrant is shown in Figure 6.8.

The best limits on a shoulder in the 90 GHz and 150 GHz beams from Galactic sources come from NGC3576, and limit it to about 15% of the throughput in channel 150A. Repeating the shoulder analysis on IRAS 100 μm data reveals residuals of similar size, implying a Galactic origin for the residual. Therefore, the best limits on the shoulder come from the ray-trace model of the optics combined with the ground measurements of the beam.

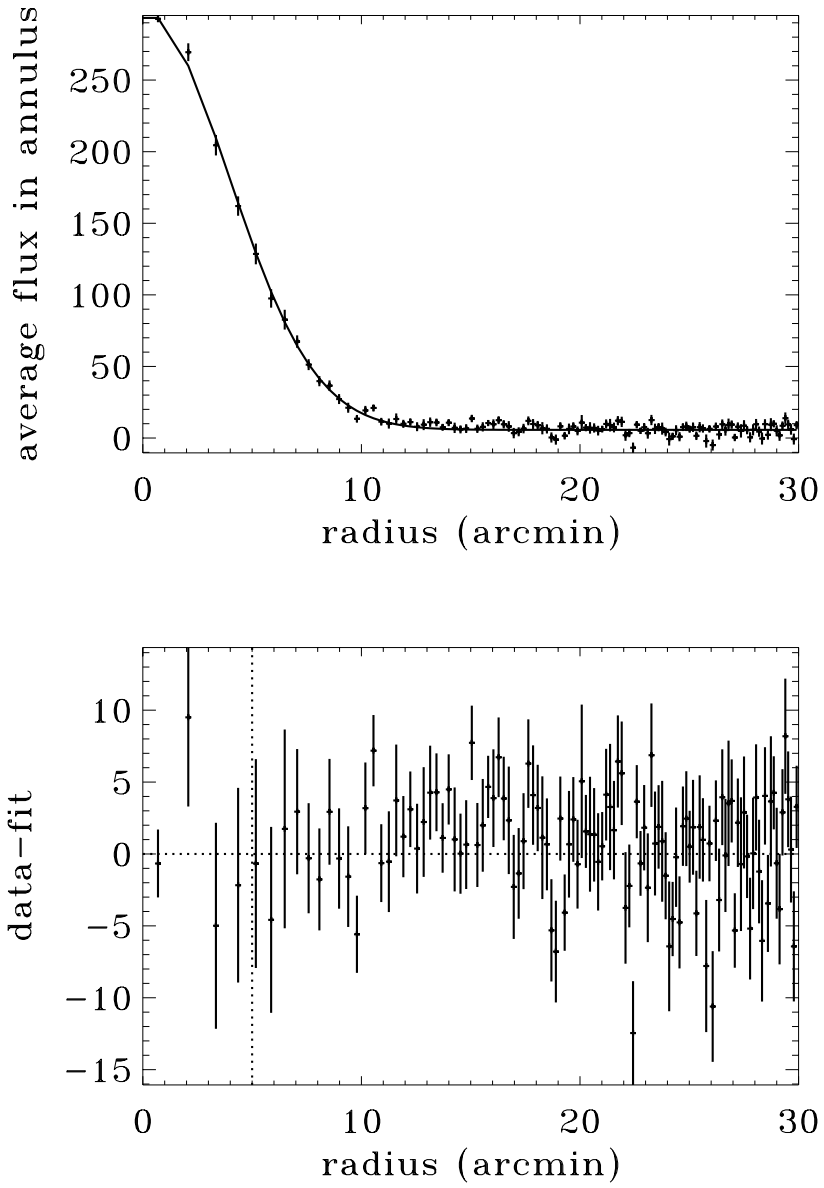

Figure 6.8:
The top panel shows the radial profile and fits for one of the quadrants for the NGC3576 observations in channel 150A. The bottom panel shows the residuals to a fit of a Gaussian plus a constant.

6.7 Deglitching

The BOOMERANG bolometer data are contaminated with transient events which must be flagged and removed; these include cosmic ray hits, thermal events in the 0.3 K stage, calibration lamp signals, and short periods of electromagnetic interference (EMI).

Large thermal events in the 0.3 K stage, atmospheric signal due to changes in telescope elevation, and signals from the calibration lamp appear simultaneously in all channels and are easily flagged. Smaller thermal relaxation events were found with a pattern matching algorithm. Cosmic ray hits, EMI spikes, and smaller thermal events occurring within an individual bolometer are found using two algorithms. First, large spikes are detected as deviations of greater than 3σ in a three point difference function of the time ordered data, defined by $\delta_i = d_i - 0.5(d_{i-1} + d_{i+i})$, where σ refers to the standard deviation of the data. Smaller glitches are found using an iterative binning scheme; the time stream data are binned into pixels on the sky and individual samples more than 4σ from the average value of a pixel are flagged and not used in the next iteration. After 4 iterations, a negligible number of new glitches are found.

Drifts in the bolometer data due to large cosmic ray hits are removed by fitting a parabola to the data. Drifts induced by large thermal events are fit to an exponential and removed. The flagged data are replaced by a constrained realization of the noise and not used in subsequent analysis. Approximately 5% of the data in each channel are contaminated by glitches.

6.8 Transfer Function

A cosmic ray hit on a bolometer is well approximated by a delta function in power input, and can be used to measure the transfer function of the bolometer and electronics. The transfer function of the experiment is parameterized by three time constants; the thermal time constant of the bolometer, the time constant of the AC-coupling filter and the time constant of the anti-aliasing filters in the readout electronics. The AC-coupling and anti-aliasing time constants are measured on the ground and are expected to be the same in flight since the electronics operating temperature in flight is similar to that on the ground. The bolometer time constant is highly sensitive to the background optical load, however, and should be measured in flight.

The combination of the theoretical transfer function of the bolometer (a single pole low pass filter) and the measured electronics transfer function is Fourier transformed into the time domain to obtain the impulse response function.

A database of cosmic ray hits is built for each channel, simultaneously fitting an ampli-

channel	Cal lamp	CosRay	HugeCR	Ping	Elev	Bias	Trim	Total
B90A	0.68	0.79	0.58	0.30	0.93	0.80	1.2	5.3
B90B	0.71	0.87	0.59	0.093	1.2	0.86	1.3	5.6
B150A	0.63	0.42	0.60	0.22	0.85	0.81	0.78	4.3
B150B	0.67	0.79	0.45	6.5	0.81	0.80	1.7	11.7
B150A1	0.63	1.2	0.37	0.37	0.82	0.80	1.62	5.8
B150A2	0.62	0.58	0.37	0.29	0.86	0.80	0.94	4.5
B150B1	0.63	0.66	0.37	0.45	0.83	0.81	1.1	4.8
B150B2	0.63	0.47	0.31	0.52	0.84	0.81	0.84	4.4
B240A1	0.64	0.53	0.23	0.43	0.82	0.81	0.86	4.3
B240A2	0.64	0.57	0.36	0.58	0.81	0.80	0.93	4.7
B240B1	0.63	0.52	0.18	0.44	0.82	0.82	0.88	4.3
B240B2	0.63	0.19	0.28	0.0053	0.80	0.81	0.48	3.2
B400A1	0.63	0.32	0.16	2.9	0.81	0.81	1.1	6.6
B400A2	0.63	0.48	0.11	0.74	0.81	0.81	0.90	4.5
B400B1	0.63	0.38	0.14	0.65	0.83	0.82	0.79	4.2
B400B2	0.63	0.45	0.14	2.2	0.81	0.81	1.1	6.2
DarkA	0.63	0.20	0.025	2.1	0.81	0.81	0.87	5.5
DarkB	0.63	0.37	0.34	5.6	0.83	0.81	1.38	9.9
GNDFET	0.62	0.059	0.0016	0.035	0.81	0.81	0.43	2.8
LoadRes	0.62	0.10	0.021	0.045	0.81	0.81	0.49	2.9

Table 6.5:
Percentage of data flagged in each channel for each glitch type. "Huge CR" refers to cosmic ray hits which saturate the amplifier. "Ping" refers to RF interference, "Elev" refers to data which are unusable due to changes in telescope elevation, "Bias" refers to data which are unusable due to changes in the bolometer bias, and "Trim" refers to some extra data removed around the edges of large events to prevent ringing.

tude and phase shift to each hit as well as fitting the data to the impulse response function. Figure 6.9 shows the best fit template and the cosmic ray data for one of the 150 GHz channels. The best fit bolometer time constants for each channel are listed in Table 6.8.

The cosmic ray method is very precise in the measure of the high frequencies in the transfer function. The low frequency side of the function is dominated by the AC-coupling filter. The ground measured high pass time constants have been confirmed to be identical to those in flight by checking the behavior of the data in time domain after a step in the input signal. Steps in the signal are produced by changes in the bolometer bias voltage amplitude and by elevation changes which change the column depth of atmosphere viewed by the detectors.

Channel	average time between glitches (s)
90A	32
90B	28
150A	72
150B	27
150A1	19
150A2	46
150B1	35
150B2	61
240A1	56
240A2	32
240B1	53
240B2	278
400A1	79
400A2	53
400B1	71
400B2	57
Dark A	65
Dark B	72
Lres	324
GndFET	193

Table 6.6:
Average time between glitches. The average over all channels is 43 seconds between glitches. In channel 240B2, many smaller glitches were lost in the extraordinarily high noise (see Table 4.13), resulting in a longer time between glitches than in other channels.

6.9 Detector Noise

The voltage noise is determined by taking the power spectrum of the deglitched time domain data. To compute the Noise Equivalent Temperature (NET), the voltage noise is divided by the responsivity of the detector. In addition, the voltage noise spectrum is deconvolved with the detector transfer function. Figure 6.10 shows the NET as a function of frequency of channel 150A.

During the 1°/s scans at 45° elevation, a signal on the sky with spherical multipole moment of $\ell = 200$ is mapped to a frequency of 0.38 Hz, well above the 1/f knee of the detector system, but near the natural pendulation frequency of the gondola.

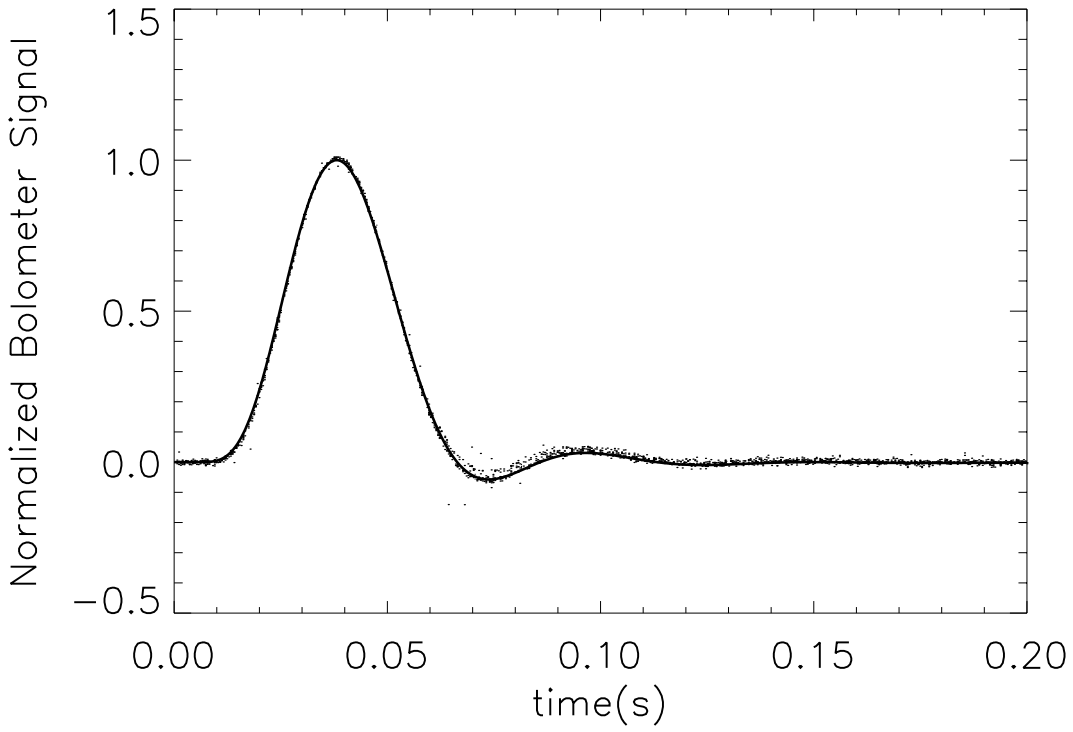

Figure 6.9:
The best fit impulse response function to cosmic ray hits for one of the 150 GHz bolometers.

6.10 Scan-synchronous Noise

During the CMB scan mode, scan-synchronous noise (SSN) appeared at the fundamental and first harmonic of the scan frequency. See Figure 6.11 for a sample section of calibrated time-ordered data from Channel 150A. The amplitude of the SSN is very different at the two different scan speeds of 1°/s and 2°/s. At 90, 150, and 240 GHz, the 1°/s signal is very well fit by the cosmological dipole, but at 2°/s the SSN is much larger than the dipole and additionally has a large component at the first harmonic of the scan frequency.

The SSN is correlated between channels and has an amplitude which increases with electromagnetic frequency; it is largest in the 400 GHz channels and smallest in the 90 GHz channels.

To investigate the nature and origin of the SSN, a spectral analysis was done on the 1.5 hours of data obtained in spin mode. The data are binned into angle on the sky. A

Channel	target	lab	flight	bolo type
B90A	24	19.9 (24.5)	22.48	5.6
B90B	24	18.7 (31.8)	21.92	5.6
B150A	15	11.4	10.8	3.4
B150B	15	12.2	13.3	3.4
B150A1	15	10.3	13.3	3.4
B150A2	15	10.3	12.0	3.4
B150B1	15	12.7	16.3	3.4
B150B2	15	16.75	21.2	4.8
B240A1	10	6.77	8.898	M1
B240A2	10	8.84	7.24	M1
B240B1	10	9.36	10.567	M1
B240B2	10	7.07	8.77	M1
B400A1	6	< 6	4.184	M2
B400A2	6	10.6	9.92	M2
B400B1	6	< 6	4.464	M2
B400B2	6	< 6	4.298	M2
DarkA	6		3.037	M2
DarkB	15		24.422	3.4

Table 6.7:
The bolometer time constant measured pre-flight in the lab, in-flight, and the detector type. Types 3.4, 4.8, and 5.6 refer to the low G detectors with absorber diameters 3.4mm, 4.8mm, and 5.6mm, respectively. Types M1 and M2 are higher G detectors with absorber diameters of 4.0mm.

galaxy template and a SSN template were simultaneously fit to the binned data. The galaxy template was obtained from the Schlegel map at 100 μm [63]. The SSN template was a cosine signal with phase selected such that the peak signal is centered on the direction of the sun. The ratio of SSN amplitude to galaxy amplitude was fit to a power law. Each of the four multi-color photometers were analyzed separately and a spectral index of 2 ± 0.5 was found for the SSN relative to the galaxy.

Since the galactic signal is expected to rise as $\nu^{2.7}$, the SSN has an absolute spectral index as large as 5. The large spectral index is consistent with both an atmospheric signal and sunlight scattered from either the balloon or from the atmosphere. In addition, the sidelobe response could potentially have a strong spectral dependence. However, the SSN also has a very strong dependence on scan speed (i.e., Figure 6.11), indicating a mechanical resonance effect. Atmospheric signal due to gondola pendulation is the only source of this noise that could have such a strong dependence on scan speed.

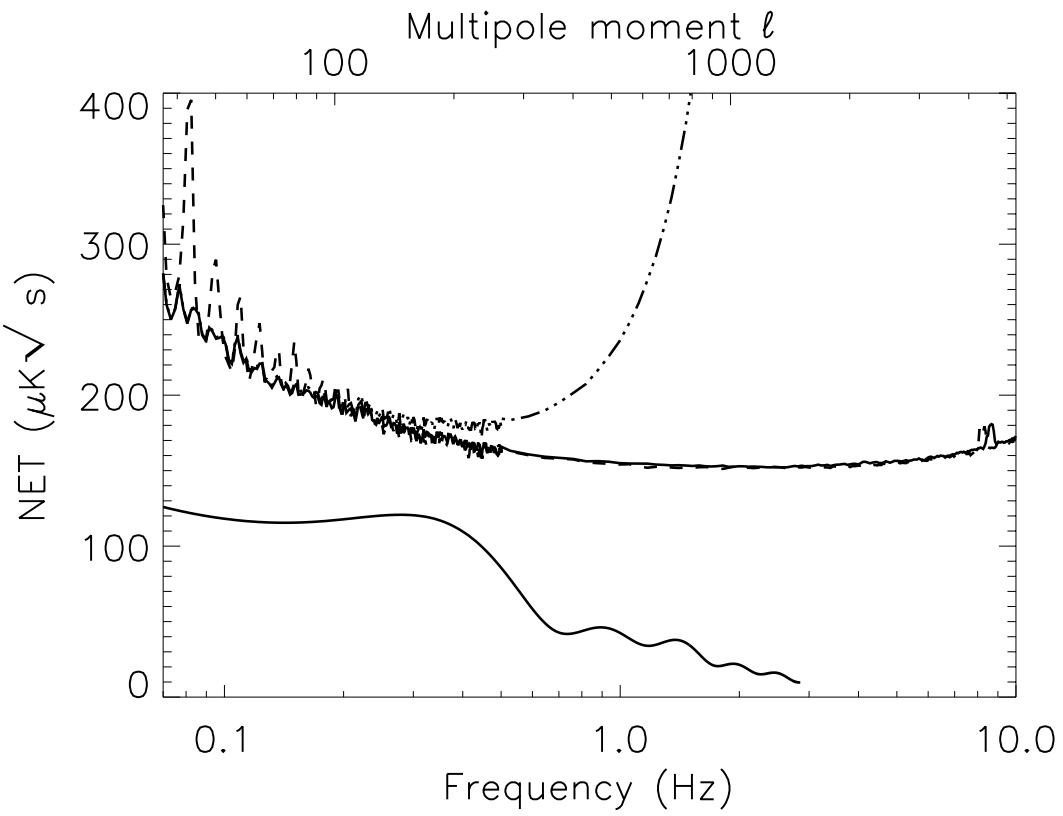

Figure 6.10:
Two noise spectra of channel 150A during 1°/s mode (solid line) and 2°/s mode (dashed line). The lines at $f < 0.1$ Hz are harmonics of the scan frequency. The rise in NET at high frequency is due to the bolometer's time constant $\tau = 10.8$ms. The top x-axis shows the corresponding spherical harmonic multipole for the 1°/s mode. The dashed line shows the 1°/s noise spectrum convolved with the window function of a $10'$ beam. The solid line shows the signal due to CMB anisotropy assuming the best fit B97 model.

6.11 Flight Load

The optical background on each detector can be calculated from the temperature rise through the relation

$$Q = \frac{\Delta T}{G} \tag{6.1}$$

where Q is the optical load, ΔT is the temperature rise of the bolometer, and G is the thermal conductivity. An effective Rayleigh-Jeans temperature can be assigned by solving

$$Q = \int 2k_B T_{RJ} \frac{\nu^2}{c^2} A\Omega \eta_{opt} t_\nu d\nu \tag{6.2}$$

for T_{RJ}, where $A\Omega$ is the throughput, η_{opt} is the optical efficiency, and k_B is Boltzmann's

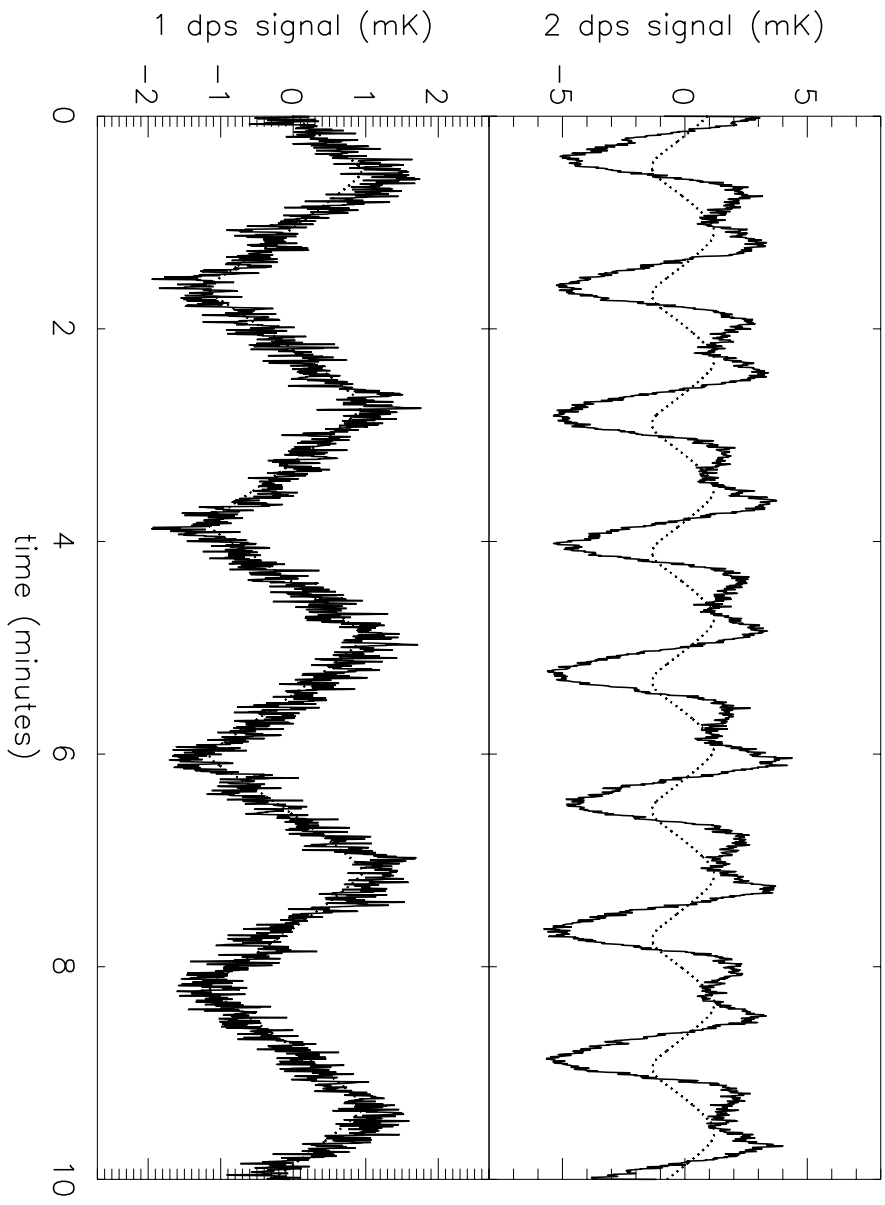

Figure 6.11:
A sample section of deglitched, calibrated time ordered data for channel 150A for each of the scan modes. The bandwidth has been limited to 2 Hz to show the low frequency signal. The best fit dipole is overlaid in each panel.

constant. See Table 6.11 for the calculated values of Q and T_{RJ} for each channel, including the dark channels. Section 7.6 discusses the method of measuring in-flight optical efficiency.

Another method of computing the background load temperature is to fit a Rayleigh-Jeans spectrum to the optical power as a function of frequency which results in a tempera-

ture of 9.5 K.

A better measurement of the $R(T)$ parameters (Δ and R_0) would result in a more accurate and reliable measurement of the in-flight loading. The parameters were assumed to be the same for entire set of bolometers; however, in practice there is normally some dispersion in their values.

Channel	G pW/K	ΔT mK	Q pW	T_{RJ} K
90A	81	23	1.9	4.3
90B	82	35	2.9	6.9
150A	81	11	0.9	2.6
150B	88	15	1.3	3.8
150A1	88	31	2.7	10.7
150A2	104	33	3.5	11.2
150B1	90	39	3.5	13.7
150B2	73	44	3.2	11.5
240A1	181	33	6.1	10.6
240A2	180	20	3.4	4.3
240B1	195	33	6.5	12.5
240B2	202	24	4.9	7.2
400A1	519	29	14.9	12.6
400A2	412	13	5.5	7.4
400B1	422	31	13.0	12.3
400B2	424	8	3.6	5.0
Dark A	377	119	45.0	
Dark B	28	6	1.6	

Table 6.8:
The estimated background on each detector during flight.

Chapter 7 Calibration

The absolute responsivity of BOOMERANG during the 1998 LDB flight was measured in three different ways. First, the calibration measured on the ground was extrapolated to the flight background conditions. Second, the responsivity to the CMB dipole was measured. Third, the responsivity to galactic and extragalactic sources in flight was measured.

As a check, the relative responsivity of the BOOMERANG channels was measured by comparing the signals measured at degree scales in the CMB maps as well as comparing power spectra of different channels.

7.1 Lab Scaled to Flight

The responsivity of the detectors measured in the lab can be scaled to flight conditions using the following relation for the responsivity of a bolometer:

$$S = \frac{\alpha V}{G - \alpha P_e} \tag{7.1}$$

where G is the thermal conductivity, V is the DC voltage across the bolometer, P_e is the electrical power dissipated in the bolometer, and $\alpha = \frac{1}{R}\frac{dR}{dT}$. The term that varies the most between flight and ground conditions is the bolometer voltage V. The quantities α, G, and P_e change by only a few percent, so to a first order approximation, the responsivity is proportional to the bolometer voltage. Scaling the responsivity measured on the ground by the ratio of the DC bolometer voltages measured in flight and on the ground yields an estimate of the responsivity in flight.

This method of calibration has several drawbacks. First, it fails to take into account any vignetting of the beam by the neutral density filters. Second, its precision is dependent on knowledge of the transmission of the neutral density filters, which is known to an accuracy of only $\sim 20\%$.

7.2 Dipole

The 90, 150, and 240 GHz bolometer signals can be calibrated from their response to the CMB dipole anisotropy. The CMB dipole is due to the motion of the Earth relative to the CMB, and is an ideal calibration source for a CMB mapping receiver. Its amplitude has been measured to high precision (0.7%) by COBE/DMR [31]. Its spectrum is identical to that of the degree-scale anisotropy and it entirely fills the BOOMERANG beams. This reduces the final calibration error by eliminating uncertainty in the measured spectral frequency response of each channel and in the beam pattern of the telescope.

The equator of the CMB dipole is roughly orthogonal to the BOOMERANG scan direction through the center of the $\pm 60^\circ$ CMB scan mode. The dipole appears as a $\sim$3 mK peak-to-peak signal in the timestream, much larger than the detector noise.

The motion of the Earth relative to the Sun changes the amplitude and direction of the dipole (see Figure 7.1). At the time of the BOOMERANG flight, the motion of the Earth around the Sun increases the apparent amplitude of the dipole from the average value by 8%.

The dipole signal appears at f=0.008 Hz and f=0.016 Hz during the 1°/s and 2° CMB scan modes, respectively. At such low frequencies the detector signals are sensitive to 1/f noise, uncertainties in the measurement of the transfer function, and scan synchronous noise.

Low-resolution ($55'$ pixel size) maps of the bolometer data are constructed using the iterative maximum likelihood map-making scheme of [58]. The data are split into the 1°/s and 2°/s scan modes. The 1°/s maps are fit to a model dipole with direction and amplitude fixed by the COBE/DMR measurement of the cosmological dipole, as shown in Figures 7.3 and 7.2.

The galactic plane lies at one edge of the map, and bright galactic dust in the plane can create a spurious dipole signal. The sign of the effect is such that the amplitude of the total dipole increases with more dust. Therefore, if galactic signal is present, it results in an under-estimation of the responsivity. To avoid galactic dust altogether, only pixels that lie at galactic latitudes b<-15 are used in the dipole fit. Cutting more data is observed to have no effect on the measured responsivity.

During the CMB scan mode, scan synchronous noise appeared at the fundamental scan

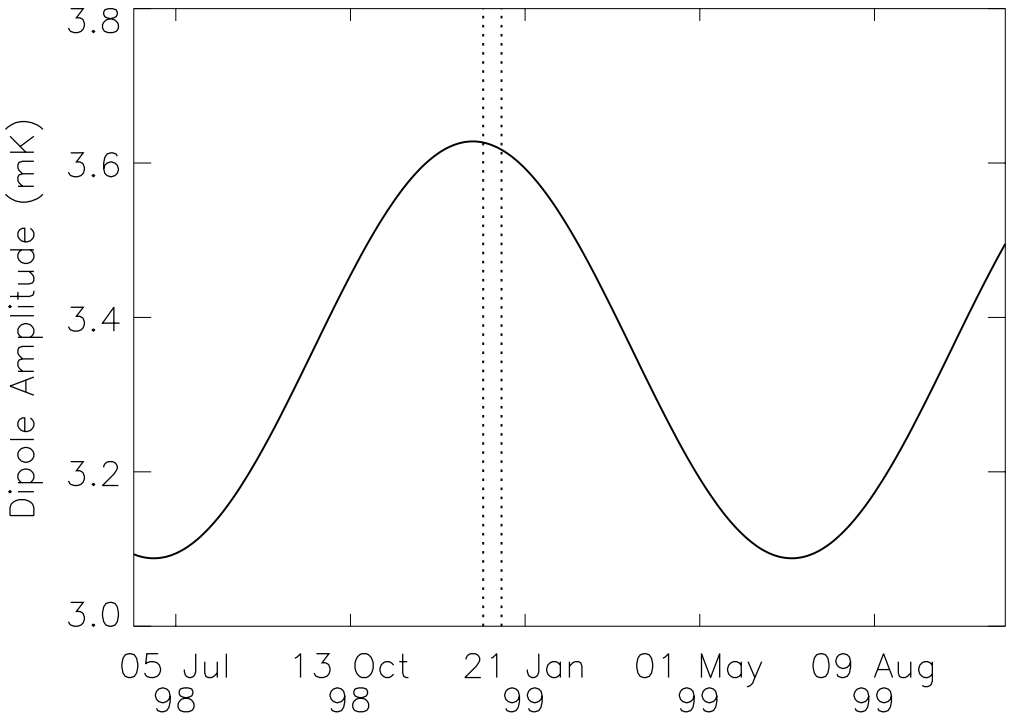

Figure 7.1:
The amplitude of the CMB dipole as a function of time. The time of the BOOMERANG flight above Antarctica is denoted by the vertical dotted lines. The yearly variation is due to the motion of the Earth around the Sun.

frequency. In the 150 GHz and 240 GHz channels during the 2°/s mode, this appeared as a signal larger than the signal from the dipole. The scan synchronous noise is well correlated with the 400 GHz channels, and a 400 GHz map is used as a template to model the noise. The 2°/s data are simultaneously fit to the dipole model and to the 400 GHz template, and the measured response to the dipole agrees to within 10% of the 1°/s fits in all channels (Table 7.2). See Figure 7.4 for a histogram of the ratios of the 1°/s calibration to the 2°/s calibration.

The 1°/s data are also simultaneously fit to a dipole model and a 400 GHz template. The resulting dipole fit amplitude from the simultaneous fit varies from the single component fit by less than 1% in the 90 GHz and 150 GHz channels and by $\sim 1\%$ in the 240 GHz channels (Table 7.2). We conclude that scan synchronous noise is not a significant contaminant to the 1°/s data.

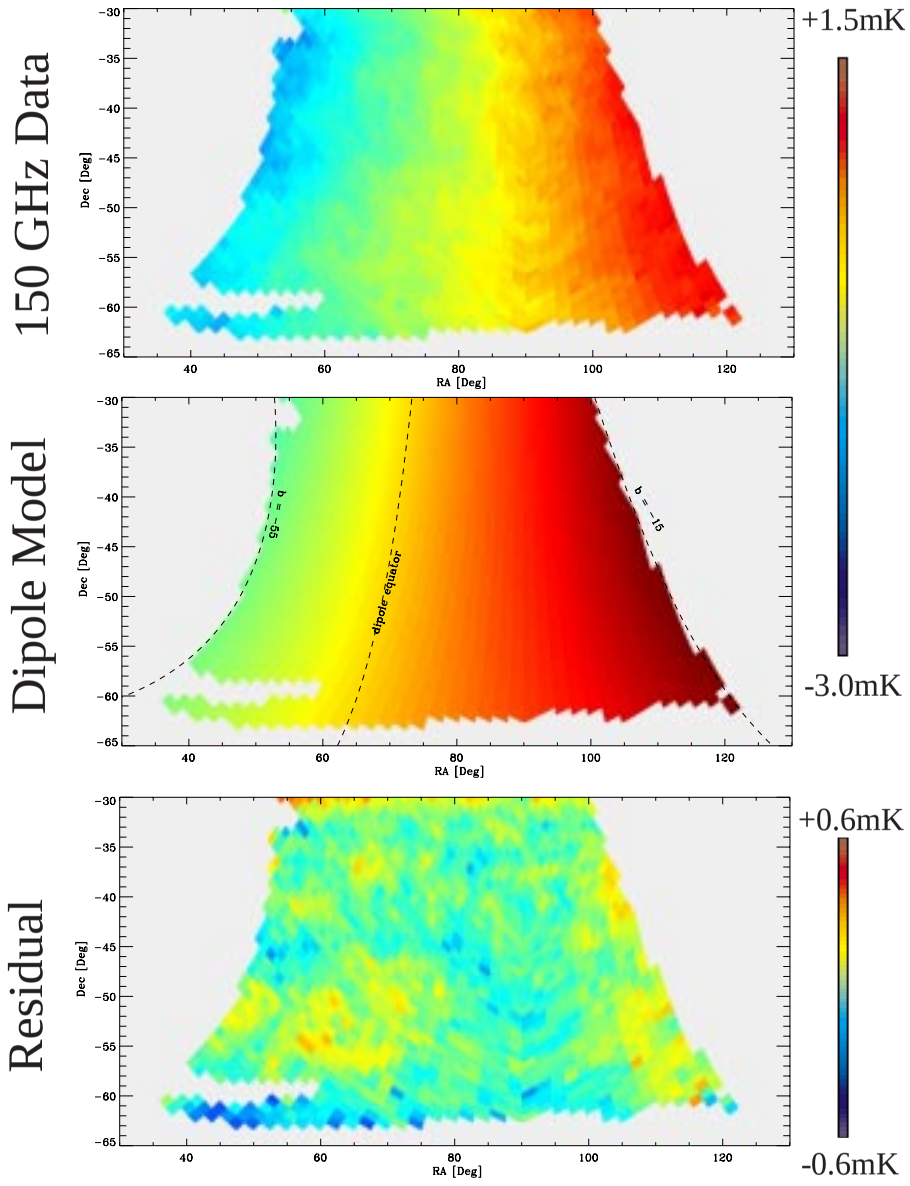

Figure 7.2:
The dipole fitting procedure. The top panel shows a map from BOOMERANG channel 150A in 1°/s mode. The middle panel shows the dipole model for this map, and the bottom panel shows the residual from the fit.

The agreement of the 1°/s and 2°/s results provides checks for additional systematic effects (Table 7.2). Since the dipole signal frequency is a factor 2 different, we conclude that the results are not biased by incorrect knowledge of the electronic transfer function. In CMB scan mode, the dipole appears at a signal frequency of 0.008 Hz and 0.016 Hz at 1°/s

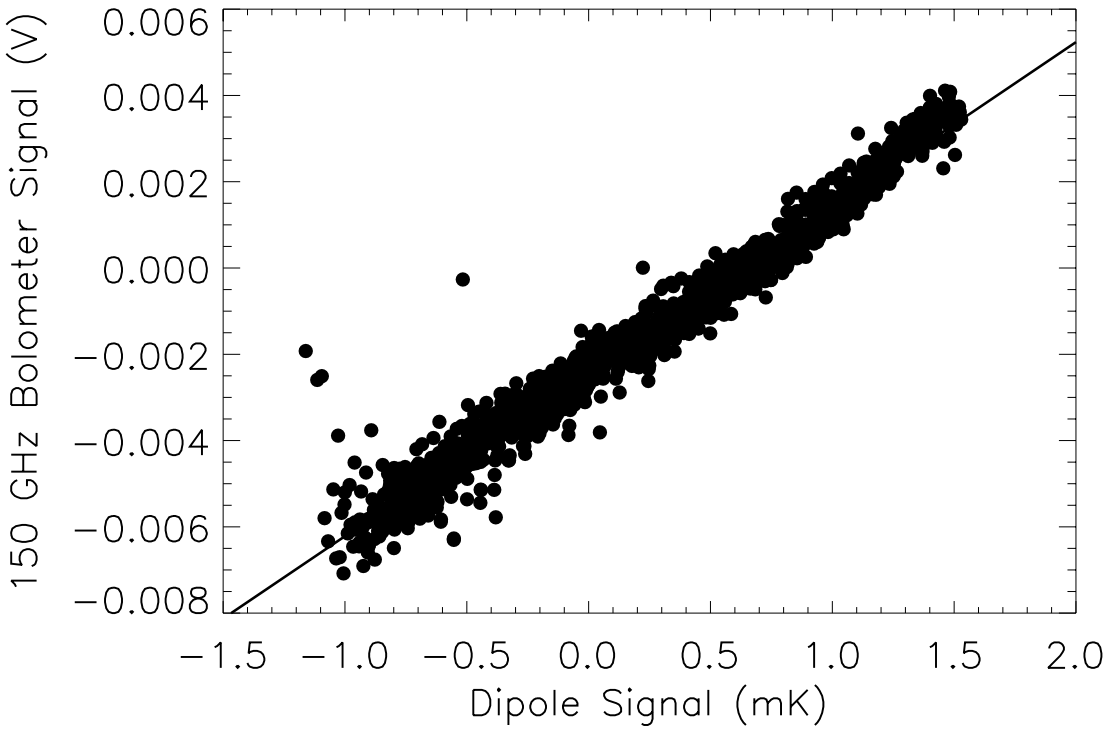

Figure 7.3:
BOOMERANG channel 150A 1°/s map fit to a dipole model.

and 2°/s, respectively. The transfer function of the electronics at these two frequencies has amplitudes of 0.47 and 0.73, respectively. Additionally, the 2°/s data were taken during the first half of the flight and the 1°/s data were taken during the second half of the flight, between which the Sun moved 5° on the sky and the payload traveled hundreds of kilometers.

The degree scale anisotropies were measured with high signal to noise. To check that the spectrum of the observed dipole signal matches that of the degree scale anisotropies, the relative response of each detector to the degree anisotropies were measured and agree with those of the dipole anisotropies to within $1\sigma = 8\%$. See Figure 7.5 for a histogram of the relative to absolute calibration ratios. Section 7.3 discusses the relative calibration in more detail.

Removal of the scan-synchronous noise limits the precision of the dipole calibration. A conservative measure of how well the scan-synchronous noise is removed is 10%, which is the level of agreement between the 1°/s and 2°/s calibrations. We therefore assign an error of 10% to the dipole calibration.

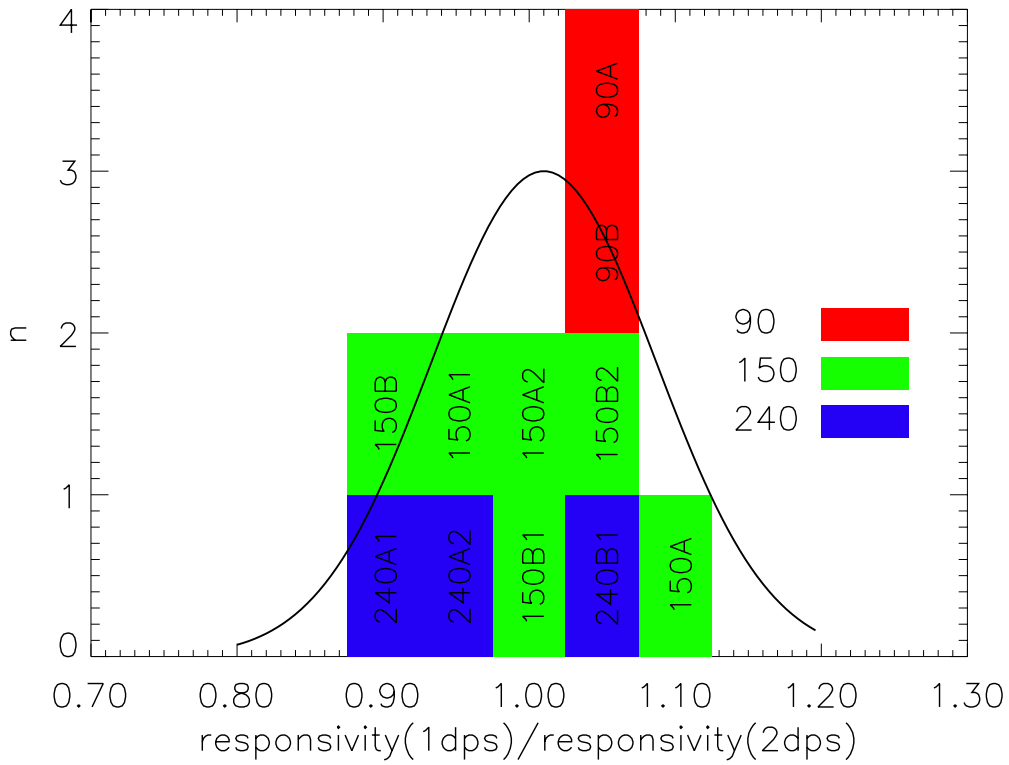

Figure 7.4:
A histogram of the ratio of the responsivity obtained with 1°/s data to that obtained with 2°/s data. The solid line shows the best fit Gaussian, which has a 1 $\sigma = 0.08$ and an offset of 0.01. The mean and standard deviation at each frequency are shown in Table 7.2. There is no statistically significant skew as a function of frequency.

7.3 Relative Calibration

A relative calibration between channels was determined by measuring the relative response to degree scale structure. This was done with two different methods; comparison of maps and comparison of power spectra.

Comparison of maps was done using a simple linear fit of one map to another. Points were weighted by the standard deviation. The maps were created using the iterative technique described below and were degraded to 55′ resolution to remove any decorrelation due to mis-matched beams. Only a high signal-to-noise region of the maps far from the galaxy was selected; right ascension $65° < \alpha < 105°$ and declination $-55° < \delta < -35°$. Figure 7.6 shows the scatter plots of the 150A map compared with other maps and the best fit lines.

A second method of relative calibration was to fit the power spectra of various channels

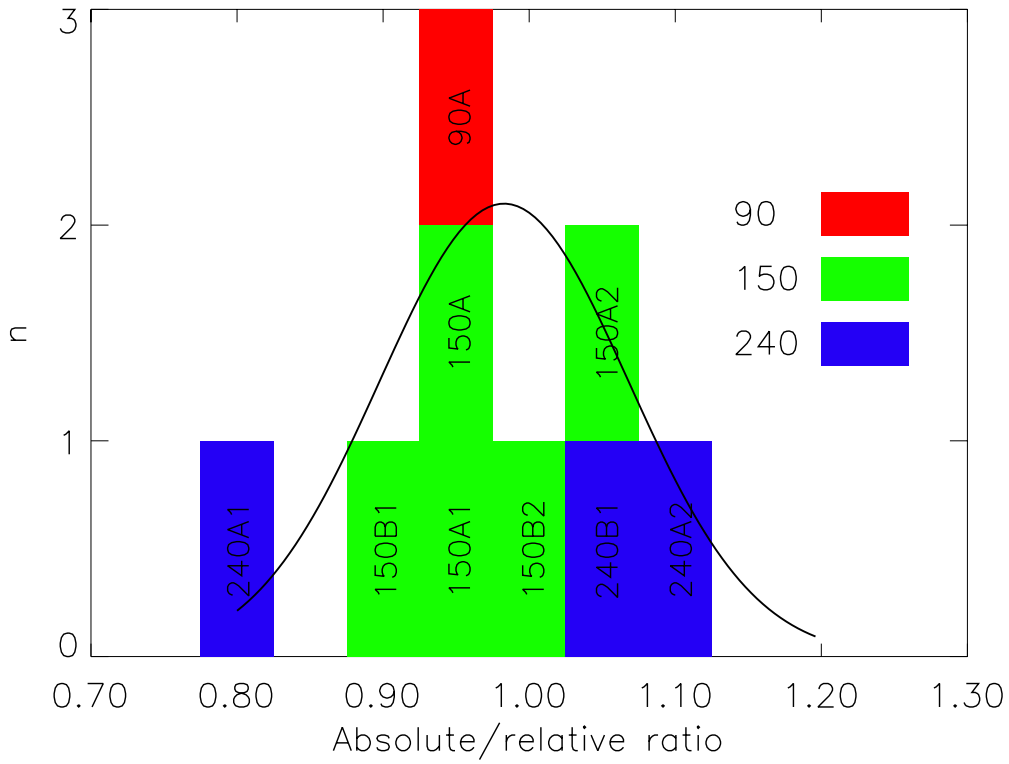

Figure 7.5:
A histogram of the ratio of the relative to absolute responsivity. The solid line shows the best fit Gaussian, which has a 1 $\sigma = 0.08$ and an offset of -0.017. Channel 240A1 appears to be an outlier, but is 1.6σ from the mean, which happens 11% of the time. The mean and standard deviation at each frequency are shown in Table 7.2.

over the range $50 < \ell < 550$, which is dominated by signal. Table 7.3 compares this method with the map fit method. The methods do not yield identical results, but generally agree to a similar precision.

7.4 Sources

The BOOMERANG observations of galactic and extragalactic sources provide other means of calibrating the receiver. Extended millimeter wave observations of these sources have never previously been made, however. In addition, there is evidence that some of the sources are variable [1] [14] [19]. Follow-up observations of the galactic sources NGC3576 and RCW38 and the extragalactic sources 0521–365 and 0537–441 were made at the SEST telescope at

channel	fiducial $\mu V/K_{CMB}$	1°/s no 400 rm	2°/s 400 rm	2°/s no 400 rm
90A	68	1.009	1.072	1.92
90B	67	1.009	1.092	1.82
150A	76	1.003	1.129	1.60
150B	78	1.019	0.949	1.84
150A1	49	1.007	0.986	2.21
150A2	67	1.009	1.041	1.72
150B1	54	0.992	1.027	1.99
150B2	50	0.987	1.082	1.97
240A1	48	0.985	0.950	2.82
240A2	68	0.997	0.992	2.21
240B1	45	0.975	1.082	3.15

Table 7.1:
Systematics tests applied to the responsivity to the dipole. The "fiducial" calibration is the 1°/s. The other columns show the ratio of the fiducial responsivity to the responsivity measured at 2°/s with and without a 400 GHz channel fit out and to the responsivity measured at 1°/s without a 400 GHz channel fit out. The importance of fitting a 400 GHz channel to the heavily contaminated 2°/s data can be seen by the level of disagreement of the last column, where scan synchronous noise mimics a dipole. The mean and standard deviation at each frequency are shown in Table 7.2.

Test	90 GHz	150 GHz	240 GHz
1°/s 400rm/no400rm	+0.4±0.7%	+0.3±1.2%	-1.4±1.1%
1°/s / 2°/s	+8.2±1.4%	+3.5±6.5%	+0.8±6.7%
dipole/relative	+11±7.9%	-2.0±3.1%	-5.3±11%

Table 7.2:
The average and standard deviation of systematics tests results at each frequency. The removal of a 400 GHz channel and the comparison between the 1°/s and 2°/s data show no frequency dependence. The comparison of the relative to absolute calibration shows a slight (but barely statistically significant) frequency dependence.

90 GHz and 150 GHz in La Silla, Chile, between January 8-10, 2000 [17] ($\sim$ 1 year after the Antarctic flight of BOOMERANG). The size of the SEST beam is $57''$ FWHM at 90 GHz and $35''$ FWHM at 150 GHz. The SEST data are convolved with the BOOMERANG beam to calibrate the 150 GHz and 90 GHz channels.

Two maps were made of each source and later combined: a center map ($4' \times 4'$ in extent) and an extended map ($10' \times 10'$ for NGC3576 and $6' \times 6'$ for RCW38). The grid spacing is $17.5''$ in the center maps and $35''$ in the extended maps. The total integrated

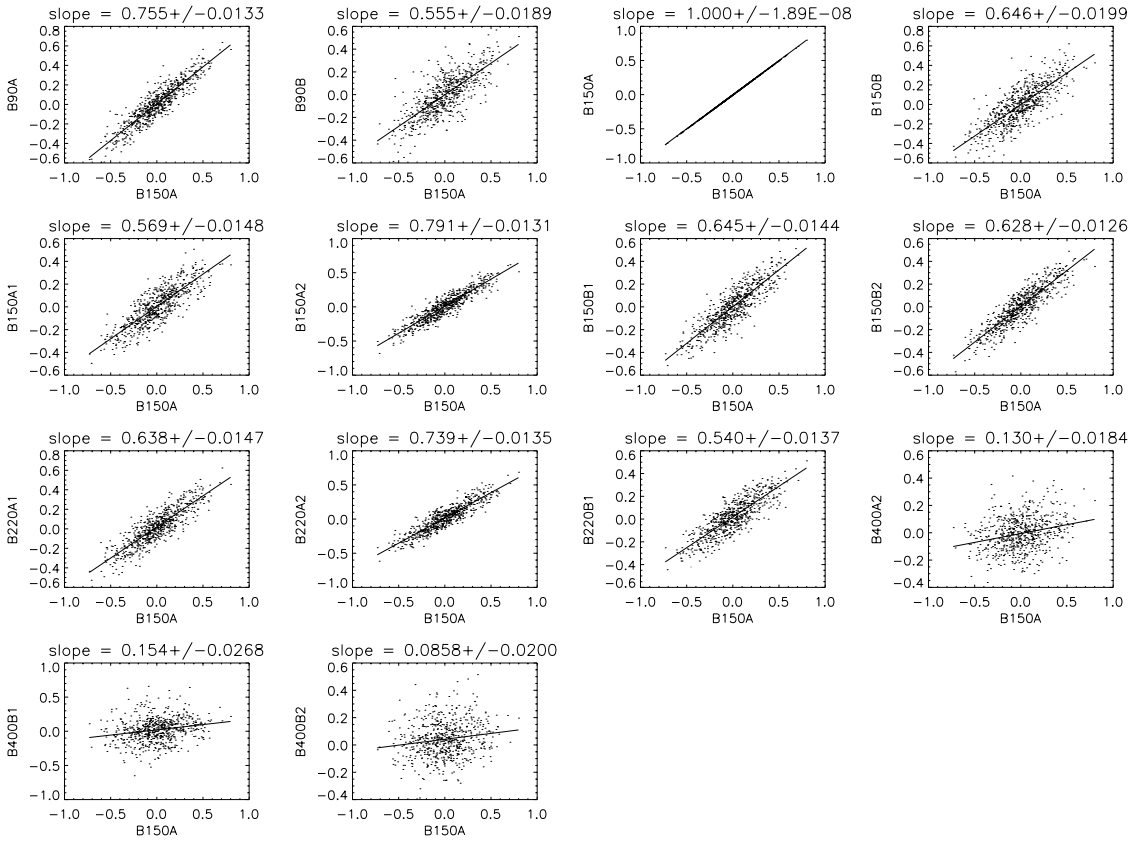

Figure 7.6:
The relative calibration determined by comparison of each map to the 150A map. The noisy channels 240B2 and 400A1 have been excluded. The units on the axes in each panel are millivolts.

flux was computed for the Boomerang observations. The integrated convolution of the SEST observations with the Boomerang (SEST*BOOM) observations was also computed. Each of the integrals is calculated for 1σ, 2σ fluxes, where 1σ and 2σ fluxes are the total integrated fluxes within a radius equal to 1 and $2\sigma_{beam}$, respectively.

Observations of NGC3576 at 150 GHz with the MAT experiment [59] are used to verify the SEST measurements. The integrated convolution of the MAT observations with the SEST observations (SEST*MAT)was computed and compared with the integrated flux from the MAT map alone. The ratio MAT/(SEST*MAT) is 1.01, 1.00, and 0.99 for the peak flux, and the 1σ and 2σ integrated fluxes, respectively. This implies that the SEST and MAT observations agree to within a few percent.

The flux ratio (BOOM)/(SEST$*$BOOM) was computed for each channel using the dipole calibration for Boomerang. For NGC3576 the results from the convolution with the SEST

Channel	map	power spectrum
90A	1.161	0.985
90B	1.049	
150A	1.000	1.000
150B	0.938	
150A1	0.948	0.988
150A2	1.014	1.064
150B1	1.002	0.943
150B2	0.976	1.018
240A1	0.828	0.845
240A2	1.041	1.108
240B1	0.971	1.063

Table 7.3:
The ratio of absolute to relative responsivity calculated with the two different methods. The absolute responsivity is from the dipole calibration and the relative calibration is determined by comparing the degree-scale signal with channel 150A.

center maps are used. The data far from the source could be contaminated by objects outside the field or could be noise. For RCW38, which is a more extended source, the combined maps were used.

Channel	RCW38		NGC3576	
	1σ	2σ	1σ	2σ
90A	1.24	1.21	0.83	0.92
90B	1.26	1.22	0.87	1.00
150A	1.00	0.96	0.97	0.81
150B	0.97	0.89	0.96	0.80
150A1	1.09	1.06		
150A2	0.98	0.93	1.06	0.92
150B1	1.15	1.10		
150B2	1.07	1.01	1.08	0.96

Table 7.4:
The ratio of source to dipole responsivity for the two galactic sources. The results from integrating to a radius of both 1σ and 2σ are shown.

For the 150 GHz data, the 2σ flux ratio is slightly lower than the 1σ flux ratio when a Gaussian is used to approximate the BOOMERANG beam. This effect is mitigated by convolving the source with the ray-traced beam model (Figure 4.10). The channels with the smaller beams are the most improved. Adding the shoulder to the beam model has less

effect on the 1σ and 2σ values than decreasing the size of the main lobe because the shoulder is at a radius of $\sim 3\sigma$ from the center of the beam. We conclude that the source calibration and the dipole calibration agree at the 15% level in the 150 GHz channels. Larger scale maps of the area and the total flux integrated by MAT would improve this estimate.

At 90 GHz, the NGC3576 BOOMERANG maps are smeared due to pointing uncertainty. The companion object NGC3603 is $23'$ from NGC3576 and due to the larger beams at 90 GHz, the sources overlap somewhat. The B90A and B90B calibrations agree with each other quite well. According to these observations, the 90 GHz dipole calibration is about 15% high. This is possibly due to the small size of the SEST map ($6' \times 6'$) and SEST chop ($11'$) compared with the 90 GHz BOOMERANG beam (about $18'$ FWHM) which would subtract any extended flux.

The extragalactic sources 0537–441 and 0521–365 were also observed with SEST at 150 GHz; the uncertainty in the central flux is about 10%. See Table 7.4 for the results. The SEST and BOOMERANG flux measurements of the extragalactic point source 0521–365 agree to within uncertainties. Evidence was found for variability in 0537–441; data from all BOOMERANG channels imply that the source increased in brightness over the year 1999 by $\sim$40%.

Channel	0521–365	0537–441
90A	0.8	0.5
90B	0.9	0.5
150A	1.0	0.65
150B	1.3	0.65
150A1	0.7	0.65
150A2	1.2	0.65
150B1	1.3	0.5
150B2	1.2	0.6

Table 7.5:
The ratio of dipole to source calibration for the two extragalactic sources. The source 0537–441 appears to have significantly increased in brightness over the year between observations with BOOMERANG and observations with SEST.

7.5 Calibration Stability

The calibration lamp was used to measure the stability of the responsivity throughout the flight. The lamp was turned on for 1 second every 13.4 minutes and provided a transfer calibration standard throughout the flight. Figure 7.7 shows the amplitude of the calibration lamp signal seen in channel 150A. There is a slight drift in responsivity in most channels, which is well modelled by a linear drift, but mostly uncorrelated between channels. Table 7.5 lists the change in responsivity of each channel over the course of the flight. In nearly all channels, the drift is less than 5% over the entire 10.5 day flight.

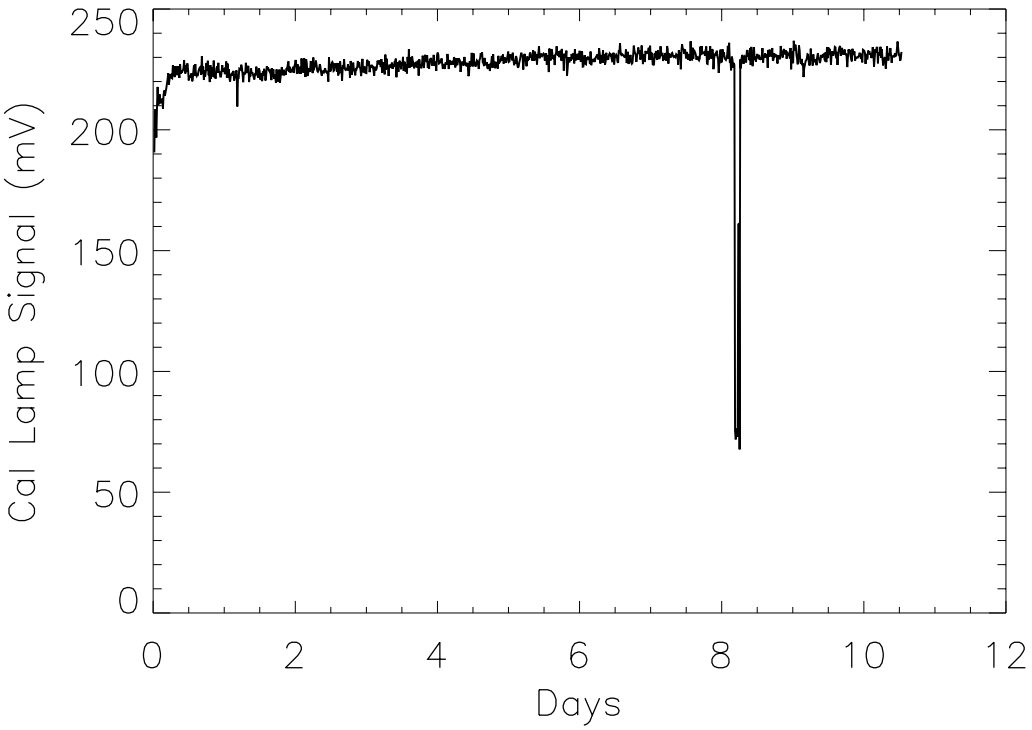

Figure 7.7:
The amplitude of the calibration lamp signal seen by channel B150A during the course of the flight. The rise in responsivity over the first half day of the flight is due to the decrease in background as the balloon ascends. The dip in responsivity on day 8 is due to a brief period of diagnostic tests.

Channel	ΔS
90A	1.59%
90B	1.22%
150A	3.88%
150B	3.4%
150A1	-1.3%
150A2	1.31%
150B1	-5.64%
150B2	-12.1%
240A1	2.29%
240A2	5.10%
240B1	-6.73%
240B2	1.53%
400A1	3.45%
400A2	-3.94%
400B1	1.07%
400B2	3.14%

Table 7.6:
The percent change in responsivity from the beginning to the end of the flight as measured by the drift in the signal due to the calibration lamp.

7.6 Sensitivity

The Noise Equivalent Power (NEP) of each detector is determined by dividing the voltage noise by the electrical responsivity obtained from a current versus voltage load curve measured on the ground (see Section 4.11). The responsivity of the detector is scaled to flight load conditions by the ratio of the bolometer DC voltage measured on the ground to that measured in flight.

The sensitivity of the BOOMERANG receiver to CMB fluctuations is determined by dividing the measured voltage noise by the responsivity to the dipole. The average NEP and NET_{CMB} for each frequency band is listed in Table 7.6.

The optical efficiency of each channel is determined by comparing the predicted responsivity to the CMB dipole to that measured in flight. The predicted responsivity of a channel is given by

$$\frac{dV}{dT} = \frac{dV}{dP} A\Omega \int \frac{dB_\nu(2.7K,\nu)}{dT} t(\nu) d\nu \tag{7.2}$$

where $\frac{dV}{dP}$ is the electrical responsivity measured from the bolometer load curve, $A\Omega$ is the

photometer throughput, $\frac{dB_\nu}{dT}(2.7K, \nu)$ is the spectrum of the CMB dipole, and $t(\nu)$ is the passband of the photometer channel (see Section 4.9). The average optical efficiency for each frequency band is listed in Table 7.6.

Channel	τ (ms)	η_{opt}	NEP (1 Hz) (10^{-17} W/$\sqrt{\text{Hz}}$)	NET_{CMB} (μK$\sqrt{\text{s}}$)
90A	22.5	0.31	3.2	145
90B	21.9	0.30	3.3	137
150A	10.8	0.15	3.4	130
150B	13.3	0.16	3.7	145
150A1	13.3	0.09	4.4	231
150A2	12.0	0.11	3.7	158
150B1	16.3	0.09	3.4	196
150B2	21.2	0.10	3.3	184
240A1	8.9	0.06	5.6	221
240A2	7.2	0.09	5.7	166
240B1	10.5	0.06	5.9	250
240B2	8.8	0.08	25.0	792
400A1	4.1	0.08	39.2	
400A2	9.9	0.05	11.3	
400B1	4.5	0.07	13.3	
400B2	4.3	0.05	11.7	

Table 7.7:
A summary of the in-flight bolometer performance of each channel. Channels 240B2 and 400A1 show the same elevated noise that was seen in the lab noise measurements (Table 4.13).

7.7 Discussion

A summary of the absolute calibration measured from the dipole, the lab calibration, and sources is listed in Table 7.7. We believe the calibration obtained with the dipole to be the most robust and reliable result for the 90 GHz, 150 GHz, and 240 GHz channels, and use it in the subsequent analysis. The source calibration agrees to 15% with the dipole calibration at 90 GHz and 150 GHz.

channel	dipole μV/K$_{CMB}$	lab scaled to flight	NGC3576	RCW38	0521-365
90A	68	54	63	83	54
90B	67	49	67	82	60
150A	76	74	62	69	76
150B	78	75	62	66	101
150A1	49	44		53	34
150A2	67	50	63	62	80
150B1	54	50		62	70
150B2	50	57	49	51	60
240A1	48	43			
240A2	68	47			
240B1	45	39			

Table 7.8:
Absolute responsivity of BOOMERANG measured by the methods discussed above. The dipole calibration is believed to be the most reliable result. The lab calibration scaled to flight is limited by knowledge of the transmission of the NDF. SEST observations of the extended sources NGC3576 and RCW38 are difficult to compare to BOOMERANG, especially at 90 GHz, because of their small chop size. The measurement of the extragalactic source 0521-365 is hampered by poor signal to noise in BOOMERANG.

Chapter 8 Power Spectrum and Cosmological Parameters

The BOOMERANG analysis pipeline is as follows: the raw time stream data are deglitched and the effects of all electronics and bolometer time constants are deconvolved to obtain uniform gain at all frequencies. The attitude of the telescope is reconstructed. A map is made from the time stream data. The angular power spectrum of the map is computed and, finally, cosmological parameters are estimated using the angular power spectrum. These three analysis steps were described in Chapter 2. This chapter discusses analysis details specific to BOOMERANG and the results obtained from the BOOMERANG data set.

8.1 Maps

The iterative map-making scheme described in Chapter 2 was used to create the maps. To pixelize the sky, the HEALPIX nested pixelization scheme is used [25].

Maps made with 90, 150, and 240 GHz data are shown in Figures 8.1, 8.2, and 8.3, respectively. In order to emphasize the degree-scale structure and remove dipole signal, the data are filtered in the time domain with a Gaussian high pass filter that corresponds to an angular scale of 10° on the sky, by applying two different filters to the time domain data, one to the $1^\circ/s$ data and a second with double the cutoff frequency was applied to the $2^\circ/s$ data. This filter has the effect of removing any structure larger than 10° which lies along the scan direction. The maps are then smoothed with a Gaussian spatial filter to a resolution of $20'$. Each of the maps from the three lowest frequency bands shows prominent degree scale structure. The 240 GHz map (Figure 8.3) shows some signal due to dust near the plane of the galaxy.

The BOOMERANG 400 GHz map is shown in Figure 8.4. No degree-scale structure is evident in this map, only signal from galactic dust clouds. A difference map was constructed between the 240 GHz and 150 GHz data (see Figure 8.5). The dominant degree-scale structure disappears in the difference map and the residual structure correlates extremely well with the 400 GHz map. A 90 - 150 GHz difference map shows similar behavior.

The degree scale structure in the maps is therefore presumed to be CMB anisotropy.

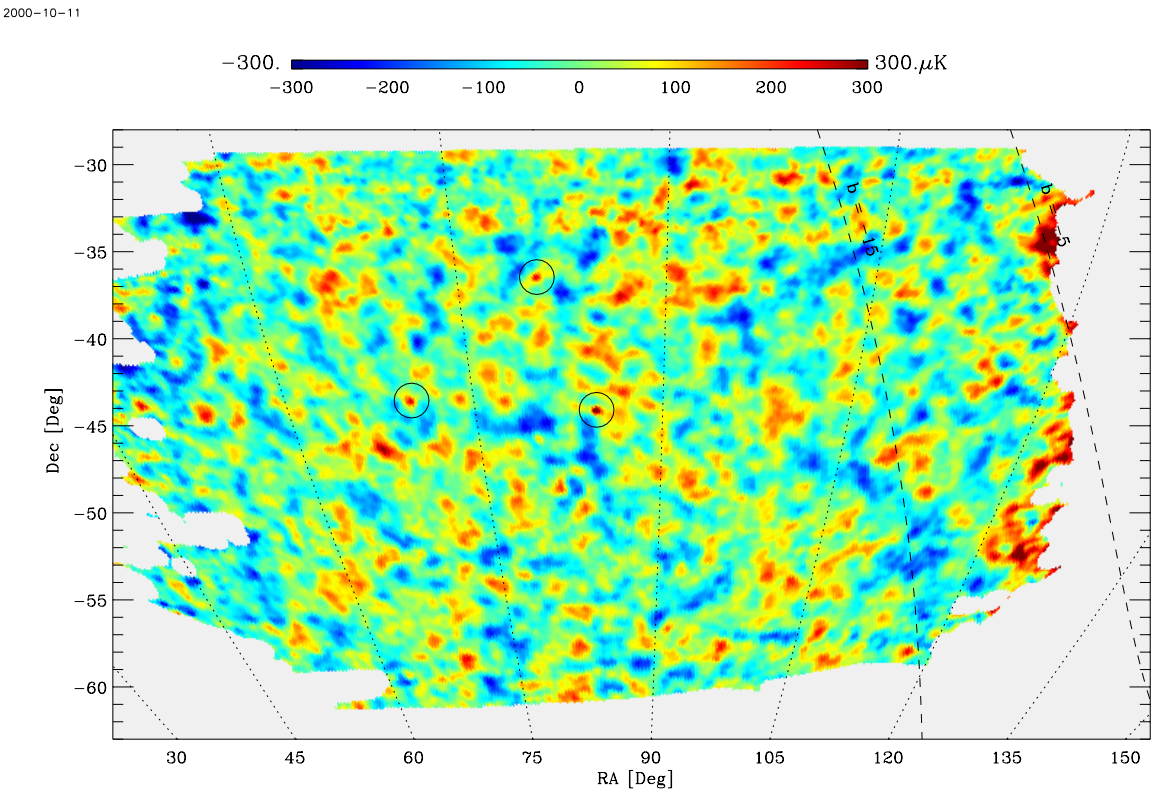

Figure 8.1:
A 90 GHz map made with the data from channel 90A. The three extragalactic point sources are circled and are brightest at this frequency. To produce this map, the data have been filtered in the time domain with a filter corresponding to 10° on the sky, so structures which are larger than 10° along the scan direction are not present in the map. The final map has been smoothed with a 20′ Gaussian filter.

By comparing the relative calibration to the degree scale structure in the maps, the degree scale structure has been shown to have the same spectrum as the dipole to good accuracy (see Chapter 7). The high degree of spatial correlation between the 90, 150, and 240 GHz channels (Figures 8.1, 8.2, and 8.3) and lack of correlation with the 400 GHz channel (Figure 8.4) is also strong evidence that the degree-scale signal has a CMB spectrum.

A color index analysis was performed to quantify the conclusion. Scatter plots were made of the 90 GHz versus 150 GHz and 240 GHz versus 150 GHz for approximately 18,000 pixels which lie at galactic latitude b $<$ -15°. Including the 10% calibration error, the linear fit to these scatter plots yield slopes of 1.00 $\pm$ 0.15 and 1.10 $\pm$ 0.16, respectively. For comparison, free-free emission would produce slopes of 2.3 and 0.85, respectively. Similarly,

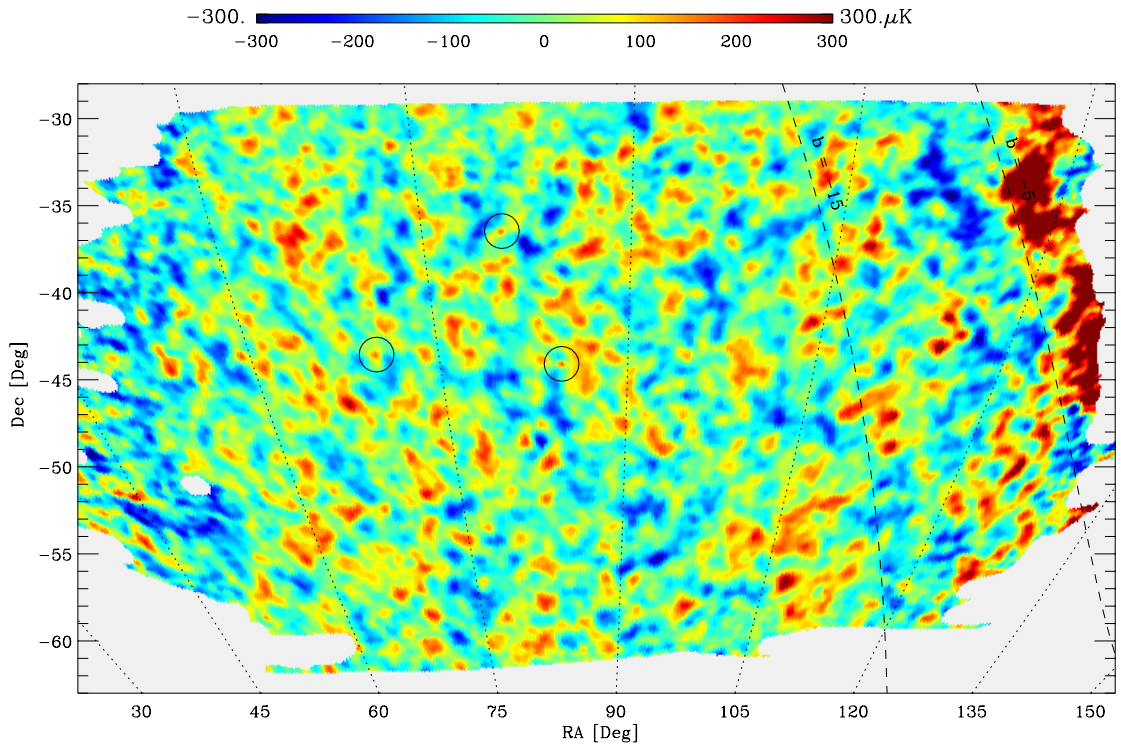

Figure 8.2:
A 150 GHz map made with a combination of channels 150A, 150B1, and 150B2. Time domain and spatial filtering is the same as in the 90 GHz map (Figure 8.1). The galactic signal to the right of the map at b>-5 saturates the color scale, but is confined to the region near the galactic plane.

emission from interstellar dust with temperature 15 K and emissivity spectral index of 1 would produce slopes of 0.4 and 2.9. Therefore, both dust and free-free emission are rejected at $> 99\%$ confidence.

Other known astrophysical foreground sources are not expected to contribute a significant amount of signal to these maps. Galactic synchrotron is expected to be negligible [32]. Additionally, contamination from extragalactic point sources is not expected to be significant [69]. According to an extrapolation of flux from the PMN survey [4], the contribution to the angular power spectrum is $<0.7\%$ at ℓ=200 and $<20\%$ at ℓ=600.

Thermal emission from interstellar dust is the only foreground source which can produce significant signal at 150 GHz. Limits are placed on the level of contamination as follows. We assume that dust properties are similar at high (b< - 20°) and moderate (-20° <b<-5°)

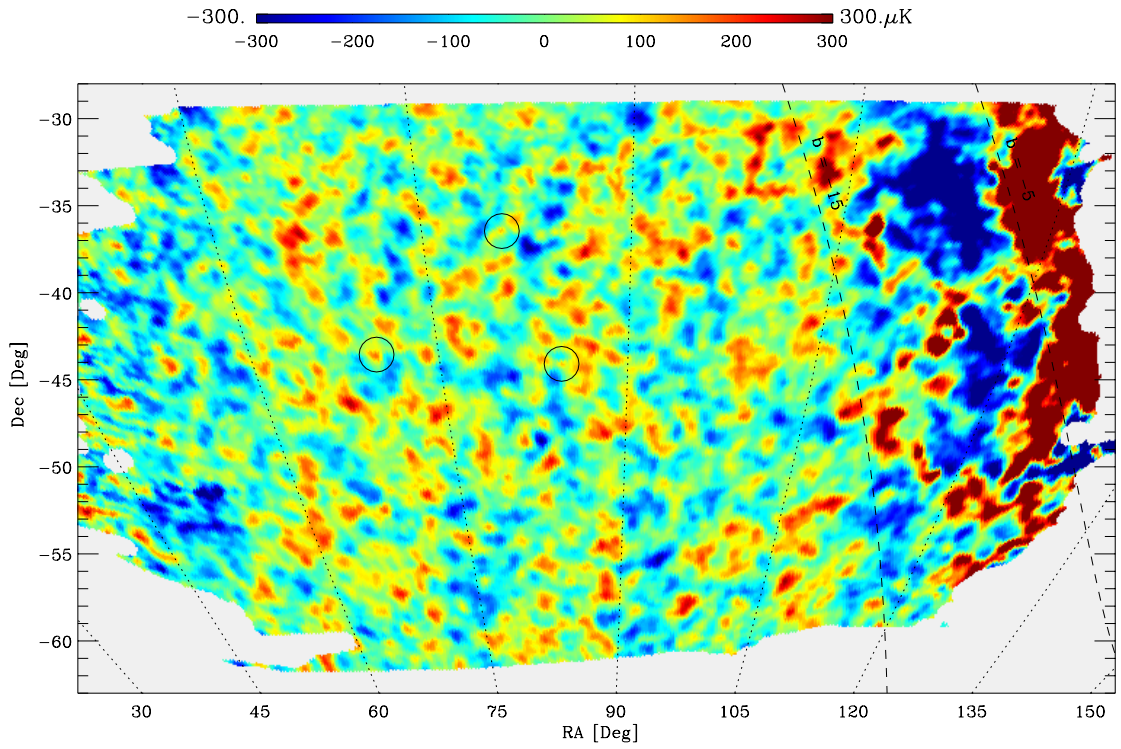

Figure 8.3:
A 240 GHz map made with channels 240A1, 240A2 and 240B1. Time domain and spatial filtering is the same as in the 90 GHz map (Figure 8.1). Note the prominant galactic signal at low galactic latitudes, b>-15. The large gradient at low galactic latitudes is an artifact of the high pass filtering, which sets the average signal at scales larger than 10° equal to zero.

galactic latitudes. The pixels at moderate galactic latitudes are correlated with the 100 μm IRAS/DIRBE map, which is dominated by dust emission. Only the 400 GHz Boomerang map correlates well with the IRAS/DIRBE map. Dust at b < -20° can account for at most 10% of the signal variance at 240 GHz, 3% at 150 GHz, and 0.5% at 90 GHz.

8.2 Power Spectrum

The Boomerang power spectrum of [4] is shown in Figure 8.6. This spectrum is produced using only data from one 150 GHz channel (150A) in the 1°/s scan mode. Additionally, a spatial cut was performed on the data in order to reduce the number of pixels included in the computation. The sky used in the analysis lay in the region of galactic latitude $b <$

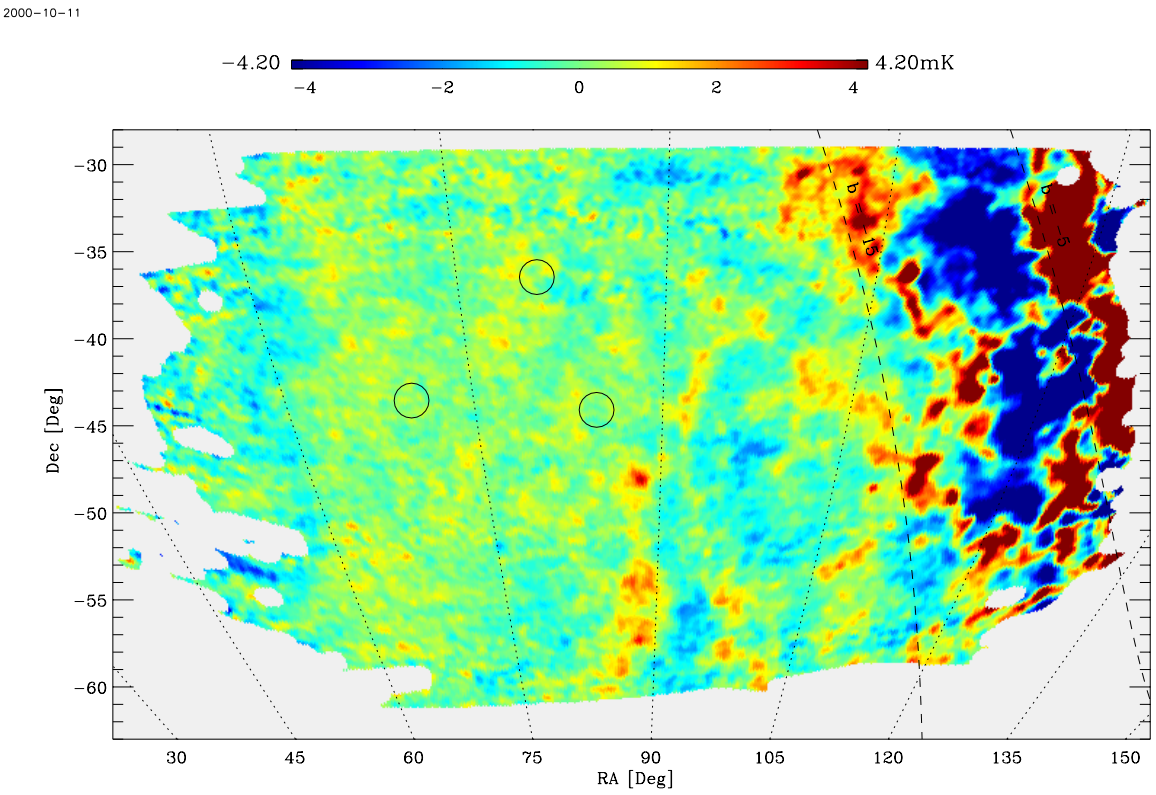

Figure 8.4:
A 400 Ghz map made with data from channel 400B1. No degree scale structure is evident. Low galactic latitude signal (b>-15) is correlated with the structure in the 150 GHz and 240 GHz maps (Figures 8.2 and 8.3), and galactic cirrus is visible at higher galactic latitude. The time domain and spatial filtering of the 400 GHz data is the same as in the 90 GHz map (Figure 8.1).

-20°, right ascension $\alpha > 70°$ and declination -55° $< \delta <$ -35 °. Additionally the sky was pixelized at $14'$ resolution, again to reduce the computation time required. The resulting data set consists of about 8,000 pixels.

The resulting power spectrum must be corrected by the window function of the experiment, including the beam and the pixelization. Figure 8.7 shows the contribution to the window function of each of these components.

Because the beam shape was not measured at high signal-to-noise in flight (Section 6.6), the beam used to calculate the window function is a combination of the ray-trace model, observations of the tethered source, and in-flight pointing jitter. The ray-trace model is fit to the tethered source data and is widened by the jitter of $4'$ rms.

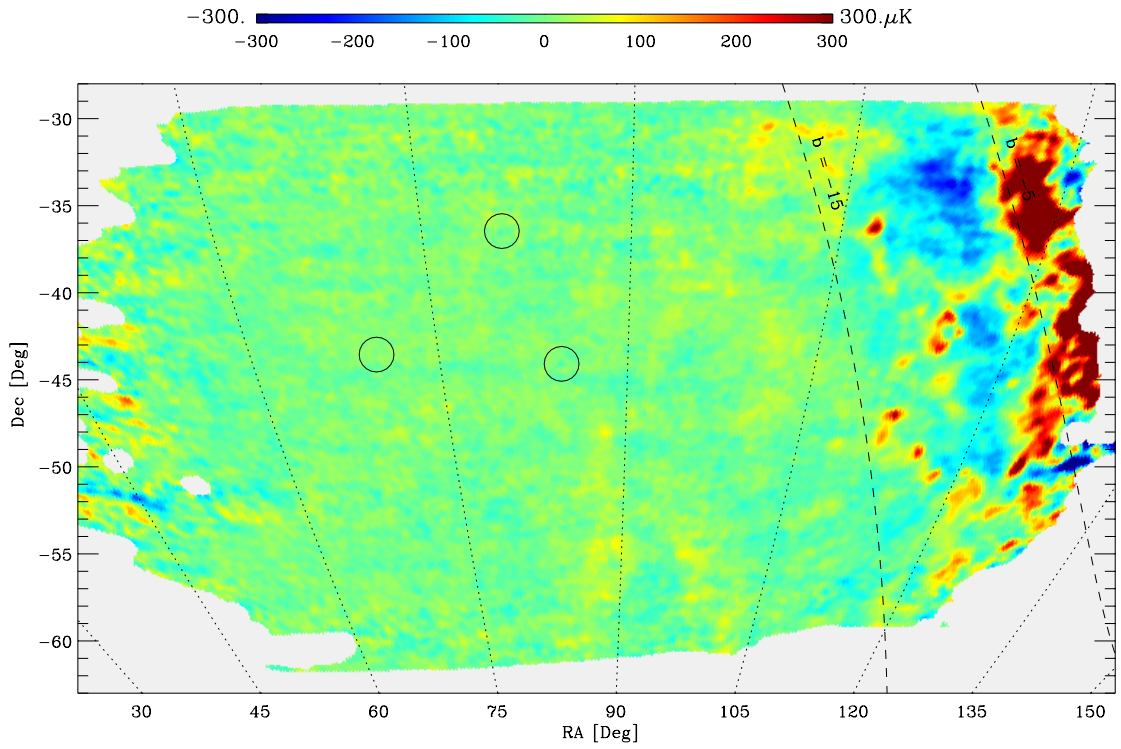

Figure 8.5:
The difference between the proceeding 240 GHz and 150 GHz maps from Figures 8.2 and 8.3. No degree scale structure remains, and there is a strong correlation with the 400 GHz map (Figure 8.4).

The uncertainty in the power spectrum due to uncertainty in the beam amounts to the possibility that the spectrum could be tilted slightly (within the error bars shown in Figure 8.7). The error in the beam is carried over into the cosmological analysis.

A localized peak is seen at $\ell \sim 200$. According to standard cold dark matter (CDM) models of structure formation, more peaks should be seen at higher harmonics. However, the result in Figure 8.6 shows no features at smaller angular scale. This has interesting implications for the determination of cosmological parameters, as shown below.

A systematics test was done by producing a power spectrum of a difference map. The second half of the data was weighted negatively relative to the first, producing a map which should contain no signal if the signal is repeatable on the sky between the first and second halves of the data. Between the first and second halves of the data, the payload has traveled

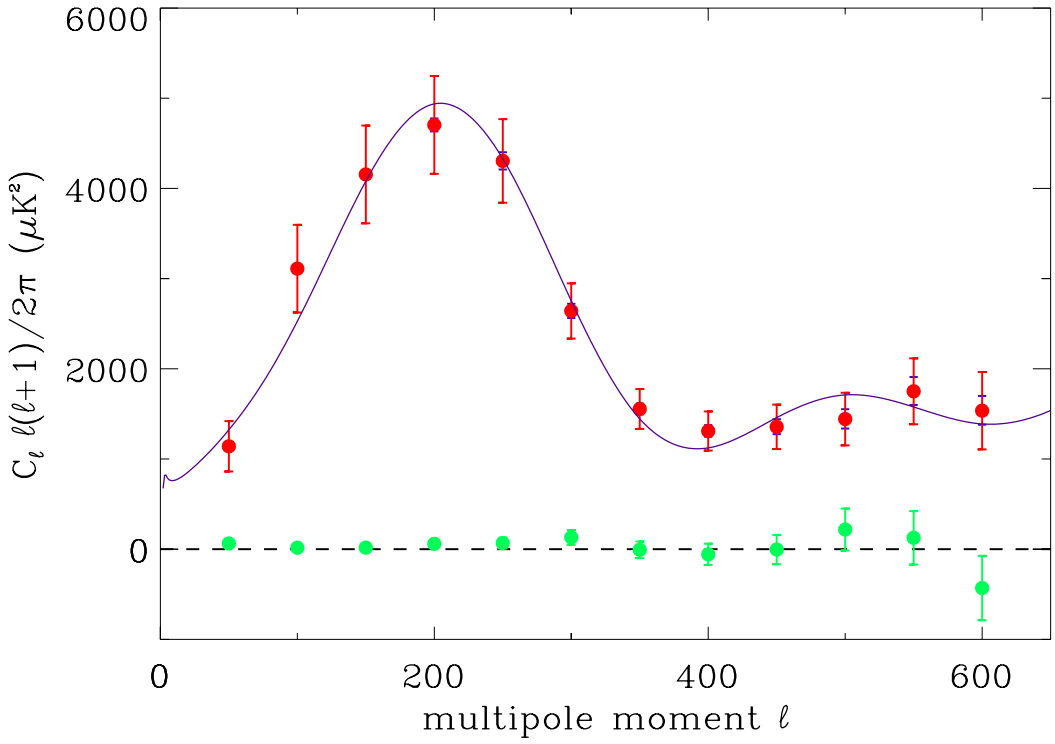

Figure 8.6:
The angular power spectrum of the CMB as measured by BOOMERANG [4]. The red data points are the sum and the green data points are the difference of the jackknife test. The purple solid curve is a best fit model with parameters Ω_{tot} =1.15, $\Omega_b h^2 = 0.03$, $\Omega_{cdm} h^2$ =0.17, Ω_Λ =0.4, and n_s =0.925. The light purple error bars indicate the error in each bin due to the uncertainty in the beam. The 10% calibration error is not shown. The tiny error bars on the green data points at $\ell < 400$ show that the errors near the first acoustic peak are dominated by cosmic variance. A small fraction of the BOOMERANG dataset (roughly 5%) was used to produce this result. The inclusion of more pixels in the analysis will reduce the cosmic sample variance, which will reduce the errors at lower multipole. The inclusion of more channels and more of the time-series data in each channel will reduce the noise at high multipole, which is dominated by instrument noise.

several hundred kilometers and the Sun has moved around 2° on the sky. The green data points in Figure 8.6 show the difference power spectrum. The reduced χ^2 of this power spectrum is 1.11 with 12 degrees of freedom, consistent with zero signal.

The most surprising feature of this power spectrum is lower power at smaller angular scales. A mismeasurement of the window function of the experiment could easily result in a change in the ratio of the first peak to the plateau seen at higher ℓ, perhaps suppressing a second acoustic peak. The window function could be changed by the contribution of

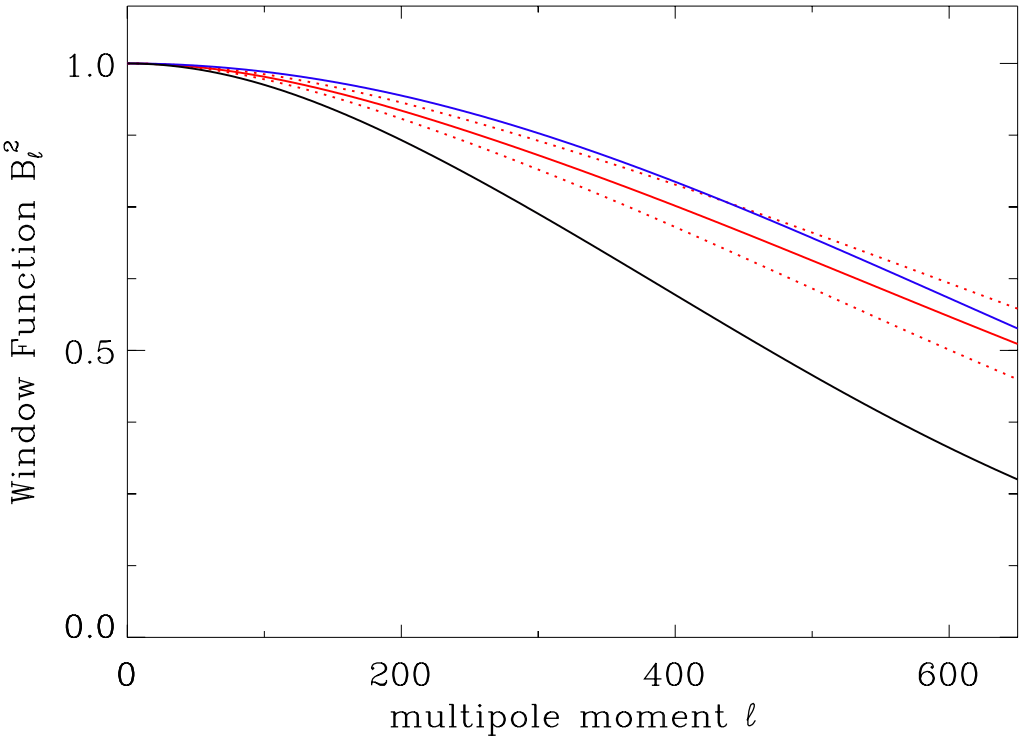

Figure 8.7:
Contributions to the BOOMERANG window function for channel 150A. The black line shows the total window function. The blue line is the contribution due to the $14'$ pixelization. The red line shows the window function due to the $10.5'$ effective beam (including pointing jitter), and is enclosed by dashed red lines which indicate the upper and lower 1σ limits of the uncertainty in the window function due to uncertainty in the beam.

sidelobes.

To investigate this possibility, a conservative model of the sidelobes was constructed from the tethered source data. The model chosen was the sum of two Gaussians; the first is the nominal beam (with $9.7'$ FWHM) and the second was chosen to enclose all of the sidelobes with a $60'$ FWHM normalized to 12% of the peak of the first Gaussian. Figure 8.8 compares the model to the tethered source data.

The window functions resulting from these models are shown in Figure 8.9. To estimate the effect a conservative beam would have on the BOOMERANG power spectrum, the ratio of the two window functions was computed at $\ell = 200$ and at ℓ =550. It was found that the ratio of the power at the two multipole moments would change by 9% if a correction due to a conservative beam was necessary. However, as seen in Figure 8.7, the error in the window

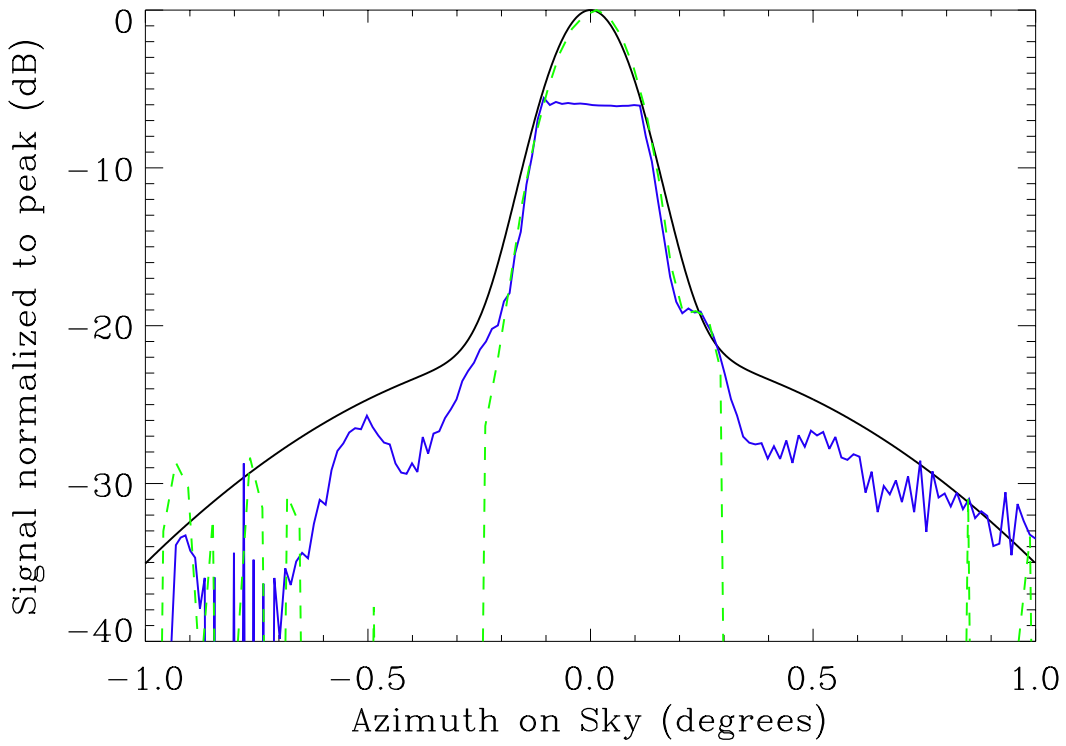

Figure 8.8:
The conservative beam model constructed as the sum of two Gaussians. The solid blue and dotted green lines show the data from the large and small tethered sources, respectively. The solid black curve shows the conservative model, which includes the best fit Gaussian plus a second Gaussian of 60′ FWHM, normalized to 12% at the peak of the first.

function due to uncertainty in the beam is already 9% at $\ell = 550$. Therefore, sidelobes smaller than or equal to the conservative beam model would not affect the resulting power spectrum any more than error in the window function due to beam width uncertainty.

8.3 Cosmological Parameter Estimation

The presence of a localized acoustic peak at $\ell \sim 200$ strengthens the evidence for the Cold Dark Matter (CDM) models of structure formation. The major rival theory, topological defects, predicts a broader peak due to the decoherence of textures [54] or cosmic strings [18]. We therefore restrict our analysis to the CDM paradigm.

The other interesting feature of the BOOMERANG power spectrum, besides the presence of the localized peak, is the absence of any features at higher ℓ. Heuristically, we expect

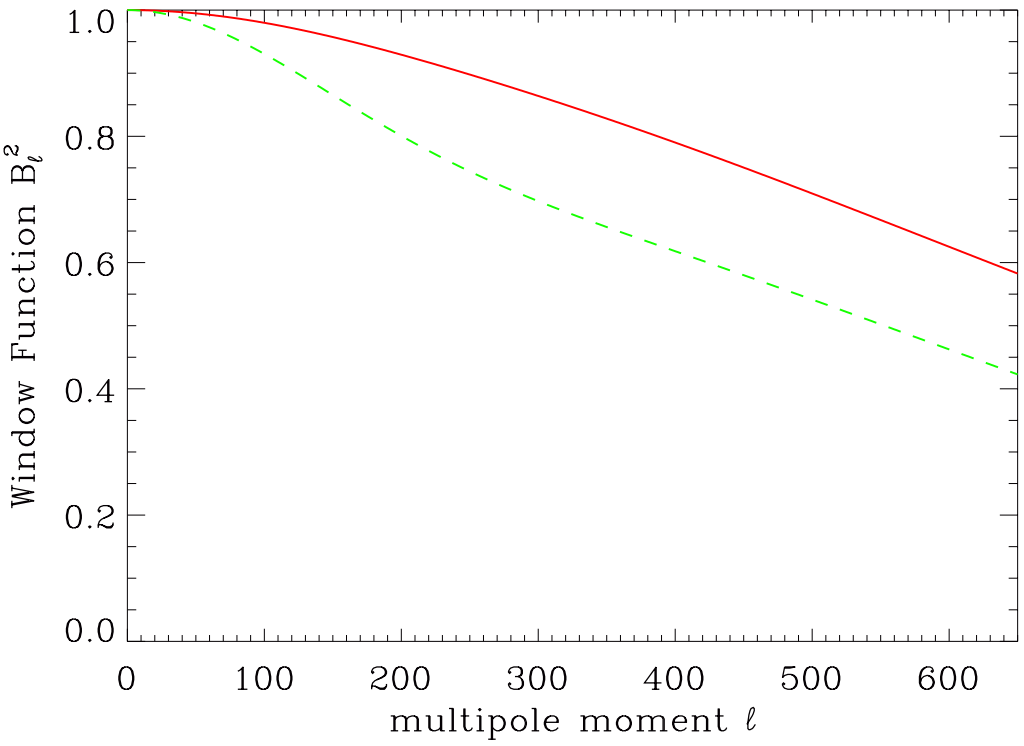

Figure 8.9:
The window function from the ZEMAX model beam (solid red line) and the conservative beam model of Figure 8.8 (dashed green line).

this to be evidence for a high baryon density. The odd acoustic peaks (numbers 1,3,5, etc., in order of decreasing angular scale) in the power spectrum correspond to compressions in the photon/baryon plasma in the early universe, while the even peaks (numbers 2,4,6, etc., in order of decreasing angular scale) correspond to rarefactions. The ratio of power in neighboring peaks therefore shows the balance between compressions and rarefactions. As seen in the measured power spectrum, a suppressed second peak relative to a first peak indicates that compressions are favored over rarefactions. One mechanism that can favor compressions is a high baryon content to the Universe.

8.3.1 Choice of Parameters

Within the framework of CDM cosmological models, a set of parameters can be constrained using the measured C_ℓ. Reasonable ranges of parameters are chosen, and theoretical angular power spectra are generated for a discrete grid of these parameters. The likelihood of the

data are computed for each theoretical power spectrum, and the entire space is mapped out, finding the maximum likelihood model. For the analysis of the BOOMERANG dataset, a seven-parameter space is chosen to characterize a broad range of CDM models: ω_b, ω_c, Ω_{tot}, Ω_Λ, n_s, τ_C, and $\ln C_{10}$.

Each density parameter denoted by a capital Ω is in units of the "critical" density [53]:

$$\Omega_i = \frac{\rho_i}{\rho_{crit}} \tag{8.1}$$

where

$$\rho_{crit} = \frac{3H_0^2}{8\pi G} \tag{8.2}$$

The first two parameters describe the behavior of acoustic oscillations in the early universe. The energy density of baryons, $\omega_b = \Omega_b h^2$, and the energy density of cold dark matter, $\omega_c = \Omega_c h^2$, affect the sound-crossing distance at the time of recombination, r_s.

The total energy density, Ω_{tot}, which parameterizes the geometry of the universe, affects the angle-diameter distance to the surface of last scattering. In open models, where $\Omega_{tot} < 1$, r_s is mapped to smaller angular scales; conversely where $\Omega_{tot} > 1$, r_s is mapped to larger angular scales. This affects the positions of the acoustic peaks in the angular power spectrum.

Energy density due to matter and energy density due to cosmological constant affect the geometry similarly; therefore, combinations of Ω_Λ and Ω_m which give the same angular diameter distance give very similar angular power spectra, resulting in a degeneracy. The main implication of this degeneracy is that BOOMERANG alone cannot measure Ω_Λ.

The Gunn-Peterson test concludes from the lack of neutral hydrogen absorption lines in high-redshift quasar spectra that the universe reionized sometime between z $\sim$ 5 and the time of recombination [27]. This suppresses small scale C_ℓ by a factor of $e^{-2\tau_C}$, where τ_C is the optical depth of plasma between recombination and the present.

The final parameters, the spectral index of scalar fluctuations n_s and the normalization C_{10}, are set by the spectrum of primordial fluctuations due to inflation. Most inflationary models have a scale-invariant spectrum of fluctuations where $n_s = 1$. The normalization parameter C_{10} is in units which fixes the CMB power in the theoretical spectrum at $\ell = 10$. This parameter is used to account for calibration error in the measured angular power spectrum.

The parameter C_{10} is a continuous variable, but all of the other parameters are discretized. See Table 8.3.1 for a list of the range of parameters. A database of C_ℓ values for each of the models was constructed using the CMBFAST [62] and CAMB [36] software packages.

parameter	lower limit	upper limit	number of steps
ω_b	0.0031	0.2	14
ω_c	0.03	0.8	10
Ω_{tot}	0.1	1.5	15
Ω_Λ	0	1.1	11
n_s	0.5	1.5	31
τ_C	0	0.5	9

Table 8.1:
The span of CDM parameters considered in the analysis.

8.3.2 Results

Table 8.3.2 shows the maximum likelihood parameters for all of the priors considered. The first search through the database was done with no prior assumptions (P1). This yields a slightly closed ($\Omega = 1.31 \pm 0.16$) Universe. The location of the acoustic peak near $\ell = 200$ requires a low sound speed to compensate the closed geometry. A low sound speed results in a very high value of $H_0 = 108 \pm 39$ km/s/Mpc and of $\Omega_b h^2 = 0.100^{+0.031}_{-0.043}$, and a very low age of 7.8 $\pm$ 2.9 Gyr. The best fit power spectrum is shown as the dotted black line in Figure 8.10.

A wide range of priors were subsequently used to further constrain the data. "Weak" priors applied were conservative constraints on the Hubble constant ($0.45 < h < 0.9$) and the baryon density ($\Omega_b h^2 < 0.038$) from Big Bang Nucleosynthesis (BBN), as well as the generally agreed upon assumption that the age of the universe is greater than 10 Gyr (P2-P4). "Strong priors" considered were $h = 0.71 \pm 0.08$ from the HST Key project [23] [49] and $\Omega_b h^2 = 0.019 \pm 0.002$ [51] [71]. Additionally, constraints from large scale structure measurements [8] and prior measurements of the CMB angular power spectrum were considered [3] [9] [44] [48].

Application of the weak priors (P4) moves the best fit model closer to a flat universe with $\Omega = 1.15^{+0.10}_{-0.09}$. The resulting value of $\Omega_b h^2 = 0.036 \pm 0.05$ is much closer to, but

still in disagreement with the BBN-derived values of [51] and [71]. Hubble's constant is determined to be $h = 0.58 \pm 0.1$, which agrees with HST measurements [23]. Values for other parameters are also reasonable, with $n_s = 1.04 \pm 0.1$, $\Omega_\Lambda < 0.83$, $\tau_C = 0.21^{+0.19}_{-0.15}$, $\Omega_{matter} = 0.84 \pm 0.29$ and Age $= 13.4 \pm 1.9$ Gyr. There is no clear detection of reionization or of Λ. Including prior CMB measurements (P4a) does not change these results by a significant amount.

Including large scale structure measurements (P5) does little to affect the values of Ω, $\Omega_b h^2$, τ_C, and n_s. One degeneracy is broken, however, and a clear detection of Λ is made; $\Omega_\Lambda = 0.66^{+0.07}_{-0.09}$. This result is consistent with "cosmic concordance" models.

The strong constraint on Hubble's constant (P6) gives results closely similar to those using the weak prior. However, the strong constraint on Ω_b (P7) shifts the results considerably. Without the strong constraint, the BOOMERANG data yield a high value of Ω_b, and forcing it to be low requires compensation in other parameters. The parameters which are most affected are $\Omega_\Lambda = 0.79^{+0.08}_{-0.30}$ and $\Omega_m = 0.71 \pm 0.27$.

Further evidence of the implication of a high density of baryons is shown by forcing a flat universe (P10,P11,P13). In this case, the value of $\Omega_b h^2$ is driven much higher than the BBN-favored value, back to $0.032^{+0.004}_{-0.003}$. Including SN1A results [56] as a prior (P12) does not change the results very much.

The best fit power spectra that result from the application of these priors are highly degenerate over the range of angular scales measured by BOOMERANG (Figure 8.10). Prior assumptions about the parameter space from other cosmological measurements are essential for breaking this degeneracy. It is also apparent that the models diverge strongly at $\ell > 600$, however. A measurement of the power spectrum at higher ℓ can easily distinguish between these models and make a more precise measurement of cosmological power spectrum with fewer priors. An improved attitude reconstruction of the BOOMERANG dataset will allow measurement of the spectrum at higher ℓ, as will measurements at higher ℓ from experiments such as CBI.

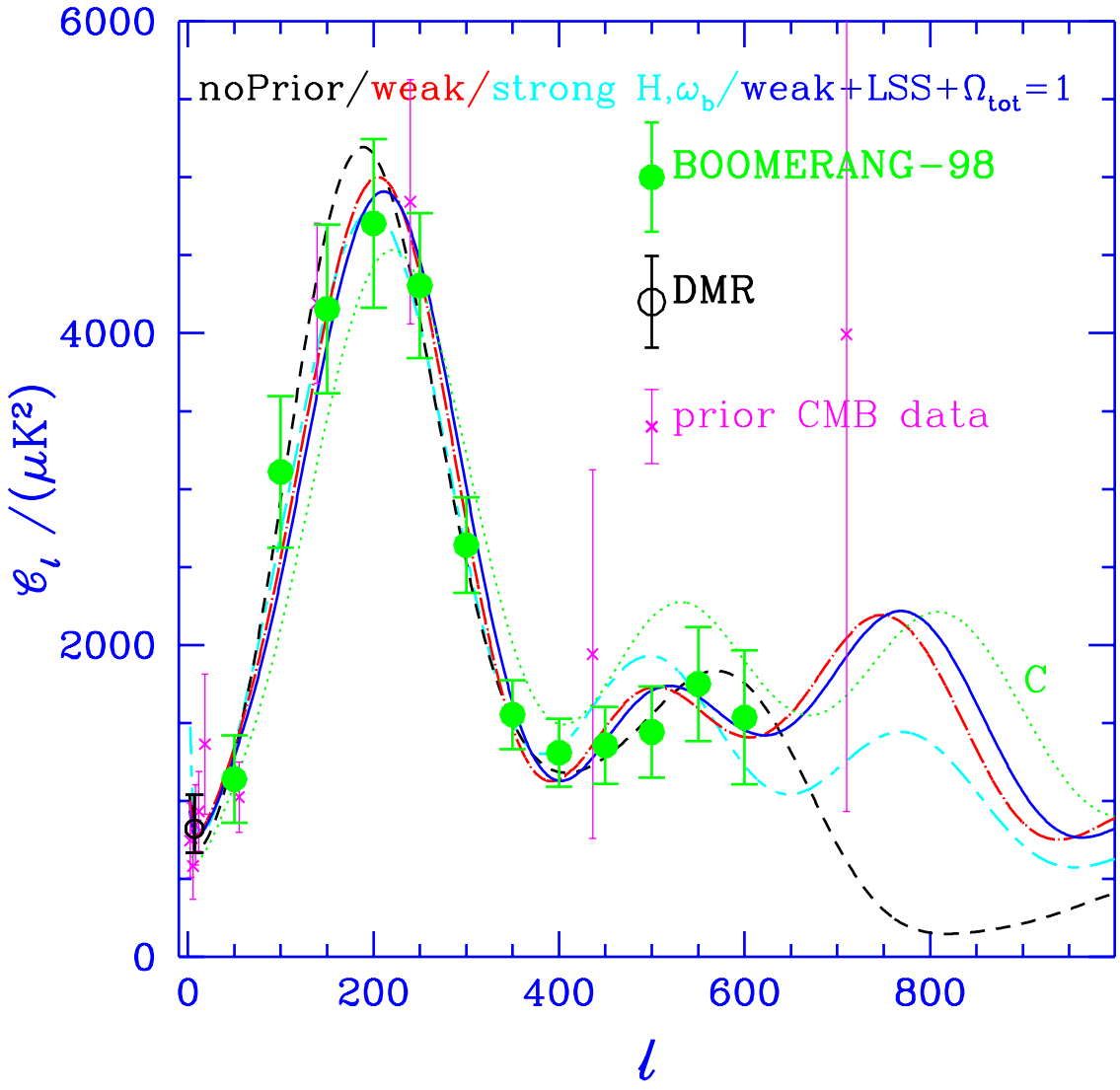

Figure 8.10:
The best fit model power spectra. The green data points are from the BOOMERANG power spectrum. The magenta data points are binned prior CMB measurements. The smooth curves are best fit power spectra corresponding to the priors listed in Table 8.3.2 as follows: short dashed line is P1, dot-dashed line is P4, short-long dashed line is P8, and solid line is P11. The curve labeled "C" corresponds to the "concordance" model with parameters $\Omega = 1.0$, $\Omega_b h^2 = 0.02$, $\Omega_{cdm} h^2 = 0.12$, and $\Omega_\Lambda = 0.7$. The concordance model does not fit the data well.

Priors	Ω_{tot}	$\Omega_b h^2$	n_s	Ω_b	Ω_Λ
P0: Medium h+BBN	$1.07^{0.06}_{0.06}$	$0.030^{0.004}_{0.004}$	$1.00^{0.08}_{0.08}$	$0.08^{0.02}_{0.02}$	$0.37^{0.23}_{0.23}$
P1: Whole Database	$1.31^{...}_{0.16}$	$0.100^{0.031}_{0.043}$	$0.88^{0.12}_{0.09}$	$0.10^{0.05}_{0.05}$	$0.53^{0.22}_{0.27}$
P2: Weak h ($0.45 < h < 0.90$)+age	$1.15^{0.10}_{0.09}$	$0.036^{0.006}_{0.005}$	$1.04^{0.10}_{0.09}$	$0.11^{0.04}_{0.04}$	< 0.83
P3: Weak BBN ($\Omega_b h^2 \leq 0.05$)+age	$1.16^{0.10}_{0.10}$	$0.035^{0.006}_{0.006}$	$1.03^{0.10}_{0.10}$	$0.16^{0.09}_{0.09}$	< 0.83
P4: Weak h+BBN+age	$1.15^{0.10}_{0.09}$	$0.036^{0.005}_{0.005}$	$1.04^{0.10}_{0.09}$	$0.11^{0.04}_{0.04}$	< 0.83
P4a: Weak and prior CMB	$1.01^{0.09}_{0.09}$	$0.031^{0.007}_{0.006}$	$1.06^{0.10}_{0.09}$	$0.10^{0.04}_{0.04}$	< 0.79
P4b NO B98: Weak and prior CMB	$1.03^{0.12}_{0.10}$	$0.024^{0.017}_{0.018}$	$1.14^{0.12}_{0.13}$	$0.08^{0.06}_{0.06}$	< 0.80
P5: LSS & Weak h+BBN+age	$1.12^{0.07}_{0.07}$	$0.034^{0.006}_{0.005}$	$0.99^{0.10}_{0.08}$	$0.10^{0.04}_{0.04}$	$0.66^{0.07}_{0.09}$
P5a: LSS & Weak and prior CMB	$1.02^{0.09}_{0.08}$	$0.030^{0.007}_{0.006}$	$1.05^{0.10}_{0.08}$	$0.09^{0.04}_{0.04}$	$0.47^{0.18}_{0.22}$
P5b NO B98: LSS & Weak and CMB	$1.00^{0.07}_{0.07}$	$0.028^{0.015}_{0.015}$	$1.08^{0.11}_{0.11}$	$0.08^{0.06}_{0.06}$	$0.58^{0.13}_{0.17}$
P6: Strong h ($h = 0.71 \pm 0.08$)	$1.09^{0.07}_{0.06}$	$0.036^{0.005}_{0.005}$	$1.05^{0.09}_{0.09}$	$0.08^{0.03}_{0.03}$	< 0.82
P7: Strong BBN ($\Omega_b h^2$=0.019 $\pm$ 0.002)	$1.10^{0.05}_{0.05}$	$0.021^{0.003}_{0.002}$	$0.85^{0.08}_{0.07}$	$0.07^{0.02}_{0.02}$	$0.79^{0.08}_{0.30}$
P8: Strong h+BBN	$1.04^{0.04}_{0.04}$	$0.021^{0.003}_{0.002}$	$0.87^{0.07}_{0.07}$	$0.05^{0.02}_{0.02}$	$0.75^{0.14}_{0.25}$
P9: LSS & Strong h+BBN	$1.04^{0.05}_{0.04}$	$0.022^{0.003}_{0.002}$	$0.92^{0.06}_{0.06}$	$0.05^{0.02}_{0.02}$	$0.66^{0.05}_{0.07}$
P10: $\Omega_{\rm tot} = 1$ & Weak h+age	1	$0.031^{0.004}_{0.004}$	$0.99^{0.07}_{0.07}$	$0.06^{0.02}_{0.02}$	< 0.78
P11: $\Omega_{\rm tot} = 1$ & LSS & Weak	1	$0.030^{0.004}_{0.004}$	$0.96^{0.07}_{0.06}$	$0.05^{0.01}_{0.01}$	$0.67^{0.04}_{0.06}$
P12: LSS & Weak & SN1a	$1.08^{0.05}_{0.05}$	$0.034^{0.005}_{0.004}$	$1.02^{0.09}_{0.08}$	$0.08^{0.03}_{0.03}$	$0.72^{0.05}_{0.04}$
P13: $\Omega_{\rm tot} = 1$ & LSS & Weak & SN1a	1	$0.030^{0.003}_{0.004}$	$0.97^{0.07}_{0.06}$	$0.05^{0.01}_{0.01}$	$0.69^{0.02}_{0.04}$

Priors	τ_c	$\Omega_{cdm} h^2$	Ω_m	h	Age
P0 : Medium h+BBN	$0.12^{0.16}_{0.09}$	$0.25^{0.10}_{0.09}$	$0.72^{0.23}_{0.23}$	$0.63^{0.06}_{0.06}$	$11.9^{1.6}_{1.6}$
P1 : Whole Database	$0.22^{0.19}_{0.16}$	...	$0.81^{0.34}_{0.34}$	$1.08^{0.39}_{0.39}$	$7.8^{2.9}_{2.9}$
P2: Weak h ($0.45 < h < 0.90$)+age	$0.21^{0.19}_{0.15}$	$0.24^{0.08}_{0.09}$	$0.84^{0.29}_{0.29}$	$0.58^{0.10}_{0.10}$	$12.7^{2.1}_{2.1}$
P3 : Weak BBN ($\Omega_b h^2 \leq 0.05$)+age	$0.21^{0.19}_{0.15}$	$0.19^{0.10}_{0.09}$	$0.92^{0.33}_{0.33}$	$0.52^{0.14}_{0.14}$	$14.6^{3.9}_{3.9}$
P4: Weak h+BBN+age	$0.21^{0.19}_{0.15}$	$0.24^{0.08}_{0.09}$	$0.84^{0.29}_{0.29}$	$0.58^{0.10}_{0.10}$	$12.7^{2.1}_{2.1}$
P4a: Weak and prior CMB	$0.24^{0.19}_{0.17}$	$0.18^{0.07}_{0.06}$	$0.64^{0.23}_{0.23}$	$0.59^{0.11}_{0.11}$	$13.4^{1.9}_{1.9}$
P4b: NO B98: Weak and prior CMB	$0.29^{0.16}_{0.19}$	$0.21^{0.09}_{0.08}$	$0.71^{0.28}_{0.28}$	$0.60^{0.11}_{0.11}$	$12.9^{2.0}_{2.0}$
P5: LSS & Weak h+BBN+age	$0.19^{0.21}_{0.14}$	$0.14^{0.03}_{0.02}$	$0.48^{0.13}_{0.13}$	$0.60^{0.11}_{0.11}$	$14.5^{1.6}_{1.6}$
P5a: LSS & Weak and prior CMB	$0.22^{0.19}_{0.16}$	$0.16^{0.05}_{0.04}$	$0.57^{0.20}_{0.20}$	$0.60^{0.12}_{0.12}$	$13.8^{1.7}_{1.7}$
P5bNO B98: LSS & Weak and CMB	$0.26^{0.17}_{0.18}$	$0.14^{0.04}_{0.03}$	$0.44^{0.15}_{0.15}$	$0.63^{0.12}_{0.12}$	$13.8^{1.7}_{1.7}$
P6: Strong h ($h = 0.71 \pm 0.08$)	$0.20^{0.19}_{0.15}$	$0.26^{0.08}_{0.10}$	$0.71^{0.27}_{0.27}$	$0.66^{0.07}_{0.07}$	$11.6^{1.4}_{1.4}$
P7: Strong BBN ($\Omega_b h^2$=0.019 $\pm$ 0.002)	$0.09^{0.12}_{0.07}$	$0.08^{0.07}_{0.03}$	$0.38^{0.21}_{0.21}$	$0.54^{0.10}_{0.10}$	$17.7^{2.9}_{2.9}$
P8: Strong h+BBN	$0.08^{0.12}_{0.06}$	$0.09^{0.09}_{0.03}$	$0.28^{0.19}_{0.19}$	$0.68^{0.09}_{0.09}$	$15.2^{2.2}_{2.2}$
P9: LSS & Strong h+BBN	$0.08^{0.12}_{0.06}$	$0.14^{0.03}_{0.02}$	$0.39^{0.07}_{0.07}$	$0.64^{0.08}_{0.08}$	$14.0^{1.3}_{1.3}$
P10: $\Omega_{\rm tot} = 1$ & Weak h+age	$0.10^{0.13}_{0.07}$	$0.27^{0.05}_{0.07}$	$0.57^{0.21}_{0.21}$	$0.74^{0.09}_{0.09}$	$10.9^{0.8}_{0.8}$
P11: $\Omega_{\rm tot} = 1$ & LSS & Weak	$0.09^{0.12}_{0.07}$	$0.18^{0.02}_{0.02}$	$0.32^{0.05}_{0.05}$	$0.79^{0.05}_{0.05}$	$11.7^{0.4}_{0.4}$
P12: LSS & Weak & SN1a	$0.23^{0.19}_{0.17}$	$0.15^{0.03}_{0.03}$	$0.37^{0.07}_{0.07}$	$0.70^{0.09}_{0.09}$	$13.3^{1.3}_{1.3}$
P13: $\Omega_{\rm tot} = 1$ & LSS & Weak & SN1a	$0.10^{0.12}_{0.07}$	$0.18^{0.02}_{0.01}$	$0.31^{0.03}_{0.03}$	$0.81^{0.03}_{0.03}$	$11.6^{0.3}_{0.3}$

Table 8.2:
Parameter estimates from the BOOMERANG power spectrum using a range of priors.

Chapter 9 Other Science with BOOMERANG

BOOMERANG has produced deep maps of a large region of the sky at 90, 150, 240, and 400 GHz. There are many possibilities for doing other science using this existing BOOMERANG data set. These include studying galactic foreground sources and looking for high-redshift objects such as clusters and galaxies.

9.1 Galactic Dust

The 400 GHz maps produced by BOOMERANG are of interest for the study of galactic dust, both as a foreground contaminant for future CMB measurements or as astrophysics in its own right.

The BOOMERANG data can be compared with existing maps [63] and models of dust [21]. There is a strong degree of correlation between the BOOMERANG 400 GHz data and the IRAS/DIRBE maps of [63]. A preliminary analysis of the models in [21] using BOOMERANG data shows better consistency with a dual component model than with a single component model of dust [67] [39].

9.2 Sunyaev-Zel'dovich Effect in Clusters

The ionized gas in clusters produces a measurable distortion of the spectrum of the CMB viewed through a cluster (Sunyaev-Zel'dovich, or S-Z, effect) [66]. There are two components of these effects, corresponding to two different components of the velocity of the electrons in the intra-cluster plasma. The thermal component is due to the thermal motion of the electrons in the ionized gas, and the kinematic effect is due to the bulk motion of the cluster relative to the CMB. Each of these effects has a distinct spectral shape and their brightnesses add linearly (see Figure 9.1).

Measuring the amplitude of the kinematic S-Z effect in a sample of clusters gives bulk velocity measurements. Measuring the amplitude of the thermal S-Z effect and combining the measurement of an X-ray map of the cluster leads to a model of the cluster geometry, and a physical size of the cluster. The size and angular extent can be related to obtain a

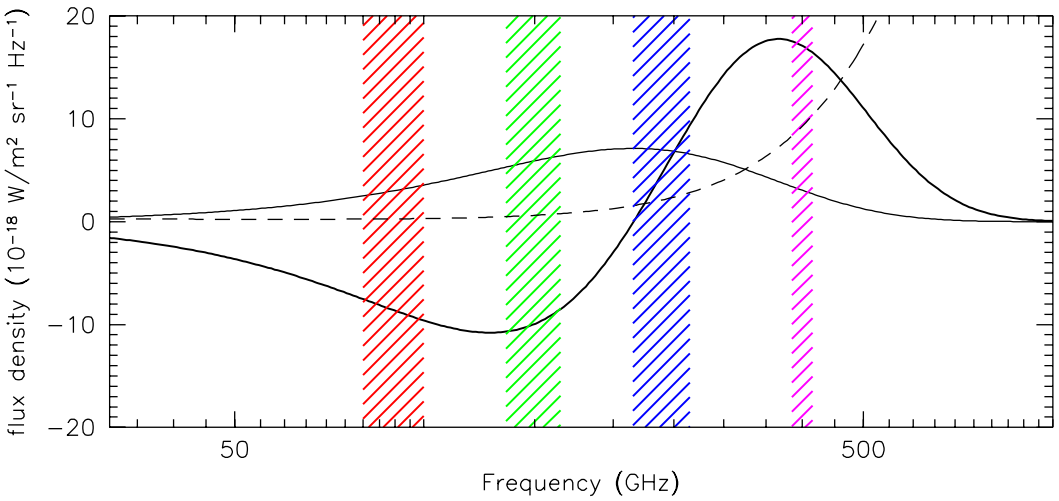

Figure 9.1:
The spectrum of the Sunyaev-Zel'dovich effect. The hatched lines indicate the BOOMERANG bandpasses. The solid line indicates the thermal S-Z effect, the dashed line shows the spectrum of CMB anisotropy, and the dotted line indicates the spectrum of dust. These three signals are readily separable using the four BOOMERANG bands.

physical distance, thereby measuring Hubble's constant. This has been successfully done by several groups; however, selection effects make it desirable to measure the thermal S-Z effect in an unbiased sample of clusters.

The beam size of BOOMERANG is $10'$, which is much larger than most clusters, so the signal due to the S-Z effect will be heavily diluted. Certain large or bright clusters may be detectable, however. BOOMERANG made targeted observations of three clusters: A3158, A3226, and A3112. The data have not yet been fully reduced, but there is hope of detecting the thermal S-Z effect in these three targets.

9.3 Serendipitous Cluster Searches

The rate of cluster formation in the early universe strongly depends on the value of the energy density of the universe. Therefore, measuring the number density of clusters at high redshift is a powerful probe of the total density, Ω. Since the S-Z brightness is independent of

redshift, millimeter wave searches for high-redshift clusters are potentially more productive than X-ray searches.

Again, the large beam of BOOMERANG is non-optimal for detection of clusters, but a large region of sky was mapped (1800 square degrees) to a 1σ depth of roughly 100 mJy at 150 GHz. At this flux limit, between 10 ($\Omega = 1.0$) and 200 ($\Omega = 0.2$) clusters should be detectable at 4σ [2]. In this large region of sky (1800 square degrees gives 45,000 $12'$ pixels), there would be only 3 pixels with a 4σ due to statistical noise alone.

A linear combination of BOOMERANG maps at the three frequencies can be created which maximally removes CMB anisotropy and galactic dust, leaving S-Z signal. This work is still in progress.

9.4 High-redshift Galaxies

The history of galaxy and star formation can be probed by measuring the number density and redshift of high-redshift galaxies. Millimeter-wave and submillimeter searches for these objects are expected to be highly productive [5]. The large beam size of BOOMERANG is not well suited to these sub arcminute-sized objects which will be heavily diluted. At a 5σ detection threshold to avoid false detections due to statistics, no galaxies will be seen[5].

Chapter 10 Discussion

A precision measurement of the angular power spectrum of the CMB was made with the BOOMERANG experiment, revealing to high accuracy the position of an acoustic peak in the angular power spectrum at $\ell_{peak} = 197 \pm 6$. Within the context of cold dark matter models of structure formation, this result implies a nearly flat universe.

When taken with other cosmological results which indicate that the expansion of the universe is accelerating, this result implies that the cosmological constant Λ is non-zero and that dark energy makes up a considerable fraction of the energy density of the universe.

Further analysis of the angular power spectrum measured by BOOMERANG shows a suppressed second acoustic peak which points to a baryon content that is 2.5σ higher than results from big-bang nucleosynthesis and the latest observations of the primordial deuterium ratio [71]. Combining the data with weak priors based on measurements of large scale structure, Hubble's constant, and the age of the Universe gives a significant detection of the dark energy $\Omega_\Lambda = 0.66\ ^{+0.07}_{-0.09}$ and of cold dark matter $\Omega_C h^2 = 0.14^{+0.003}_{-0.002}$.

It is important to note that the cosmological analysis was done with great theoretical prejudice, staying entirely in the context of adiabatically seeded CDM models. The parameters estimated by the BOOMERANG measurement are only accurate under that assumption. This is not entirely unmotivated; the presence of an acoustic peak localized in ℓ-space is strong evidence that this paradigm is correct.

The results reported in this thesis are based on a small fraction of the data. When more channels and a larger variety of the sky are analyzed, cosmic variance and instrument noise in the maps may be reduced further.

The analysis of BOOMERANG data can be further refined to measure C_ℓ at higher ℓ. As seen in Chapter 8, extending the measured power spectrum to these small angular scales has the possibility of breaking some of the degeneracies in the parameter estimation. An improvement in the accuracy of the determination of the telescope pointing is key to making accurate measurements at higher ℓ. Currently, a better calibration of the Sun sensor is in progress, which has great promise for improving the current pointing jitter of $4.5'$ rms.

Figure 10.1 shows a comparison of the BOOMERANG angular power spectrum with pre-

vious measurements. While a peak in the power spectrum was evident from these previous measurement, the BOOMERANG spectrum provides the ℓ-space resolution and precision to measure the position of the peak to much higher accuracy than all but the TOCO experiment, which constrains the position of the peak with comparable precision. The release of data from the balloon-borne MAXIMA agrees well with the BOOMERANG measurement [28] as shown in Figure 10.2.

The BOOMERANG spectrum tends to be slightly lower overall than some of the more recent experiments such as TOCO. Additionally, agreement with MAXIMA is improved by shifting the BOOMERANG power spectrum towards the upper end of the 10% calibration error (Figure 10.3).

Several factors could explain this discrepancy. Pointing jitter or an incorrectly measured beam could smear out the power on all angular scales. We are confident that the beam is well enough understood that this is not a problem in the case of BOOMERANG. Additionally, an overestimate of the responsivity of BOOMERANG could account for the discrepancy. The calibration of BOOMERANG channel 150A on the galactic sources in fact shows a slightly lower responsivity than the responsivity to the dipole.

Further precision results are expected shortly from many other experiments. MAXIMA has data from a second flight in 1999 which is currently being analyzed. The ground-based CBI and DASI interferometers have taken months of data as of October 2000. The Top Hat long duration balloon-borne experiment is expected to fly in December 2000, and the MAP satellite will launch in mid-2001 and make a full-sky map at $12'$ resolution. A second space mission, Planck, will make a highly precise measurement of temperature anisotropy and is planned for a 2007 launch.

The BOOMERANG receiver could be refitted in several simple ways which would provide further insight into the CMB. The receiver can be turned into a polarimeter and search for polarization in the CMB. An orthomode transducer, a wire-grid polarizer, or a polarization-sensitive bolometer can be used to select and modulate the polarization. Alternatively, the receiver could be fitted with single-mode feeds at 240 GHz with $6'$ resolution, allowing a measurement of the angular power spectrum to be made to much higher angular resolution. Better pointing sensors are certainly necessary for more precise attitude reconstruction.

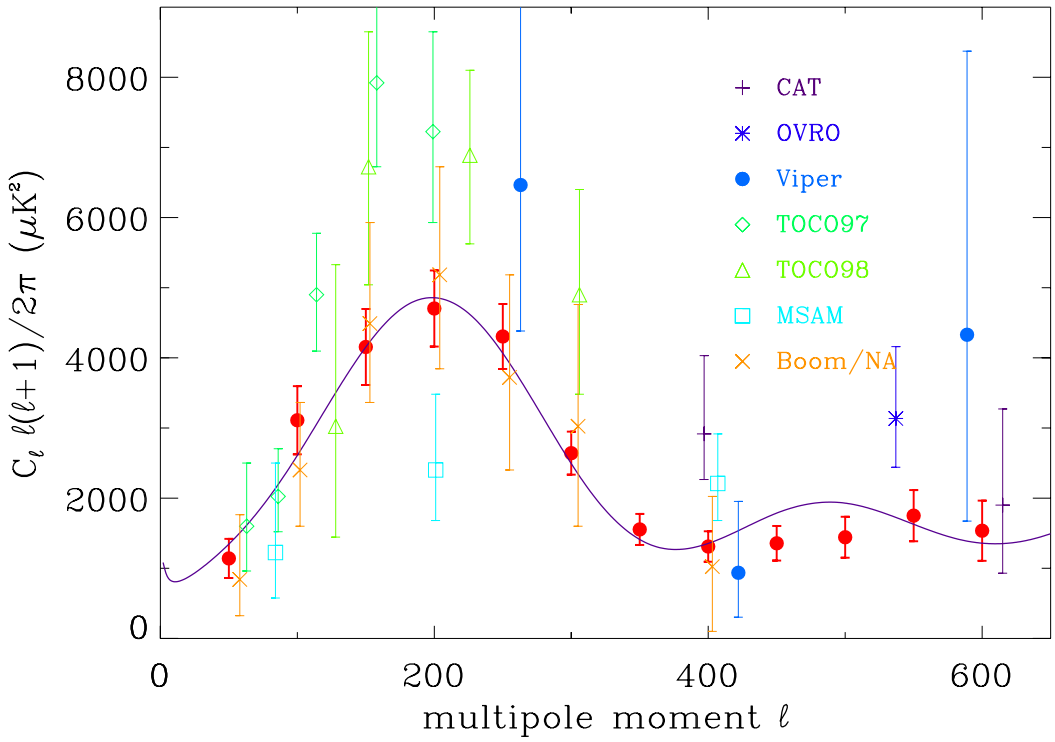

Figure 10.1:
The angular power spectrum of the CMB as measured by Boomerang (points in red) compared with other measurements in the field released prior to April 2000: TOCO [48] [70], Python [16], MSAM [73], CAT [64], OVRO [35], and Boomerang/NA [44]. The solid line is the best fit model from Boomerang/NA, which does not fit the Boomerang data at $\ell \sim 500$

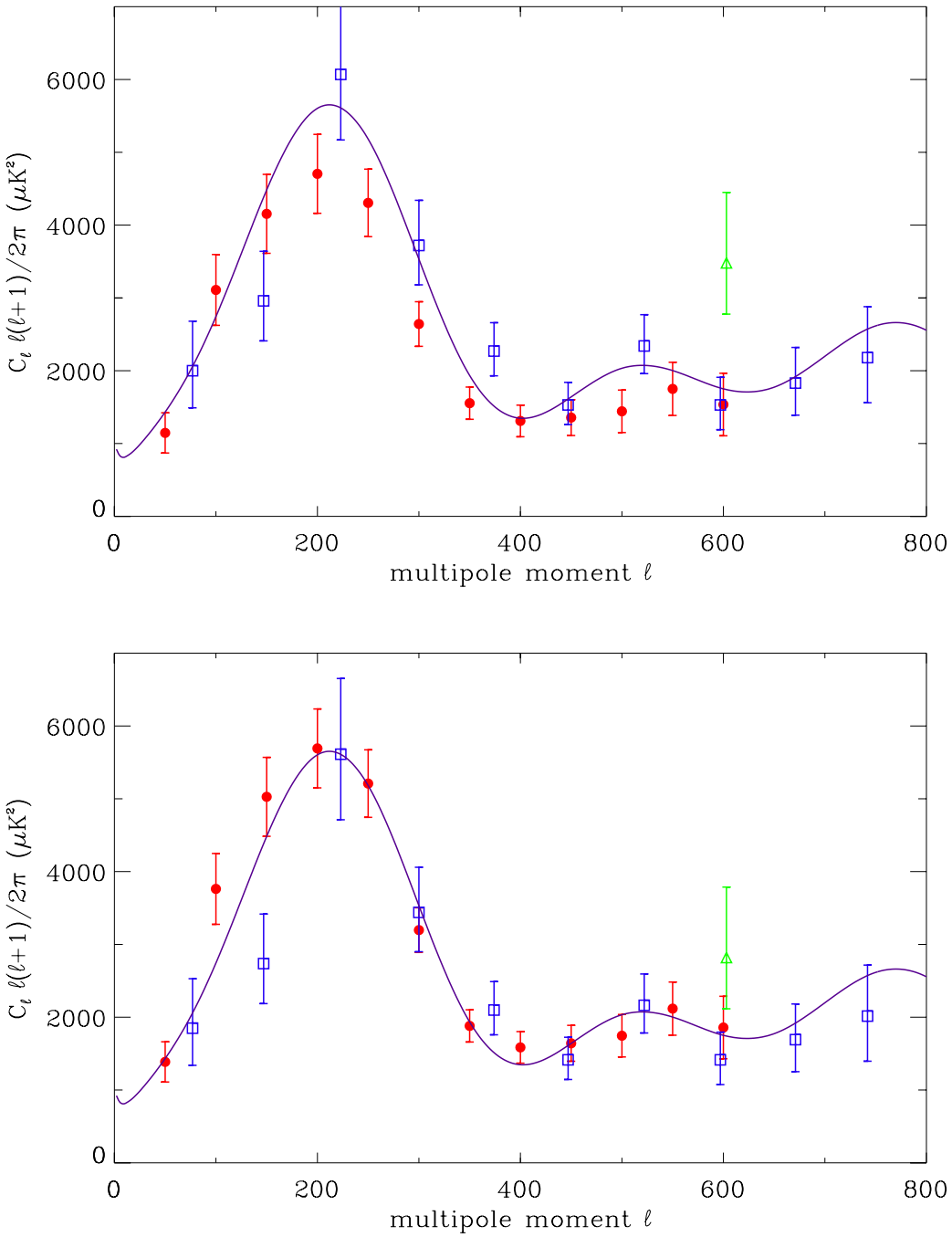

Figure 10.2:
A comparison of the BOOMERANG power spectrum (red circles) with the MAXIMA power spectrum (blue squares) and the CBI preliminary power spectrum [60] (green triangle). The solid curve is the $\Omega = 1$ model from [30]. The top panel shows the uncorrected data as published by both experiments. The bottom panel shows the results from the MAXIMA and BOOMERANG shifted to the limits of their calibration uncertainty. The MAXIMA data are reduced in amplitude by 4% and the BOOMERANG data are increased by 10%. The CBI data point is reduced by 10%, as it is expected to decrease with the inclusion of more observations [60]. Agreement between the three experiments is greatly improved.

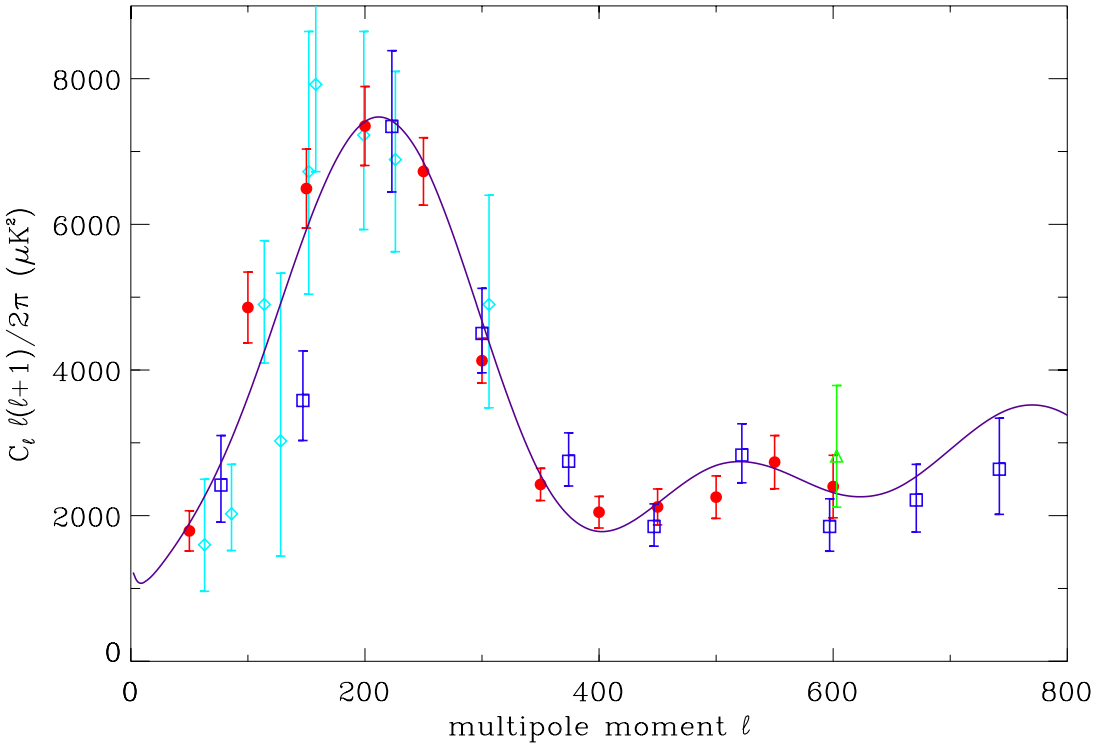

Figure 10.3:
A comparison of the BOOMERANG power spectrum scaled up by 25% (red circles) with the MAXIMA power spectrum scaled up by 10% (blue squares), the CBI preliminary power spectrum scaled down by 10% (green triangle), and the TOCO spectrum (light blue diamonds). The solid curve is the $\Omega = 1$ model from [30], scaled up by 15%. When scaled as indicated, these four experiments agree quite well.

Appendix A Bolometer Data Summary

A.1 Time Constant

Channel	lab	flight	JPL designation
90A	19.9(24.5)	22.48	5.6/1
90B	18.7(31.8)	21.92	5.6/04
150A	11.4	10.8	3.4/13
150B	12.2	13.3	3.4/14
150A1	10.3	13.3	3.4/03
150A2	10.3	12.0	3.4/1
150B1	12.7	16.3	3.4/0
150B2	16.75	21.2	4.8/03
240A1	6.77	8.898	M1/20
240A2	8.84	7.24	M1/28
240B1	9.36	10.567	M1/14
240B2	7.07	8.77	M1/10
400A1	< 6	4.184	M2/05
400A2	10.6	9.92	M2/02
400B1	< 6	4.464	M2/28
400B2	< 6	4.298	M2/27
DarkA	3.037		M2/12
DarkB	24.422		3.4/08

Table A.1:
All time constant values are in milliseconds. The lab time constants were measured optically with a chopper (see Section 4.12), flight time constants were measured from response to cosmic rays (see Section 6.8).

A.2 Bolometer Impedence

Channel	V_{bias} mVAC	flight V_{bolo} mVDC	flight R_{bolo} MΩ	ground V_{bolo} mVDC	ground R_{bolo} MΩ
90A	25	5.68	5.88	4.54	4.44
90B	25	5.16	5.21	4.00	3.81
150A	25	5.40	5.51	3.61	3.38
150B	22	5.27	6.30	3.13	3.31
150A1	30	6.72	5.77	5.49	4.48
150A2	27	5.61	5.25	4.64	4.15
150B1	25	5.46	5.59	3.98	3.79
150B2	20	4.47	5.46	2.90	3.39
240A1	37	7.94	5.46	5.71	3.65
240A2	40	8.20	5.15	5.67	3.30
240B1	35	9.17	7.10	5.91	4.06
240B2	40	8.35	5.27	5.97	3.51
400A1	60	11.1	4.54	8.96	3.51
400A2	52	12.7	6.50	11.68	5.79
400B1	55	12.8	6.04	8.79	3.80
400B2	60	11.2	4.57	11.01	4.49

Table A.2:
V_{bolo} is the voltage at the bolometer. The flight impedence and voltage are average values at float. The ground impedence and voltage are looking through the neutral density filters at a 77K load.

A.3 In-flight load curve

Channel	V_{bias} mV	V_{bolo} mV	V_{bias} mV	V_{bolo} mV	V_{bias} mV	V_{bolo} mV	V_{bias} mV	V_{bolo} mV
90A	10	2.87	25	5.78	40	5.81		
90B	10	2.57	25	5.27	40	5.51		
150A	10	3.19	25	5.53	40	5.46		
150B	8.8	2.74	22	5.35	35.2	5.35		
150A1	12	3.19	30	6.84	48	6.91		
150A2	10.8	2.80	27	5.73	43.2	5.83		
150B1	10	2.52	25	5.62	40	6.02		
150B2	8	1.94	20	4.53	32	5.15		
240A1	14.8	3.89	37	8.08	59.2	8.46		
240A2	16	4.69	40	8.34	64	8.23		
240B1	14	3.74	35	8.43	56	9.15		
240B2	16	4.55	40	9.33	64	9.41		
400A1					60	11.15	82.1	11.86
400A2					52	12.92	71.1	14.21
400B1					55	11.20	75.3	12.32
400B2					60	12.95	82.1	13.46
DarkA	8	1.09	20	2.68	32	5.00		
DarkB	12	2.29	30	5.03	48	4.27		

Table A.3:
Values of AC bias voltage (V_{bias}) and voltage at the bolometer (V_{bolo}) for the in-flight load curve, taken on the eigth day of the Antarctic flight. These load curves are plotted over load curves taken pre-flight in Figures 4.5, 4.6, 4.7, and 4.8.

A.4 Lab Load Curves

Channel	Peak S 10^8 V/W	R(peak S) MΩ	T (peak S) K	G (peak S) pW/K
90A	3.4	4.0	0.387	80
90B	3.0	3.6	0.397	84
150A	2.7	2.2	0.438	72
150B	2.6	2.7	0.422	85
150A1	2.9	3.5	0.398	88
150A2	3.3	5.8	0.370	110
150B1	3.1	3.1	0.409	78
150B2	2.5	2.1	0.445	73
240A1	1.9	3.9	0.389	183
240A2	1.9	3.4	0.402	192
240B1	1.9	3.3	0.404	208
240B2	1.9	3.4	0.401	215
400A1	1.1	4.1	0.385	600
400A2	1.9	5.4	0.65	448
400B1	1.2	2.8	0.420	470
400B2	1.5	4.4	0.381	500
Dark A	2.2	6.8	0.348	430
Dark B	4.5	3.1	0.407	40

Table A.4:
Bolometer parameters derived from load curves measured on the ground. The values of R, G, and T are at the peak responsivity S. $R(T)$ was assumed to follow the law $R = R_0 e^{\sqrt{\frac{\Delta}{T}}}$ with R_0 =300Ω and Δ =35 K for all bolometers.

A.5 Flight Noise

Channel	flight noise $nV/\sqrt{Hz}$	ground S 10^8 V/W	flight S 10^8 V/W	NEP 10^{-17} W/$\sqrt{Hz}$
90A	14	3.4	4.3	3.2
90B	13	3.0	3.9	3.3
150A	14	2.7	4.1	3.4
150B	16	2.5	4.3	3.7
150A1	16	2.9	3.6	4.4
150A2	15	3.3	4.1	3.7
150B1	15	3.1	4.4	3.4
150B2	13	2.5	3.9	3.3
240A1	15	1.9	2.7	5.6
240A2	16	1.9	2.8	5.7
240B1	16	1.9	2.7	5.9
240B2	75	1.9	3.0	25.0
400A1	55	1.1	1.4	39.2
400A2	17	1.4	1.5	11.3
400B1	20	1.2	1.5	13.3
400B2	21	1.5	1.8	11.7
DarkA	28	2.2	2.2	12.7
DarkB	25	4.5	4.5	5.6

Table A.5:
The quoted flight noise is the average noise power at 1Hz. Flight responsivity (S) is estimated by scaling the ground responsivity to flight by the ratio of the bolometer voltages. See Section 6.9 for further information.

A.6 Flight Optical Background

Channel	G pW/K	ΔT mK	Q pW	T_Q K
90A	81	23	1.9	4.3
90B	82	35	2.9	6.9
150A	81	11	0.9	2.6
150B	88	15	1.3	3.8
150A1	88	31	2.7	10.7
150A2	104	33	3.5	11.2
150B1	90	39	3.5	13.7
150B2	73	44	3.2	11.5
240A1	181	33	6.1	10.6
240A2	180	20	3.4	4.3
240B1	195	33	6.5	12.5
240B2	202	24	4.9	7.2
400A1	519	29	14.9	12.6
400A2	412	13	5.5	7.4
400B1	422	31	13.0	12.3
400B2	424	8	3.6	5.0
Dark A	377	119	45.0	
Dark B	28	6	1.6	

Table A.6:
Another estimate of thermal conductivity G based on the slope of $T(P)$, and an estimate of the flight loading (Q) by extrapolating the in-flight load curve to zero electrical power to obtain ΔT. The resulting value of Q is very sensitive to $R(T)$, which is not well known. Using optical efficiency numbers from below, the corresponding RJ temperature was found for each channel (T_Q). Fitting a RJ spectrum to the loading in all optical channels gives a background of 9.5K. See Section 6.11 for details.

A.7 In-Flight Responsivity

Channel	lab scaled to flight $\mu V/K_{CMB}$	dipole $\mu V/K_{CMB}$	sensivity $\mu K\sqrt{s}$
90A	54	68	145
90B	49	67	137
150A	74	76	130
150B	75	78	145
150A1	44	49	231
150A2	50	67	158
150B1	50	54	196
150B2	57	50	184
240A1	43	48	221
240A2	47	68	166
240B1	39	45	250
240B2	51	67	792
400A1	7.6		
400A2	3.9		
400B1	7.0		
400B2	4.9		

Table A.7:
Lab responsivity is scaled to flight by the ratio of the bolometer DC voltages. Sensitivity is obtained by dividing the voltage noise in Table A.5 by the dipole responsivity.

A.8 Optical Efficiency

Channel	$\int \frac{dB_\nu(2.7K,\nu)}{dT} d\nu$ 10^{-12} W/K/cm^2/sr	S (loadcurve) 10^8 V/W	$\frac{dV}{dT}$(dipole) 10^{-5} V/K	$A\Omega_{effective}$ cm^2 sr	$A\Omega$ cm^2 sr	η
90A	5.58	4.3	6.8	0.028	0.09	0.31
90B	6.30	3.9	6.7	0.027	0.09	0.30
150A	29.9	4.1	7.6	0.0061	0.04	0.15
150B	28.9	4.3	7.8	0.0062	0.04	0.16
150A1	30.5	3.6	4.9	0.0045	0.05	0.09
150A2	29.9	4.1	6.7	0.0055	0.05	0.11
150B1	27.4	4.4	5.4	0.0045	0.05	0.09
150B2	25.8	3.9	5.0	0.0050	0.05	0.10
240A1	56.1	2.7	4.8	0.0032	0.05	0.06
240A2	55.1	2.8	6.8	0.0044	0.05	0.09
240B1	57.2	2.7	4.5	0.0029	0.05	0.06
240B2	58.1	3.0	6.7	0.0038	0.05	0.08
400A1	13.5	1.4	0.76	0.0040	0.05	0.08
400A2	10.5	1.5	0.39	0.0025	0.05	0.05
400B1	12.7	1.5	0.7	0.0036	0.05	0.07
400B2	11.4	1.8	0.49	0.0024	0.05	0.05

Table A.8:
Responsivity to CMB fluctuations is $\frac{dV}{dT} = \frac{dV}{dP} A\Omega\eta \int \frac{dB_\nu(2.7K,\nu)}{dT} d\nu$. By comparing the responsivity to the dipole ($\frac{dV}{dT}$) to the throughput ($A\Omega$) and voltage responsivity (S), the optical efficiency η can be determined. The throughput quoted is the design throughput of the feed or photometer.

Appendix B Calculation of Beam Offset Parameters

The azimuth and elevation of the gondola boresight is reconstructed from the Sun sensor and gyros. To reference this boresight to the position of the millimeter-wave beams on the sky, the offsets of each of the beams from the boresight are parameterized. The parameters we choose: α and β are respectively the elevation and azimuth offsets when the gondola boresight is pointed at the horizon. The parameters for each beam are measured through observations of galactic sources. First, the attitude of the gondola boresight is reconstructed using the pointing sensors and a boresight right ascension and declination is computed for each sample. To compute the beam parameters, a sample is found when a beam is centered on a source. Then the known source position is compared with the position of the gondola boresight. See Section 6.3 and Figure 6.3 for the results of this analysis from the Antarctic flight of BOOMERANG.

Once these offset parameters are known, it is a straightforward linear algebra calculation which determines how the beam azimuth and elevation vary with boresight azimuth and elevation.

B.1 Rotation of the Gondola Boresight

First, we begin with computing the matrix which describes the orientation of the gondola boresight vector. Assume that the gondola boresight is oriented along the x-axis. To change the azimuth by angle φ, rotate about the z axis. The matrix to perform this rotation is:

$$M_{az} = \begin{pmatrix} \cos\varphi & \sin\varphi & 0 \\ -\sin\varphi & \cos\varphi & 0 \\ 0 & 0 & 1 \end{pmatrix}$$

To change the elevation by angle θ, rotate about the axis which is perpendicular to both the z-axis and the new azimuth direction (that is, rotate about the new y-axis). The matrix

describing this operation is:

$$M_{el} = \begin{pmatrix} \cos\theta & 0 & -\sin\theta \\ 0 & 1 & 0 \\ \sin\theta & 0 & \cos\theta \end{pmatrix}$$

To rotate in roll by angle ψ, rotate about the new x-axis:

$$M_{roll} = \begin{pmatrix} 1 & 0 & 0 \\ 0 & \cos\psi & \sin\psi \\ 0 & -\sin\psi & \cos\psi \end{pmatrix}$$

The order of these rotations must be kept, since the matrices are non-commutative, and the total rotation is given by:

$$\begin{aligned} M_{tot} &= M_{az} M_{roll} M_{el} \\ &= \begin{pmatrix} \cos\varphi\cos\theta - \sin\varphi\sin\psi\sin\theta & \sin\varphi\cos\psi & \cos\varphi\sin\theta + \sin\varphi\sin\psi\cos\theta \\ -\sin\varphi\cos\theta - \cos\varphi\sin\psi\sin\theta & \cos\varphi\cos\psi & -\sin\varphi\sin\theta + \cos\varphi\sin\psi\cos\theta \\ -\cos\psi\sin\theta & -\sin\psi & \cos\psi\cos\theta \end{pmatrix} \end{aligned}$$

B.2 Calculation of Beam Position

To describe the measured position of a beam, start with the gondola boresight oriented along the x-axis, and the beam offset by α in elevation and by β in azimuth. In this position, the beam orientation can be described with the following vector:

$$\overrightarrow{r}_{beam} = \begin{pmatrix} \cos\beta\cos\alpha \\ \sin\beta\cos\alpha \\ \sin\alpha \end{pmatrix}$$

The beam vector is then rotated with the above matrix describing the gondola orientation:

$$\overrightarrow{r'}_{beam} = M_{tot}\overrightarrow{r}_{beam} = \begin{pmatrix} r'_x \\ r'_y \\ r'_z \end{pmatrix}$$

where the components of $\overrightarrow{r'}_{beam}$ are:

$$\begin{aligned}
r'_x &= \cos\beta\cos\alpha\cos\varphi\cos\theta - \cos\beta\cos\alpha\sin\varphi\sin\psi\sin\theta \\
&\quad + \sin\varphi\cos\psi\sin\beta\cos\alpha + \sin\alpha\cos\varphi\sin\theta + \sin\alpha\sin\varphi\sin\psi\cos\theta \\
r'_y &= -\cos\beta\cos\alpha\sin\varphi\cos\theta - \cos\beta\cos\alpha\cos\varphi\sin\psi\sin\theta \\
&\quad + \cos\varphi\cos\psi\sin\beta\cos\alpha - \sin\alpha\sin\varphi\sin\theta + \sin\alpha\cos\varphi\sin\psi\cos\theta \\
r'_z &= -\cos\psi\sin\theta\cos\beta\cos\alpha - \sin\psi\sin\beta\cos\alpha \\
&\quad + \cos\psi\cos\theta\sin\alpha
\end{aligned}$$

The beam azimuth and elevation can be read off:

$$\begin{aligned}
\theta' &= \sin^{-1}\left(r'_z\right) \\
\varphi' &= \tan^{-1}\left(\frac{r'_y}{r'_x}\right)
\end{aligned}$$

B.3 Calculation of Beam Offset Parameters

To calculate α and β given a boresight position and a source position, the inverse problem is solved:

$$\overrightarrow{r}_{beam} = M^{-1}_{beam}\overrightarrow{r'}_{beam} = \begin{pmatrix} r_x \\ r_y \\ r_z \end{pmatrix}$$

where the components of $\overrightarrow{r}_{beam}$ are:

$$\begin{aligned}
r_x &= \cos\varphi'\cos\theta'\cos\varphi\cos\theta - \cos\varphi'\cos\theta'\sin\varphi\sin\psi\sin\theta \\
&\quad + \sin\varphi'\cos\theta'\sin\varphi\cos\theta + \sin\varphi'\cos\theta'\cos\varphi\sin\psi\sin\theta + \cos\psi\sin\theta\sin\theta' \\
r_y &= \sin\varphi\cos\psi\cos\varphi'\cos\theta' - \cos\varphi\cos\psi\sin\varphi'\cos\theta' \\
&\quad + \sin\psi\sin\theta' \\
r_z &= \cos\varphi'\cos\theta'\cos\varphi\sin\theta + \cos\varphi'\cos\theta'\sin\varphi\sin\psi\cos\theta \\
&\quad + \sin\varphi'\cos\theta'\sin\varphi\sin\theta - \sin\varphi'\cos\theta'\cos\varphi\sin\psi\cos\theta - \cos\psi\cos\theta\sin\theta'
\end{aligned}$$

and the beam offset parameters can be read off:

$$\begin{aligned} \alpha &= \sin^{-1}(r_z) \\ \beta &= \tan^{-1}\left(\frac{r_y}{r_x}\right) \end{aligned}$$

Appendix C Roll Correction to Azimuth and Elevation

A roll in the gondola also affects the azimuth and elevation of the telescope beam. To correct the data from two-axis Sun sensor for this effect, the roll measured by the gyroscope must be used.

A vector can be constructed containing the Sun azimuth α and elevation ϵ. This is then rolled into the frame of the Sun sensor with the roll matrix from Appendix B:

$$\begin{aligned} v_{sun} &= \begin{pmatrix} 1 & 0 & 0 \\ 0 & \cos\psi & \sin\psi \\ 0 & -\sin\psi & \cos\psi \end{pmatrix} \begin{pmatrix} \cos\epsilon\cos\alpha \\ \cos\epsilon\sin\alpha \\ \sin\epsilon \end{pmatrix} \\ &= \begin{pmatrix} \cos\epsilon\cos\alpha \\ \cos\psi\cos\epsilon\sin\alpha + \sin\psi\sin\epsilon \\ -\sin\psi\cos\epsilon\sin\alpha + \cos\psi\sin\epsilon \end{pmatrix} \end{aligned}$$

The true azimuth and elevation can be read off from the above equation:

$$\begin{aligned} \alpha' &= \tan^{-1}\left(\frac{\cos\psi\cos\epsilon\sin\alpha + \sin\psi\sin\epsilon}{\cos\epsilon\cos\alpha}\right) \\ \epsilon' &= \sin^{-1}\left(-\sin\psi\cos\epsilon\sin\alpha + \cos\psi\sin\epsilon\right) \end{aligned}$$

Bibliography

[1] Arnold, E. M., et al., *Astronomy and Astrophysics*, **70**, L1 (1978).

[2] Barbosa, D., J. G. Bartlett, A. Blanchard, *Astrophysics and Space Science*, **261**, 277 (1998).

[3] Bennett, C. L. et al., *Astrophysical Journal*, **464**, L1 (1996).

[4] de Bernardis P. et al., *Nature*, **404**, 955, (2000).

[5] Blain, A.W. et al., *Astrophysical Journal*, **512**, 2 (1999).

[6] Bock, J. J., PhD thesis, University of California at Berkeley (1994).

[7] Bond, J. R., G. Efstathiou, and M. Tegmark, *Monthly Notices of the Royal Astronomical Society*, **291**, L33 (1997).

[8] Bond, J.R. and A. H. Jaffe, *Phil. Trans. R. Soc. London*, **357**, 57 (1999).

[9] Bond, J. R., A. H. Jaffe, and L. Knox, *Astrophysical Journal*, **533**, 19 (2000).

[10] Borrill, J., *Proc. 5th European SGI/Cray MPP Workshop* (1999) *astro-ph/9911389*.

[11] Boscaleri, A. et al., *SPIE Proceedings*, **1304**, 127 (1990).

[12] Boscaleri, A. et al., *SPIE Procceedings*, **1341**, 58 (1990).

[13] Boscaleri, A. et al., *Measurement Science and Technology* **5**, 190 (1994).

[14] Cheung, L. H., et al., *Astrophysical Journal*, **240**, 74 (1980).

[15] Church, S. E. et al., *Proc. 30th ESLAB Symp. Submillimetre and Far-Infrared Space Instrumentation*, ESTEC, Noordwijk, Netherlands, ESA SP-388 (1996).

[16] Coble, K., et al., *Astrophysical Journal*, **519**, L5 (1999).

[17] Coble, K., et al., *Astrophysical Journal*, in preparation (2000).

[18] Contaldi, C., M. Hindmarsh, and J. Magueijo, *Phys. Rev. Lett.*, **82**, 679 (1999).

[19] Cox, P., et al., *Astronomy and Astrophysics*, **297**, 168 (1995).

[20] Dodelson, S. and L. Knox, *Phys. Rev. Lett.*, **84**, 3523 (2000).

[21] Finkbeiner, D. P., M. Davis, and D. J. Schlegel, *Astrophysical Journal*, **524**, 2 (1999).

[22] Fischer M. L., et al., *Astrophysical Journal* **388**, 242 (1992).

[23] Freedman, W. L., (1999) *astro-ph/9909076*.

[24] Glenn, J., et al., *Applied Optics*, in preparation (2000).

[25] Gorski, K. M., E. Hivon, and B. D. Wandelt, *Proc. MAP/ESO Conference*, Garching August 2-7 (1998).

[26] Grannan, S. M. et al., *Int J Infrared Milli.* **18**, 319 (1997).

[27] Gunn, J. E. and B. A. Peterson, *Astrophysical Journal*, **142**, 1633 (1965).

[28] Hanany, S. et al., *Astrophysical Journal*, in press (2000) *astro-ph/0005123*.

[29] Hu, W., N. Sugiyama, and J. Silk, *Nature*, **386**, 37, (1997).

[30] Jaffe, A. H., et al., *Phys Rev Lett* , submitted (2000) *astro-ph/0007333*.

[31] Kogut, A. et al., *Astrophysical Journal*, **470**, 653 (1996).

[32] Kogut, A., in *Anomalous Microwave Emission in Microwave Foregrounds*, Eds. A. de Oliveira-Costa and M. Tegmark, Astron. Soc. Pacific conf series 181, 91 (1999).

[33] Lange, A. E., et al., *Astrophysical Journal*, **428**, 384 (1994).

[34] Lee, C., et al., *Proc. 30th ESLAB Symp. Submillimetre and Far-Infrared Space Instrumentation*, ESTEC, Noordwijk, Netherlands, ESA SP-388 (1996).

[35] Leitch, E. M., et al., *Astrophysical Journal*, **532**, 37 (2000).

[36] Lewis, A., A. Callinor, and A. Lasenby, *astro-ph/9911177* (1999).

[37] Masi, S. et al., *Cryogenics* **38**, 319 (1998).

[38] Masi, S. et al., *Cryogenics* **39**, 217 (1999).

[39] Masi, S. et al., *Astrophysical Journal*, in preparation (2000).

[40] Mather, J., *Applied Optics* **23**, 584 (1984).

[41] Mather, J.C. et al., *Astrophysical Journal*, **420**, 439 (1994).

[42] Mauskopf, P. D., PhD thesis, University of California, Berkeley (1996).

[43] Mauskopf, P. D., et al., *Applied Optics*, **36**, 765 (1997).

[44] Mauskopf, P. D., et al., *Astrophysical Journal*, **536**, L59 (2000).

[45] Mauskopf, P. D., *Astrophysical Journal*, submitted (2000).

[46] McCullough, P. R., et al., in *Anomalous Microwave Emission in Microwave Foregrounds*, Eds. A. de Oliveira-Costa and M. Tegmark, Astron. Soc. Pacific conf series 181, 91 (1999).

[47] Melchiorri, A., et al., *Astrophysical Journal*, **536**, L63 (2000).

[48] Miller A.D. et al., *Astrophysical Journal*, **524**, L1 (1999).

[49] Mould, J.R. et al., *Astrophysical Journal*, **529**, 786 (2000).

[50] Netterfield, C. B., et al., *Astrophysical Journal*, **474**, 47 (1997).

[51] Olive, K.A., G. Steigman, and T. P. Walker, *Phys. Rep.*, **333**, 389 (2000).

[52] de Oliveira-Costa, A. et al., *Astrophysical Journal*, **509**, L77 (1998).

[53] Peebles, P.J.E., *Principles of Physical Cosmology*, Princeton UP (1993).

[54] Pen, U., U. Seljak, and N. Turok, *Phys. Rev. Lett.* **79**, 1611 (1997).

[55] Penzias, A. A. and R. W. Wilson, *Astrophysical Journal*, **142**, 419 (1965).

[56] Perlmutter, S. et al., 1999, *Astrophysical Journal*, **517** , 565 (1999).

[57] Piacentini, F. et al., *Astrophysical Journal*, submitted (2000).

[58] Prunet, S. et al., *Proc.of the conference "Energy Density in the Universe,"* D. Langlois, R. Ansari, J. Bartlett, editors, Editiones Frontieres (2000).

[59] Puchalla, J.L. et al., *Astrophysical Journal*, sumitted, (2000) *astro-ph/0005420.*

[60] Readhead, A., private communication (2000).

[61] Sachs, R. K. and A. M. Wolfe, *Astrophysical Journal* **147**, 73 (1967).

[62] Seljack, U. and M. Zaldarriaga, *Astrophysical Journal*, **469**, 437 (1996).

[63] Schlegel, D.J., D.P. Finkbeiner, and M. Davis, *Astrophysical Journal*, **500**, 2 (1998).

[64] Scott, P. F. et al., *Astrophysical Journal*, **461**, L1 (1996).

[65] Smooth, G. in *Anomalous Microwave Emission in Microwave Foregrounds*, Eds. A. de Oliveira-Costa and M. Tegmark, Astron. Soc. Pacific conf series 181, 91 (1999).

[66] Sunyaev, R. A. and Ya. B. Zel'dovich, *Comments on Astrophysics and Space Physics*, **4**, 173 (1972).

[67] Shelton, K., senior thesis, California Institute of Technology (2000).

[68] Tegmark, M., *Astrophysical Journal*, **480**, 87 (1997).

[69] Toffolatti, L., et al., *Monthly Notices of the Royal Astronomical Society*, **297**, 117 (1998).

[70] Torbet, E., et al., *Astrophysical Journal*, **521**, L79 (1999).

[71] Tytler, D., J.M. O'Meara, N. Suzuki, and D. Lubin, *Physics Reports*, **333**, 409 (2000).

[72] Ulrich, R., *Infrared Physics*, **7**, 37 (1967).

[73] Wilson, G.W., et al., *Astrophysical Journal*, **532**, 57 (2000).

[74] Yamada, Y., A. Mitsuishi, and H. Yoshinaga, *J. Opt. Soc. Am.*, **52**, 17 (1962).